Belle note №1351, v1.3, 30.03.2016

Study of Michel parameters in leptonic τ decays at Belle

H. Aihara, D. Epifanov, N. Shimizu

Abstract

We present a study of Michel parameters in leptonic τ decays using experimental information collected at Belle. Michel parameters are extracted in the unbinned maximum likelihood fit of the ($\tau^{\mp} \to \ell^{\mp}\nu\nu$, $\tau^{\pm} \to \pi^{\pm}\pi^0\nu$) events in the full 9D phase space. Essential point of the study is analysis of the spin-spin correlation of taus, which allows us to extract $\xi_\rho\xi$ and $\xi_\rho\xi\delta$ parameters in addition to ρ and η.

2014

Contents

1 Introduction

There are three generations of the fundamental leptons in the Standard Model (SM) of the elementary particles and their interactions: (ν_e, e^-), (ν_μ, μ^-), (ν_τ, τ^-). The properties of the charged leptons appear not only as external parameters in the theory but also reflect the basic structure of the SM. Therefore, investigation of the charged leptons provides the crucial test of the SM.

The Belle detector at the KEKB energy-asymmetric e^+e^- collider has collected the world largest integrated luminosity of 1053 fb^{-1} in the region of the $\Upsilon(1S) - \Upsilon(5S)$ resonances. It provides a huge sample of more than 900 million $\tau\tau$ events, which opened a new era in precise studies of τ decays.

Because of its relatively large mass and the simplicity of its decay mechanism, τ lepton offers many interesting, and sometimes unique, possibilities for testing and improving the SM. These studies involve the leptonic and hadronic sectors and cover a large range of topics, from the measurement of the leptonic couplings in the weak charged current and the search for lepton flavor violation, providing precise universality tests, to a complete investigation of hadronic production from the Quantum Chromodynamics vacuum.

In the SM the charged weak interaction is described by the exchange of $W^\pm$ boson with a pure vector coupling to only left-handed fermions. Thus, in the low-energy four-fermion framework, the Lorentz structure of the matrix element is predicted to be of the type "V-A⊗V-A". Deviations from this behavior would indicate new physics and might be caused by changes in the W-boson couplings or through interactions mediated by new gauge bosons. Leptonic τ decays ($\tau^- \to \ell^- \bar{\nu}_\ell \nu_\tau$ ($\ell = e, \mu$)) are the only ones in which the electroweak couplings can be probed without disturbance from the strong interaction. This makes them an ideal system to study the Lorentz structure of the charged weak current.

The most general, Lorentz invariant, derivative-free and lepton-number-conserving four-lepton point interaction matrix element for this decay can be written as:

$$\mathcal{M} = \frac{4G}{\sqrt{2}} \sum_{\substack{N=S,V,T \\ i,j=L,R}} g_{ij}^N \Big[\bar{u}_i(l^-)\Gamma^N v_n(\bar{\nu}_l)\Big]\Big[\bar{u}_m(\nu_\tau)\Gamma_N u_j(\tau^-)\Big], \tag{1}$$

$$\Gamma^S = 1,\ \Gamma^V = \gamma^\mu,\ \Gamma^T = \frac{1}{\sqrt{2}}\sigma^{\mu\nu} = \frac{i}{2\sqrt{2}}(\gamma^\mu\gamma^\nu - \gamma^\nu\gamma^\mu) \tag{2}$$

The Γ_N matrices define the properties of the two currents under a Lorentz transformation with $N = S, V, T$ for scalar, vector and tensor interactions, respectively. The indices i and j label the right- or lefthandedness (R, L) of the charged leptons. For a given i, j and N, the handedness of the neutrinos (n, m) are fixed. Ten terms (terms at the g^T_{RR} and g^T_{LL} coupling constants are identically equal to 0) are characterized by ten complex coupling constants g^N_{ij}. In the SM "V-A" interaction the only non-zero coupling constant is $g^V_{LL} = 1$. As the couplings can be complex, with arbitrary total phase, there are 19 independent parameters. The total strength of the weak interaction (charged weak current sector) is determined by the Fermi constant G, hence g^N_{ij} constants are normalized as:

$$3\Big(|g^T_{LR}|^2 + |g^T_{RL}|^2\Big) + \Big(|g^V_{LL}|^2 + |g^V_{LR}|^2 + |g^V_{RL}|^2 + |g^V_{RR}|^2\Big) + \\ + \frac{1}{4}\Big(|g^S_{LL}|^2 + |g^S_{LR}|^2 + |g^S_{RL}|^2 + |g^S_{RR}|^2\Big) \equiv 1 \tag{3}$$

This constrains the coupling constants to be: $|g^S| \leq 2$, $|g^V| \leq 1$ and $|g^T| \leq 1/\sqrt{3}$.

Without measuring the neutrinos and the spin of the outgoing charged lepton, only four Michel parameters (MP) ρ, η, ξ and δ are experimentally accessible. They are bilinear combinations of the coupling constants:

$$\rho = \frac{3}{4} - \frac{3}{4}\Big(|g^V_{LR}|^2 + |g^V_{RL}|^2 + 2|g^T_{LR}|^2 + 2|g^T_{RL}|^2 + \Re\big(g^S_{LR}g^{T*}_{LR} + g^S_{RL}g^{T*}_{RL}\big)\Big) \tag{4}$$

$$\eta = \frac{1}{2}\Re\Big(6g^V_{RL}g^{T*}_{LR} + 6g^V_{LR}g^{T*}_{RL} + g^S_{RR}g^{V*}_{LL} + g^S_{RL}g^{V*}_{LR} + g^S_{LR}g^{V*}_{RL} + g^S_{LL}g^{V*}_{RR}\Big) \tag{5}$$

$$\xi = 4\Re(g^S_{LR}g^{T*}_{LR}) - 4\Re(g^S_{RL}g^{T*}_{RL}) + |g^V_{LL}|^2 + 3|g^V_{LR}|^2 - 3|g^V_{RL}|^2 - |g^V_{RR}|^2 \\ + 5|g^T_{LR}|^2 - 5|g^T_{RL}|^2 + \frac{1}{4}|g^S_{LL}|^2 - \frac{1}{4}|g^S_{LR}|^2 + \frac{1}{4}|g^S_{RL}|^2 - \frac{1}{4}|g^S_{RR}|^2 \tag{6}$$

$$\xi\delta = \frac{3}{16}|g^S_{LL}|^2 - \frac{3}{16}|g^S_{LR}|^2 + \frac{3}{16}|g^S_{RL}|^2 - \frac{3}{16}|g^S_{RR}|^2 - \frac{3}{4}|g^T_{LR}|^2 + \frac{3}{4}|g^T_{RL}|^2 \\ + \frac{3}{4}|g^V_{LL}|^2 - \frac{3}{4}|g^V_{RR}|^2 + \frac{3}{4}\Re\big(g^S_{LR}g^{T*}_{LR}\big) - \frac{3}{4}\Re\big(g^S_{RL}g^{T*}_{RL}\big) \tag{7}$$

and appear in the predicted energy spectrum of the charged lepton.

In the τ rest frame, neglecting radiative corrections, this spectrum is given by:

$$\frac{d\Gamma(\tau^{\mp})}{d\Omega dx} = \frac{4G^2 M_\tau E_{\max}^4}{(2\pi)^4}\sqrt{x^2-x_0^2}\Bigg(x(1-x)+\frac{2}{9}\rho(4x^2-3x-x_0^2)+\eta x_0(1-x)$$

$$\mp\frac{1}{3}P_\tau cos\theta_\ell \xi\sqrt{x^2-x_0^2}\Big[1-x+\frac{2}{3}\delta\big(4x-4+\sqrt{1-x_0^2}\big)\Big]\Bigg),$$

$$x=\frac{E_\ell}{E_{max}},\ E_{max}=\frac{M_\tau}{2}(1+\frac{m_\ell^2}{M_\tau^2}),\ x_0=\frac{m_\ell}{E_{max}}, \tag{8}$$

where P_τ is τ polarization, and θ_ℓ is the angle between τ spin and lepton momentum. In the SM the "V-A" charged weak current is characterized by $\rho = 3/4$, $\eta = 0$, $\xi = 1$ and $\delta = 3/4$. As the differential decay width has to be positive quantity physically allowed values of MP are determined by the following criteria [1]:

$$0 \le \rho \le 1, \tag{9}$$

$$\begin{cases} |\eta| \le 1-\frac{2}{3}\rho, & \rho \le \frac{3}{4} \\ |\eta| \le 2(1-\rho), & \rho > \frac{3}{4} \end{cases} \tag{10}$$

$$|\xi| \le 3-\frac{2}{3}\rho, \tag{11}$$

$$|\xi\delta| \le \rho, \tag{12}$$

$$|7\xi\delta - 3\xi| \le 9(1-|\xi\delta|). \tag{13}$$

These inequalities determine the tetrahedral domain in the ($\rho,\ \xi,\ \xi\delta$) space as shown in Fig.1. It should be noted that the SM values of MP are consistently at the edge of the allowed domain. Any deviation from the pure "V-A" Lorentz structure means effects beyond the SM. Table 1 demonstrates coupling constants and associated MP values for the various structures of the weak vertices in the leptonic τ decay.

Two independent indicators of the new physics, related with the τ right-handed couplings, are linear combinations of MP:

$$\mathcal{S}_R^\tau = \frac{1}{4}(|g_{RR}^S|^2+|g_{LR}^S-2g_{LR}^T|^2)+|g_{RR}^V|^2 = \frac{2}{3}\big[\rho-\xi\delta\big], \tag{14}$$

$$\mathcal{P}_R^\tau = \frac{1}{4}|g_{RR}^S|^2+\frac{1}{4}|g_{LR}^S|+|g_{RR}^V|^2+|g_{LR}^V|^2+3|g_{LR}^T|^2 = \frac{1}{2}\Big[1+\frac{1}{3}\xi-\frac{16}{9}\xi\delta\Big], \tag{15}$$

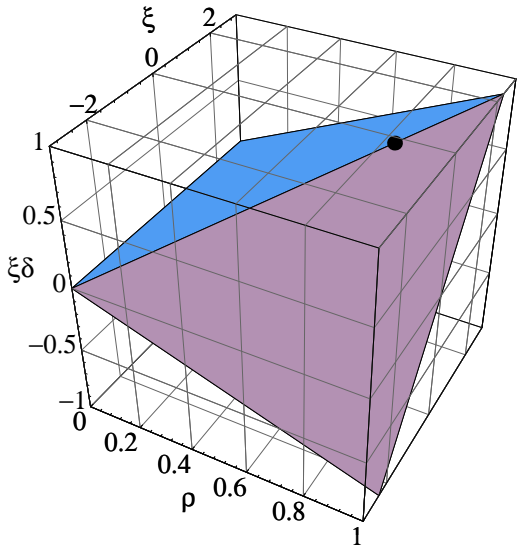

Figure 1: Physically allowed values of MP forming the tetrahedral domain. Standard Model MP values, marked by bold point, lie at the edge of this domain.

Table 1: Coupling constants and corresponding MP values. First column shows the structure of two leptonic currents, the associated nonzero coupling constants are shown in the second column, MP values - in the last four columns.

Type of interaction $\ell\ \nu_\ell$ vertex $\otimes$ $\tau\ \nu_\tau$ vertex	Coupling constants	Michel parameters ρ	ξ	$\xi\delta$	η
V−A $\otimes$ V−A	$g^{\rm V}_{\rm LL}=1$	$\frac{3}{4}$	1	$\frac{3}{4}$	0
V+A $\otimes$ V+A	$g^{\rm V}_{\rm RR}=1$	$\frac{3}{4}$	-1	$-\frac{3}{4}$	0
V $\otimes$ V	$g^{\rm V}_{\rm LL}=g^{\rm V}_{\rm RL}=g^{\rm V}_{\rm LR}=g^{\rm V}_{\rm RR}=\frac{1}{2}$	$\frac{3}{8}$	0	0	0
A $\otimes$ A	$g^{\rm V}_{\rm LL}=-g^{\rm V}_{\rm RL}=-g^{\rm V}_{\rm LR}=g^{\rm V}_{\rm RR}=\frac{1}{2}$	$\frac{3}{8}$	0	0	0
V−A $\otimes$ V+A	$g^{\rm V}_{\rm LR}=1$	0	3	0	0
V+A $\otimes$ V−A	$g^{\rm V}_{\rm RL}=1$	0	-3	0	0
S+P $\otimes$ S−P	$g^{\rm S}_{\rm LL}=2$	$\frac{3}{4}$	1	$\frac{3}{4}$	0
S−P $\otimes$ S+P	$g^{\rm S}_{\rm RR}=2$	$\frac{3}{4}$	-1	$-\frac{3}{4}$	0
S $\otimes$ S	$g^{\rm S}_{\rm LL}=g^{\rm S}_{\rm RL}=g^{\rm S}_{\rm LR}=g^{\rm S}_{\rm RR}=1$	$\frac{3}{4}$	0	0	0
P $\otimes$ P	$-g^{\rm S}_{\rm LL}=g^{\rm S}_{\rm RL}=g^{\rm S}_{\rm LR}=-g^{\rm S}_{\rm RR}=1$	$\frac{3}{4}$	0	0	0
S+P $\otimes$ S+P	$g^{\rm S}_{\rm LR}=2$	$\frac{3}{4}$	-1	$-\frac{3}{4}$	0
S−P $\otimes$ S−P	$g^{\rm S}_{\rm RL}=2$	$\frac{3}{4}$	1	$\frac{3}{4}$	0
T $\otimes$ T	$g^{\rm T}_{\rm LR}=g^{\rm T}_{\rm RL}=\sqrt{\frac{1}{6}}$	$\frac{1}{4}$	0	0	0

here $\mathcal{P}_R^\tau$ is the fractional contribution of the right-handed couplings to the leptonic decay width, which appears in the left-right symmetric models [2–5].

Of particular importance is the η parameter, which vanishes in the SM. The largest contribution to this parameter comes from the interference between the dominant g_{LL}^V coupling and a scalar coupling:

$$\eta \simeq \frac{1}{2}\Re(g_{RR}^S g_{LL}^{V*}), \tag{16}$$

which appears in the models with the charged Higgs bosons [6–8]. Also η is the only MP which contributes to the leptonic τ decay width:

$$\Gamma(\tau \to \ell\nu\nu) \approx \frac{M_\tau^5 G^2}{192\pi^3}\left(1 + 4\eta\frac{m_\ell}{M_\tau}\right) \tag{17}$$

Its effect is maximal in the low energy part of the outgoing lepton spectrum. Due to the suppression of this term by a factor of m_ℓ/M_τ it is almost impossible to measure η in $\tau^- \to e^-\bar{\nu}_e\nu_\tau$ decays. As a result η can be measured only in $\tau^- \to \mu^-\bar{\nu}_\mu\nu_\tau$ decays, where the suppression is only $\simeq 1/17$.

The last, most precise, measurements of MP in τ decays were done by CLEO and ALEPH collaborations [9], [10], see Table 2. It is seen that

Table 2: The most precise measurements of MP in leptonic τ decays. In the second column measured values are shown (the first error is statistical and the second is systematic one). Current PDG average values are shown in the fourth column.

Michel parameter	Measured value	Exp.	PDG average	SM value
ρ (e or μ)	$0.747 \pm 0.010 \pm 0.006$	CLEO-97	0.749 ± 0.008	3/4
η (e or μ)	$0.012 \pm 0.026 \pm 0.004$	ALEPH-01	0.015 ± 0.021	0
ξ (e or μ)	$1.007 \pm 0.040 \pm 0.015$	CLEO-97	0.981 ± 0.031	1
$\xi\delta$ (e or μ)	$0.745 \pm 0.026 \pm 0.009$	CLEO-97	0.744 ± 0.022	3/4
$\xi_{\rm h}$ (all hadr.)	$0.992 \pm 0.007 \pm 0.008$	ALEPH-01	0.997 ± 0.007	1

statistical accuracy dominates in all measurements, so with much larger data sample collected at Belle it is possible to improve these results and achieve several times better accuracy. More precise measurement of MP will provide more severe test of the SM as well as more stringent limits on the parameters of the new particles and interactions beyond the SM.

2 Method (1st part)

Measurement of ξ and δ requires the knowledge of the τ spin direction. In the experiments at e^+e^- colliders with unpolarized $e^\mp$ beams the average polarization of single τ is zero. However, effect of spin-spin correlations between τ^+ and τ^- produced in the reaction $e^+e^- \to \tau^+\tau^-$ can be used [11]. The differential cross section of this reaction in the center-of-mass system (CMS) is given by formula:

$$\frac{d\sigma(\vec{\zeta}^{*-}, \vec{\zeta}^{*+})}{d\Omega} = \frac{\alpha^2}{64E_\tau^2}\beta_\tau(D_0 + D_{ij}\zeta_i^{*-}\zeta_j^{*+})$$

$$D_0 = 1 + \cos^2\theta + \frac{1}{\gamma_\tau^2}\sin^2\theta$$

$$D_{ij} = \begin{pmatrix} (1+\frac{1}{\gamma_\tau^2})\sin^2\theta & 0 & \frac{1}{\gamma_\tau}\sin 2\theta \\ 0 & -\beta_\tau^2\sin^2\theta & 0 \\ \frac{1}{\gamma_\tau}\sin 2\theta & 0 & 1+\cos^2\theta - \frac{1}{\gamma_\tau^2}\sin^2\theta \end{pmatrix} \qquad (18)$$

where $\vec{\zeta}^{*\mp}$ is polarisation vector of $\tau^\mp$ in the $\tau^\mp$ rest frame (unitary vector along $\tau^\mp$ spin direction). Asterisk marks parameters measured in the associated τ rest frame. E_τ, $\gamma_\tau = E_\tau/M_\tau$, $\beta_\tau = P_\tau/E_\tau$ and θ are energy, Lorentz factor, velocity of τ (in the units of c) and polar angle of τ^- momentum direction respectively. The fraction of events with anti-correlated τ^- and τ^+ helicities is $\frac{2\gamma_\tau^2}{2\gamma_\tau^2+1}$ ($\approx 95\%$ at Belle), see also Fig.2, hence if we know helicity of one τ we can identify helicity of the other τ with the probability of 95%.

The main idea of our method is to consider events where both taus decay to the particular final states. One (signal) $\tau^\mp$ decays leptonically ($\tau^\mp \to \ell^\mp\nu\nu$, $\ell = e,\ \mu$) and the $\tau^\pm \to \pi^\pm\pi^0\nu$ decay serves as spin analyser. We chose $\tau^\pm \to \pi^\pm\pi^0\nu$ decay as a spin analyser in our analysis because it has the largest branching fraction as well as properly studied dynamics [12]. The hadronic current for this decay mode can be written in the general form as:

$$J^\mu = < \rho|\bar{d}\gamma^\mu(c_V + c_A\gamma^5)u|0 >, \qquad (19)$$

where c_V and c_A are complex numbers describing contribution of vector and axial vector components to the charged weak current of quarks. The differential decay width of $\tau^\pm(p, \vec{\zeta'}^*) \to \pi^\pm(k_1)\pi^0(k_2)\nu(q)$ (see also Fig.3) is:

$$\frac{d\Gamma(\tau^\pm)}{dm_{\pi\pi}^2 d\Omega_\rho^* d\tilde{\Omega}_\pi} = \kappa_\rho(A' \mp \xi_\rho\vec{B'}\vec{\zeta'}^*)W(m_{\pi\pi}^2) = \kappa_\rho A' W(m_{\pi\pi}^2)(1 \mp \xi_\rho\vec{H}_\rho\vec{\zeta'}^*);$$

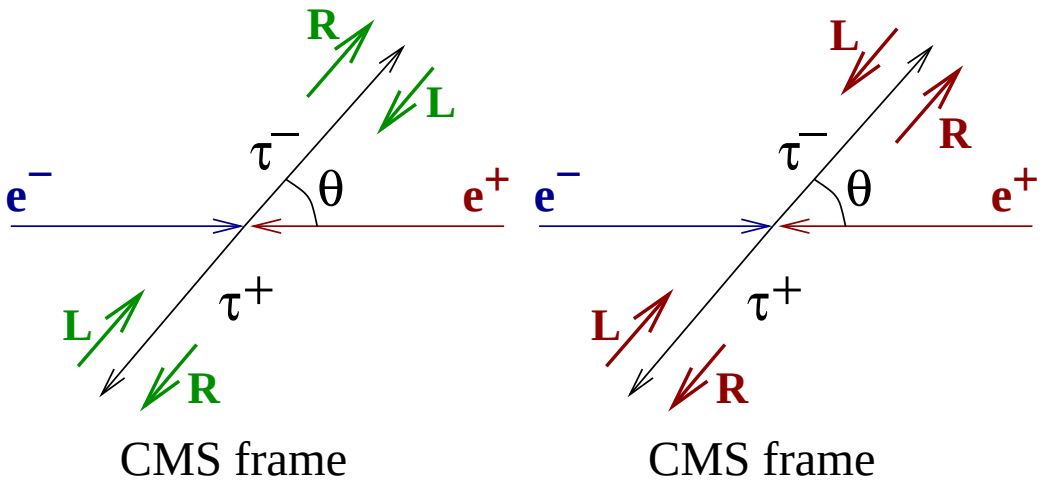

Figure 2: Helicity configurations of taus in $e^+e^- \to \tau^+\tau^-$: $\frac{2\gamma_\tau^2}{2\gamma_\tau^2+1}$ fraction ($\approx 95\%$) with anti-correlated helicities (left), $\frac{1}{2\gamma_\tau^2+1}$ fraction ($\approx 5\%$) with correlated helicities (right).

$$\xi_\rho = -\frac{2Re(c_V^* c_A)}{|c_V|^2+|c_A|^2},\ A' = 2(q,Q)Q_0^* - Q^2 q_0^*,\ \vec{B}' = Q^2\vec{K}^* + 2(q,Q)\vec{Q}^*;$$

$$W = |F_\pi(m_{\pi\pi}^2)|^2 \frac{p_\rho^*(m_{\pi\pi}^2, M_\tau)\tilde{p}_\pi(m_{\pi\pi}^2)}{M_\tau m_{\pi\pi}},\ \vec{H}_\rho = \vec{B}'/A', \tag{20}$$

$$\tilde{p}_\pi(m_{\pi\pi}^2) = \frac{\sqrt{(m_{\pi\pi}^2 - (m_\pi + m_{\pi^0})^2)(m_{\pi\pi}^2 - (m_\pi - m_{\pi^0})^2)}}{2m_{\pi\pi}}, \tag{21}$$

$$p_\rho^*(m_{\pi\pi}^2, M_\tau) = \frac{M_\tau}{2}\left(1 - \frac{m_{\pi\pi}^2}{M_\tau^2}\right), \tag{22}$$

where $F_\pi(m_{\pi\pi}^2)$ is charged pion form factor, parameters marked by tilde are calculated in the ρ rest frame. In our analysis we use pion form factor measured in $\tau^- \to \pi^-\pi^0\nu_\tau$ decay at Belle [12]. It was also embedded into TAUOLA generator [13, 14] It is seen from Eq. 20 that Michel formalism for the $\tau^- \to \rho^-\nu_\tau$ decay is represented by only one parameter, $\xi_\rho = -\frac{2Re(c_V^* c_A)}{|c_V|^2+|c_A|^2} = -h_{\nu_\tau}$, which is equal to the minus τ neutrino helicity, $\xi_\rho = 1$ in the SM. It is also seen that $\tau^\mp \to \rho^\mp\nu$ decays with polarimeter vector $\vec{H}_\rho$ along τ^- spin (against τ^+ spin) are preferred, so the average polarimeter vector indicates helicity of decaying tau (spin analyser side). Using

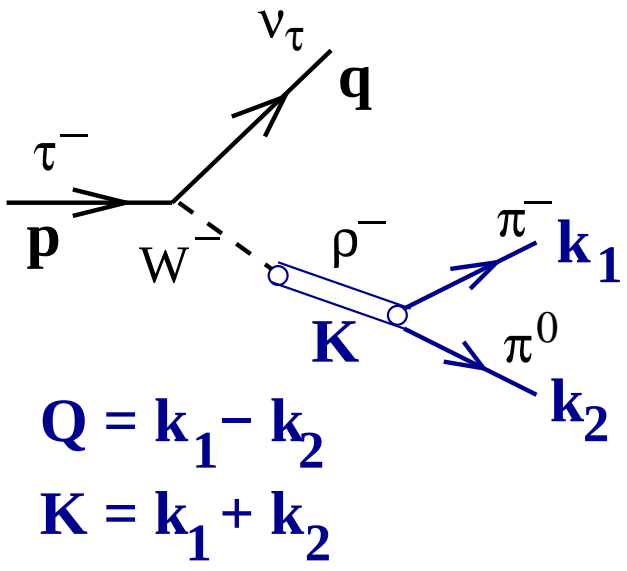

Figure 3: Mechanism of $\tau^- \to \pi^-\pi^0\nu_\tau$.

spin-spin correlation of taus we infer the helicity of the opposite tau (signal side). The idea is also graphically demonstrated in Fig.4. As a result analysing ($\tau^\mp \to \ell^\mp\nu\nu$; $\tau^\pm \to \rho^\pm(\to \pi^\pm\pi^0)\nu$) (shortly $\ell-\rho$) events we extract: ρ, η, $\xi_\rho\xi$ and $\xi_\rho\xi\delta$ parameters. Events with ($\tau^\mp \to \rho^\mp\nu$; $\tau^\pm \to \rho^\pm\nu$) configuration (shortly $\rho-\rho$) are used to measure ξ_ρ^2 and extract ξ_ρ (sign of ξ_ρ was reliably established by ARGUS [16]). After that we can calculate pure ξ and $\xi\delta$.

To calculate polarimeter vector of spin analyser τ flight direction is needed, however it can not be measured directly at Belle. Nevertheless in the $\ell^\mp-\rho^\pm$ events the direction of τ axis can be constrained by arc, which is determined by three angles: ψ - angle between $\rho^\pm$ and $\tau^\pm$ momenta, χ - angle between $\ell^\mp$ and $\tau^\mp$ momenta, and α - measurable angle between $\rho^\pm$ and $\ell^\mp$ momenta. Considering τ neutrino(antineutrino) mass from $\tau^\pm \to \rho^\pm\nu$ decay to be 0 we get:

$$\cos\psi = \frac{2E_\tau E_\rho - M_\tau^2 - m_{\pi\pi^0}^2}{2p_\tau p_\rho}. \tag{23}$$

From the criteria on the invariant mass of two neutrinos from $\tau^\mp \to \ell^\mp\nu\nu$

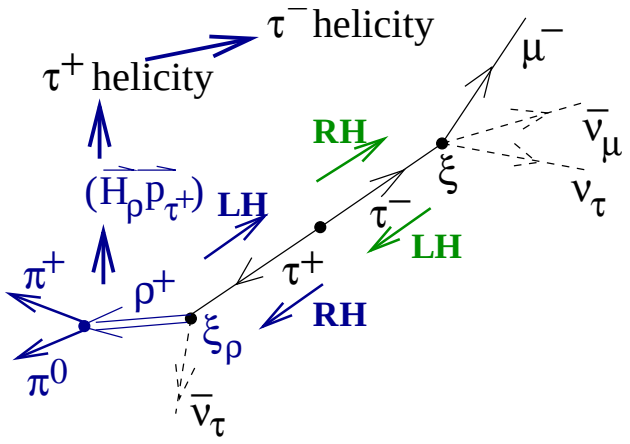

Figure 4: Idea of the method.

decay, $0 < m^{\ell}_{\nu\nu} \leq (M_\tau - m_\ell)$, we get:

$$\frac{2E_\tau E_\ell - M_\tau^2 - m_\ell^2}{2p_\tau p_\ell} < \cos\chi \leq \frac{E_\tau E_\ell - M_\tau m_\ell}{p_\tau p_\ell}. \tag{24}$$

$$\cos\alpha = \sin\theta_\rho \sin\theta_\ell \cos(\varphi_\rho - \varphi_\ell) + \cos\theta_\rho \cos\theta_\ell. \tag{25}$$

Geometrically the directions of τ axis are given by the intersection of the reflected cone of allowed $\tau^{\pm}$ flight directions (for particular ψ angle) and a sector of the $\tau^{\mp}$ flight directions, determined by allowed range of χ angle, see Fig.5. Finally arc of allowed τ axis directions, $(\Phi_1,\ \Phi_2)$, is determined by two angles:

$$\Phi_1 = \pi + \arcsin\left(\frac{\cos\psi\cos\alpha + \cos\chi}{\sin\psi\sin\alpha}\right),$$

$$\Phi_2 = 2\pi - \arcsin\left(\frac{\cos\psi\cos\alpha + \cos\chi}{\sin\psi\sin\alpha}\right). \tag{26}$$

To demonstrate spin-spin correlation of taus we introduce special helicity sensitive variable ω, suggested in [17]. It is defined as the projection of the ρ polarimeter vector to the τ flight direction in the τ rest frame averaged over the $(\Phi_1,\ \Phi_2)$ arc:

$$\omega = \frac{1}{\Phi_2 - \Phi_1}\int_{\Phi_1}^{\Phi_2} (\vec{H}_{\rho^\pm}, \vec{n}_{\tau^\pm}) d\Phi = < (\vec{H}_{\rho^\pm}, \vec{n}_{\tau^\pm}) >_{\Phi_\tau} \tag{27}$$

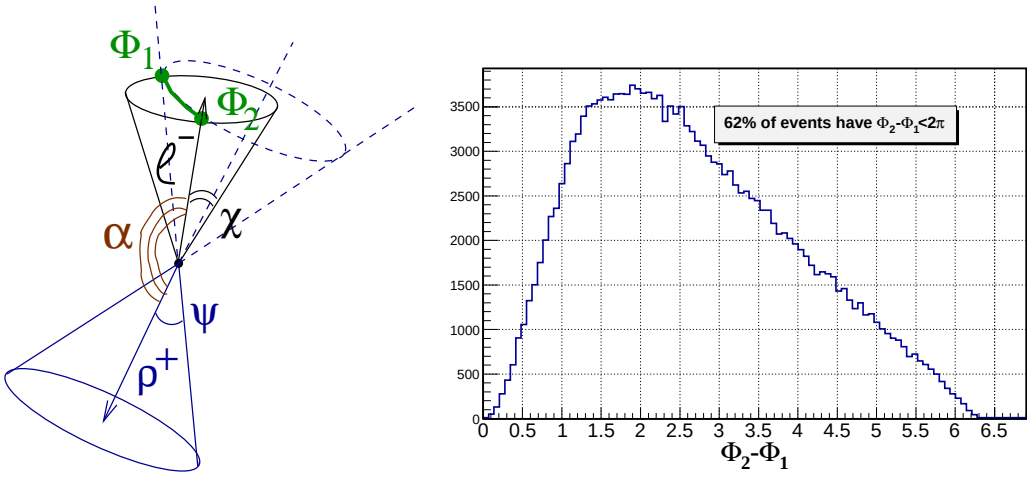

Figure 5: Arc of allowed τ axis directions (Φ_1, Φ_2) (left), distribution of $\Phi_2 - \Phi_1$ for the events with $\Phi_2 - \Phi_1 < 2\pi$ (with a fraction of 62%) (right).

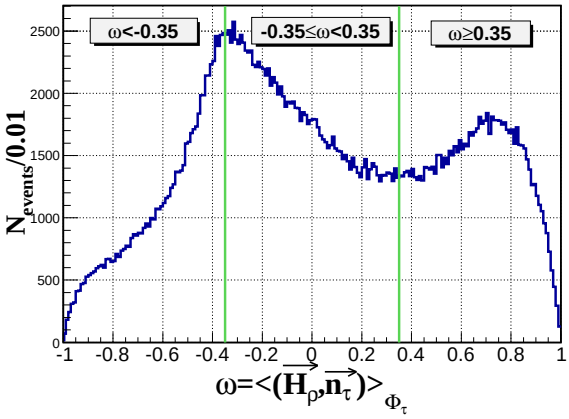

Figure 6: MC distribution of $\omega =< (\vec{H}_{\rho^\pm}, \vec{n}_{\tau^\pm}) >_{\Phi_\tau}$.

MC distribution of ω is shown in Fig.6. Selecting events with different values of ω we form samples with different average τ helicities, which can be demonstrated by different shapes of the lepton momentum distributions in these samples, see Fig.7. Dependence between ω and helicity states of taus is

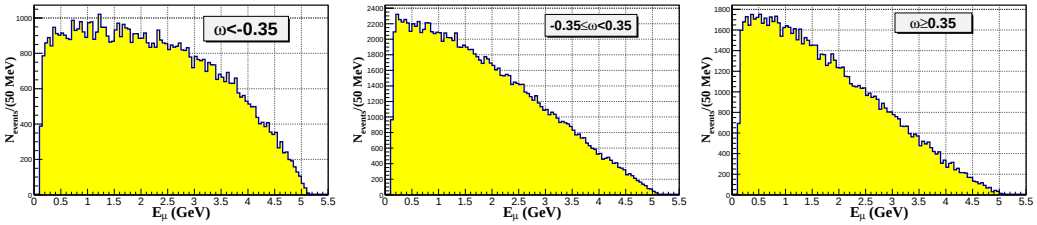

Figure 7: Muon energy distributions of $\mu - \rho$ events selected in three ω ranges: $\omega < -0.35$ (left), $-0.35 \leq \omega < 0.35$ (middle), $\omega \geq 0.35$ (right)

demonstrated in Fig.8. It is clearly seen that for the positive ω the preferred lepton momentum is directed against momentum of the parent tau, hence lepton gets negative boost and low momenta are dominant, see Fig.7(right). In turn for the negative ω the preferred lepton momentum is along momentum of the parent tau, as a result, due to the positive boost, we have notable excess of events with high momenta, see Fig.7(left).

Figure 8: Diagram clarifying dependence between ω and helicity states of taus.

To write the total differential cross section for $\ell - \rho$ events we follow the way initially proposed in [18]. The detailed development of the approach for the $\ell - \rho$ case was done in [19–21].

Combining differential cross section of the reaction $e^+e^- \to \tau^-(\vec{\zeta}^{*-})\tau^+(\vec{\zeta}^{*+})$ given by Eq. 18, differential decay width of $\tau^\pm(\vec{\zeta}^{*\prime}) \to \rho^\pm\nu$ given by Eq. 20 and differential decay width of $\tau^\mp(\vec{\zeta}^*) \to \ell^\mp\nu\nu$ (see also Eq. 8):

$$\frac{d\Gamma(\tau^\mp(\vec{\zeta}^*) \to \ell^\mp\nu\nu)}{dx^* d\Omega_\ell^*} = \kappa_\ell(A(x^*) \mp \xi\vec{n}_\ell^*\vec{\zeta}^* B(x^*)),$$

$$A(x^*) = A_0(x^*) + \rho A_1(x^*) + \eta A_2(x^*),\ B(x^*) = B_1(x^*) + \delta B_2(x^*),$$
$$A_0(x^*) = x^*(1-x^*)\sqrt{x^{*2} - x_0^{*2}},\ A_1(x^*) = \frac{2}{9}(4x^{*2} - 3x^* - x_0^{*2})\sqrt{x^{*2} - x_0^{*2}},$$
$$A_2(x^*) = x_0^*(1-x^*)\sqrt{x^{*2} - x_0^{*2}},\ B_1(x^*) = \frac{1}{3}(x^{*2} - x_0^{*2})(1-x^*),$$
$$B_2(x^*) = \frac{2}{9}(x^{*2} - x_0^{*2})(4x^* - 4 + \sqrt{1 - x_0^{*2}}),$$
$$x^* = \frac{E_\ell^*}{E_{\ell max}^*},\ x_0^* = \frac{m_\ell}{E_{\ell max}^*},\ E_{\ell max}^* = \frac{M_\tau}{2}(1 + \frac{m_\ell^2}{M_\tau^2}). \tag{28}$$

we can write the total differential cross section for the $\ell - \rho$ events in the form:

$$\frac{d\sigma(\ell^\mp, \rho^\pm)}{dE_\ell^* d\Omega_\ell^* d\Omega_\rho^* dm_{\pi\pi}^2 d\tilde{\Omega}_\pi d\Omega_\tau} = \kappa_\ell \kappa_\rho \frac{\alpha^2 \beta_\tau}{64 E_\tau^2} \big(D_0 A' A(E_\ell^*) + \xi_\rho \xi_\ell D_{ij} n_{\ell i}^* B_j' B(E_\ell^*) \big) W(m_{\pi\pi}^2) \tag{29}$$

The cross section above depends also on parameters in the associated tau rest frames, writing it through the measured variables only and integrating over allowed directions of tau axis we get:

$$\frac{d\sigma(\ell^\mp, \rho^\pm)}{dp_\ell d\Omega_\ell dp_\rho d\Omega_\rho dm_{\pi\pi}^2 d\tilde{\Omega}_\pi} = \int_{\Phi_1}^{\Phi_2} \frac{d\sigma(\ell^\mp, \rho^\pm)}{dE_\ell^* d\Omega_\ell^* d\Omega_\rho^* dm_{\pi\pi}^2 d\tilde{\Omega}_\pi d\Omega_\tau} \left| \frac{\partial(E_\ell^*, \Omega_\ell^*, \Omega_\rho^*, \Omega_\tau)}{\partial(p_\ell, \Omega_\ell, p_\rho, \Omega_\rho, \Phi_\tau)} \right| d\Phi_\tau, \tag{30}$$

$$\left| \frac{\partial(E_\ell^*, \Omega_\ell^*, \Omega_\rho^*, \Omega_\tau)}{\partial(p_\ell, \Omega_\ell, p_\rho, \Omega_\rho, \Phi_\tau)} \right| = \left| \frac{\partial(E_\ell^*, \Omega_\ell^*)}{\partial(p_\ell, \Omega_\ell)} \right| \cdot \left| \frac{\partial(\Omega_\rho^*, \Omega_\tau)}{\partial(p_\rho, \Omega_\rho, \Phi_\tau)} \right|, \tag{31}$$

$$\left| \frac{\partial(E_\ell^*, \Omega_\ell^*)}{\partial(p_\ell, \Omega_\ell)} \right| = \frac{p_\ell^2}{E_\ell p_\ell^*},\ \left| \frac{\partial(\Omega_\rho^*, \Omega_\tau)}{\partial(p_\rho, \Omega_\rho, \Phi_\tau)} \right| = \frac{M_\tau}{|\vec{p}_\tau|} \frac{p_\rho}{E_\rho p_\rho^*}, \tag{32}$$

details of the calculation of these Jacobians can be also found in [20]. We extract 4 Michel parameters simultaneously in the unbinned maximum likelihood fit of $\ell - \rho$ events in the 9D phase space

($\vec{z} = (p_\ell,\ \cos\theta_\ell,\ \phi_\ell,\ p_\rho,\ \cos\theta_\rho,\ \phi_\rho,\ m_{\pi\pi},\ \cos\tilde{\theta}_\pi,\ \tilde{\phi}_\pi)$) in CMS. To write the following equations shortly it is convenient to introduce vector $\vec{\Theta} = (1,\ \rho,\ \eta,\ \xi_\rho\xi_\ell,\ \xi_\rho\xi_\ell\delta_\ell)$. The probability density function (PDF) for individual k-th event is written in the form:

$$\mathcal{P}^{(k)} = \frac{\mathcal{F}^{(k)}(\vec{\Theta})}{\mathcal{N}(\vec{\Theta})},\ \mathcal{F}^{(k)}(\vec{\Theta}) = \mathcal{F}(\vec{z}^{(k)}, \vec{\Theta}) = \frac{d\sigma(\ell^\mp, \rho^\pm)}{d\vec{z}^{(k)}},\ \mathcal{N}(\vec{\Theta}) = \int \mathcal{F}(\vec{z}, \vec{\Theta}) d\vec{z} \tag{33}$$

Both $\mathcal{F}^{(k)}(\vec{\Theta})$ and $\mathcal{N}(\vec{\Theta})$ are linear functions on $\vec{\Theta}$:

$$\mathcal{F}^{(k)}(\vec{\Theta}) = \sum_{i=0}^{4} A_i^{(k)}\Theta_i,\ A_i^{(k)} = A_i(\vec{z}^{(k)}),\ i = 0 \div 4, \tag{34}$$

$$\mathcal{N}(\vec{\Theta}) = \sum_{i=0}^{4} C_i\Theta_i,\ C_i = \int A_i(\vec{z})d\vec{z}. \tag{35}$$

In this case likelihood function (L) and logarithmic likelihood function ($\mathcal{L}$) for N events is written as:

$$L = \prod_{k=1}^{N} \mathcal{P}^{(k)},\ \mathcal{L} = -\ln L = N\ln\mathcal{N}(\vec{\Theta}) - \sum_{k=1}^{N}\ln\mathcal{F}^{(k)}(\vec{\Theta}), \tag{36}$$

$$\mathcal{L} = N\ln\left(\sum_{i=0}^{4} C_i\Theta_i\right) - \sum_{k=1}^{N}\ln\left(\sum_{i=0}^{4} A_i^{(k)}\Theta_i\right) \tag{37}$$

As a result whole statistics to be fitted is represented by a set of $5N$ coefficients $A_i^{(k)}$ ($k = 1 \div N,\ i = 0 \div 4$), which are calculated only once per fit. Four normalisation coefficients C_i ($i = 0 \div 4$) can be calculated with help of the MC simulation. Suppose we have $N_{\rm MC}$ MC events, which were simulated with particular set of Michel parameters $\vec{\Theta}^{\rm MC}$. Reweighting each event we can calculate normalization for arbitrary set $\vec{\Theta}$ (summation is implied over the repeated index):

$$\mathcal{N}(\vec{\Theta}) = \frac{1}{N_{MC}}\sum_{k=1}^{N_{MC}} w^{(k)},\ w^{(k)} = \frac{A_i^{(k)}\Theta_i}{A_j^{(k)}\Theta_j^{MC}} = B_m^{(k)}\Theta_m,\ B_m^{(k)} = \frac{A_m^{(k)}}{A_j^{(k)}\Theta_j^{MC}} \tag{38}$$

$$\mathcal{N}(\vec{\Theta}) = C_i\Theta_i,\ C_i = \frac{1}{N_{MC}}\sum_{k=1}^{N_{MC}} B_i^{(k)} \tag{39}$$

This approach can be easily modified to take into account detection efficiency. Distribution of the detected events in the full phase space is given by modified function:

$$\mathcal{F}'(\vec{z},\vec{\Theta}) = \mathcal{F}(\vec{z},\vec{\Theta})\epsilon(\vec{z}), \tag{40}$$

modified normalisation is:

$$\mathcal{N}'(\vec{\Theta}) = \int \mathcal{F}(\vec{z},\vec{\Theta})\epsilon(\vec{z})d\vec{z} \tag{41}$$

Suppose we fit $N_{\rm sel}$ experimental events. MC data sample of N_{MC} generated events (with $\vec{\Theta}^{SM}$) and $N_{MC}^{\rm sel}$ selected events is used to calculate normalisation. Logarithmic likelihood function is:

$$\mathcal{L} = N_{\rm sel} \ln \mathcal{N}'(\vec{\Theta}) - \sum_{k=1}^{N_{\rm sel}} \ln\Big(\mathcal{F}^{(k)}(\vec{\Theta}) \epsilon(\vec{z}) \Big) =$$

$$= N_{\rm sel} \ln(C'_i \Theta_i) - \sum_{k=1}^{N_{\rm sel}} \ln(A_i^{(k)} \Theta_i) - \cancel{\sum_{k=1}^{N_{\rm sel}} \ln \epsilon(\vec{z})}, \; C'_i = \frac{1}{N_{MC}} \sum_{k=1}^{N_{MC}^{\rm sel}} B_i^{(k)} \qquad (42)$$

As it is seen from Eq. 42 explicit knowledge of efficiency $\epsilon(\vec{z})$ is not needed. Term with efficiency in the likelihood function can be omitted because it does not depend on Michel parameters. In the calculation of normalisation coefficients C'_i efficiency is automatically taken into account.

We embedded Michel formalism for leptonic τ decays in TAUOLA generator [13] according [22] and performed series of fits of large MC samples (of 10 million events each), generated for different values of MP. In the fit of the **generated** samples we confirmed that the developed method allows us to extract Michel parameters without bias (within statistical uncertainties of $\sim 10^{-3}$). We observed that unknown tau axis direction (integration over Φ_τ in the formula for the differential cross section) results in only ~ 1.4 inflation of the MP statistical uncertainties. Also we realized that even with huge Belle statistics we can exctract η MP from the fit of $\mu - \rho$ events only. For the $e - \rho$ events the term with η MP is strongly suppressed by $m_{\rm e}/M_\tau$, see Eq. 8. However, due to the notable correlation between ρ and η MP we should fit $\mu - \rho$ and $e - \rho$ events simultaneously to reach the best possible accuracy for both ρ and η MP.

In the precise studies it is important to take into account effects of the higher order corrections. These corrections will distort all distributions determined by Born cross section ($O(\alpha^2)$), hence they should be taken into account in PDF. In the total cross section of the reaction $e^+e^- \to \tau^\mp(\to \ell^\mp \nu\nu)\tau^\pm(\to \pi^\pm \pi^0 \nu)$ we should take into account all electroweak corrections at least of the order of $O(\alpha^3)$, so that the relative contributions to the Born cross section of the order of 1% ($\sim \alpha$) would be controlled properly. Higher order electroweak corrections can be separated into two groups: corrections to the $\tau^+\tau^-$ production cross section (i.e. $e^+e^- \to \tau^+\tau^-(\gamma)$) and so called radiative corrections to the tau decays: $\tau^\mp \to \ell^\mp \nu\nu(\gamma)$ and $\tau^\pm \to \pi^\pm \pi^0 \nu(\gamma)$.

To include radiative corrections in PDF we use analytical (main) and MC-based approaches. This allows us to study related systematic uncertainties. In the MC-based approach we rely on the radiative photon momentum distribution, which is produced by KKMC+PHOTOS [32,33] MC generator, and use it to calculate visible differential cross section used in PDF.

Corrections to the $\tau^+\tau^-$ production cross section include the following contributions (see also Fig. 9):

- Low polar angle (collinear) initial state radiation (ISR) (Fig. 9(b));
- Final state radiation (FSR) (Fig. 9(c)) and its interference with ISR;
- Interference of the box (Fig. 9(d),(e)) and Born diagrams (a);
- Interference of the Z^0-exchange (Fig. 9(f)) and Born diagrams;
- Interference of the $\gamma - \tau^+\tau^-$ vertex correction (Fig. 9(g)) and Born diagrams;
- Vacuum polarization (Fig. 9(h));

The description of these corrections is based on the approach developed in the papers [23]- [29]. Collinear ISR provides the largest contribution, hence the largest influence on the energy spectrum of outgoing lepton (electron or muon from consequent leptonic tau decay), see Fig. 10. According to [23]-[25] visible differential cross section with effects of QED corrections can be written in the form (dPS $= dp_\ell d\Omega_\ell dp_\rho d\Omega_\rho dm^2_{\pi\pi} d\tilde{\Omega}_\pi$):

$$\frac{d\sigma_{\rm vis}(s)}{\rm dPS} = \int\limits_0^1 \int\limits_0^1 dx_1 dx_2 D(x_1,s)D(x_2,s)\times$$

$$\times\left(\frac{d\tilde{\sigma}_B(s,x_1,x_2)}{\rm dPS}(1+\frac{2\alpha}{\pi}K) + \frac{d\tilde{\sigma}_c(s,x_1,x_2)}{\rm dPS}\right)$$

$$+\frac{\alpha}{\pi}\int\limits_\Delta^1 \frac{dx_1}{x_1}\left[(1-x_1+\frac{x_1^2}{2})\ln\frac{\theta_0^2}{4}+\frac{x_1^2}{2}\right]\frac{d\tilde{\sigma}_B(s,x_1,0)}{\rm dPS}$$

$$+\frac{\alpha}{\pi}\int\limits_\Delta^1 \frac{dx_2}{x_2}\left[(1-x_2+\frac{x_2^2}{2})\ln\frac{\theta_0^2}{4}+\frac{x_2^2}{2}\right]\frac{d\tilde{\sigma}_B(s,0,x_2)}{\rm dPS}$$

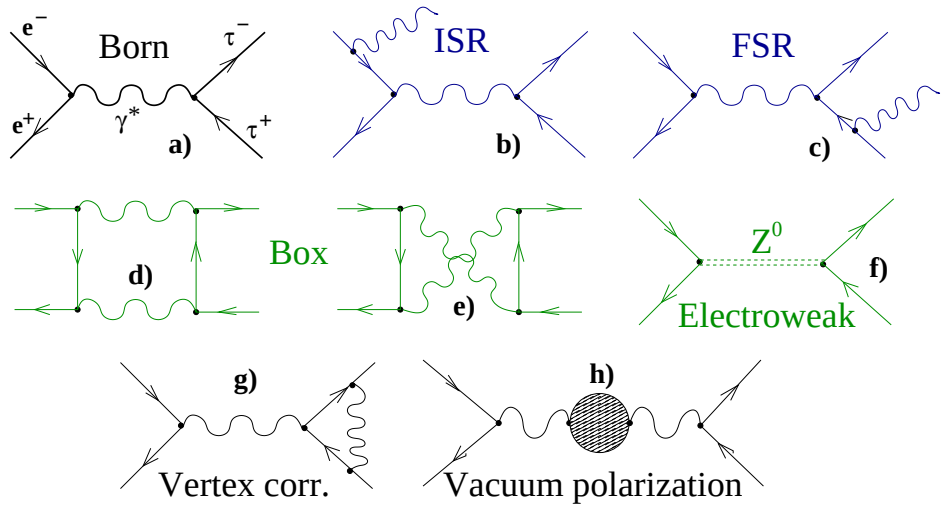

Figure 9: Diagrams used to evaluate all $O(\alpha^3)$ electroweak corrections to the $\tau^+\tau^-$ production cross section: (a) Born diagram, (b) initial state radiation (ISR), (c) final state radiation (FSR), (d) and (e) box diagrams, (f) Z^0-boson exchange, (g) $\gamma - \tau^+\tau^-$ vertex correction, (h) vacuum polarisation. For the diagrams (d)-(g) only $O(\alpha^3)$ interference terms with the Born diagram are taken into account in the cross section. Charge-odd part of the cross section comes from the interference of the ISR and FSR diagrams as well as box and Born diagrams, and Z^0-exchange and Born diagrams.

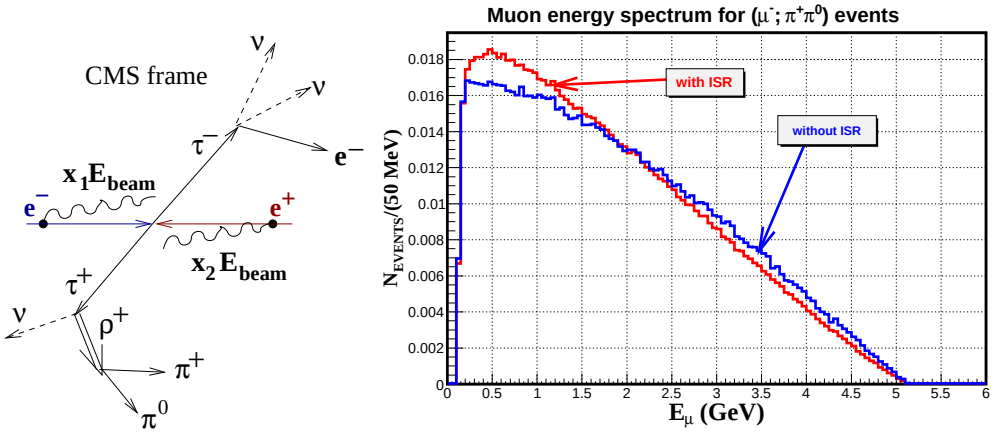

Figure 10: Initial state radiation (left). CMS energy spectrum of muon for $(\mu^-;\ \rho^+)$ events (right). Spectrum with effect of ISR is shown by red line, without ISR - by blue line.

$$+\frac{\alpha^3}{32\pi^2 s}\int\limits_{\substack{\omega>\Delta\varepsilon\\ \theta_\gamma>\theta_0}}^{E_\tau\beta_\tau^2}\frac{dR_{\rm hard}}{\rm dPS}\sqrt{1-\frac{4M_\tau^2}{(s-2\sqrt{s}\omega)}}\omega d\omega d\Omega_\gamma$$

$$+\frac{2\alpha}{\pi}\left[\frac{1+\beta_\tau^2}{2\beta_\tau}\ln\frac{1+\beta_\tau}{1-\beta_\tau}-1+2\ln\frac{1-\beta_\tau\cos\theta_\tau}{1+\beta_\tau\cos\theta_\tau}\right]\ln(\Delta)\frac{d\tilde{\sigma}_B(s,0,0)}{\rm dPS}, \qquad (43)$$

$$\frac{d\tilde{\sigma}_B}{\rm dPS}=\frac{1}{|1-\Pi(s')|^2}\frac{d\sigma(s')}{dp'_\ell d\Omega'_\ell dp'_\rho d\Omega'_\rho dm^2_{\pi\pi}d\tilde{\Omega}_\pi}\left|\frac{\partial(p'_\ell,\Omega'_\ell)}{\partial(p_\ell,\Omega_\ell)}\right|\left|\frac{\partial(p'_\rho,\Omega'_\rho)}{\partial(p_\rho,\Omega_\rho)}\right|, \qquad (44)$$

$$\left|\frac{\partial(p'_\alpha,\Omega'_\alpha)}{\partial(p_\alpha,\Omega_\alpha)}\right|=\frac{p^2_\alpha}{p'^2_\alpha}\frac{E'_\alpha}{E_\alpha},\ \alpha=\ell,\rho, \qquad (45)$$

where: $s'=s(1-x_1)(1-x_2)$, $\Pi(s')$ is vacuum polarisation operator taken from [30], [31] (see also Fig. 11), $\frac{d\sigma(s')}{dp'_\ell d\Omega'_\ell dp'_\rho d\Omega'_\rho dm^2_{\pi\pi}d\tilde{\Omega}_\pi}$ is the differential cross section of $\tau^+\tau^-$ production in the $\tau^+\tau^-$ rest frame, it is determined by Eq. 30; $|\frac{\partial(p'_i,\Omega'_i)}{\partial(p_i,\Omega_i)}|$ $(i=\ell,\ \rho)$ is Jacobian of the transformation from the $\tau^+\tau^-$ rest frame to the Belle CMS. Parameters marked by prime are measured in the $\tau^+\tau^-$ rest frame ($\tau^+\tau^-$ system moves against radiative gamma(s)). The first and the largest term in Eq. 43 describes the cross section with effects of the collinear ISR, here $D(x,s)=x^{\beta/2-1}h(x)$ is the probability function for initial

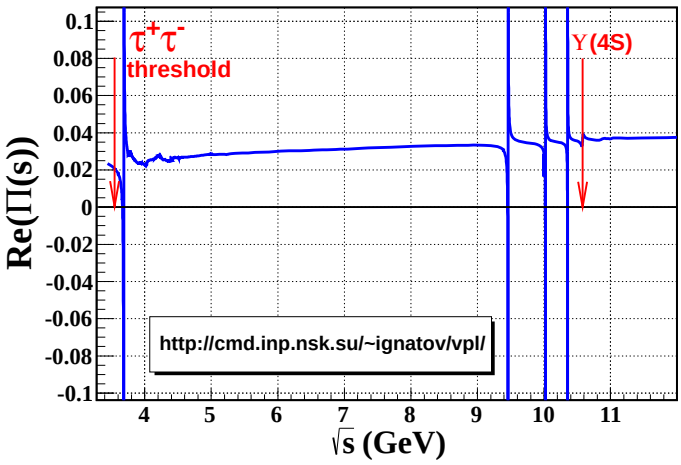

Figure 11: $\mathrm{Re}(\Pi(s))$ as a function of $\sqrt{s}$.

$e^{\mp}$ to emit ISR γ-quantum jet carrying $x_{1,2}$ part of $e^{\mp}$ energy $E_{\rm beam} = \sqrt{s}/2$, $\beta = \frac{2\alpha}{\pi}(\ln\frac{s}{m_e^2} - 1)$, $h(x)$ is smooth limited function [23], [26]. Multiplicative part of the higher order corrections are described by K-factor in Eq. 43 and the remaining part (including spin-spin correlation term) is introduced by the $\frac{d\tilde{\sigma}_c}{\rm dPS}$ term:

$$\frac{d\tilde{\sigma}_c}{\rm dPS} = \frac{1}{|1-\Pi(s')|^2}\frac{d\sigma_c(s')}{dp'_\ell d\Omega'_\ell dp'_\rho d\Omega'_\rho dm^2_{\pi\pi} d\tilde{\Omega}_\pi}\left|\frac{\partial(p'_\ell,\Omega'_\ell)}{\partial(p_\ell,\Omega_\ell)}\right|\left|\frac{\partial(p'_\rho,\Omega'_\rho)}{\partial(p_\rho,\Omega_\rho)}\right|, \qquad (46)$$

where for the $\frac{d\sigma_c}{dp'_\ell d\Omega'_\ell dp'_\rho d\Omega'_\rho dm^2_{\pi\pi} d\tilde{\Omega}_\pi}$ cross section the formalism from [28] is used.

The large polar angle ($\theta_\gamma > \theta_0$) hard photon ($\omega > \Delta\varepsilon$) emission part of the cross section is introduced by the fourth term in Eq. 43. The radiator function, $R_{\rm hard}$, includes 3 contributions: ISR, FSR, and their interference [23]. The spin-spin correlation part of the $R_{\rm hard}$ is taken from [28]. It should be noted that special compensator terms are introduced (second and third term in Eq. 43) in the formalism to cancel the dependence of the total cross section on arbitrary parameters: θ_0 - minimal polar angle of hard photon, $\Delta = \Delta\varepsilon/E_{\rm beam}$ - normalized minimal energy of hard photon. The last, fifth term in Eq. 43 comes from the virtual and soft photon corrections, this is just Born cross section multiplied by correction factor.

It is worth noting that the radiative corrections result in the charge asymmetry of the total cross section. It is seen even in the virtual and soft photon

correction, where the term, containing $\cos\theta_\tau$ is antisymmetric on the charge conjugation ($\cos\theta_\tau \to -\cos\theta_\tau$).

The electroweak corrections due to the Z^0 exchange are described according to [28]. The corresponding unpolarized form factor $D_0(Z^0) \sim -1\% \cos\theta_\tau$ is proportional to the $\cos\theta_\tau$, hence introduces the forward-backward asymmetry of the order of 1% in the cross section. Spin-spin correlation tensor components are: $D_{xx} \sim -0.01\% \sin^2\theta_\tau$, $D_{yy} \sim 0.01\% \sin^2\theta_\tau$, $D_{zz} \sim -1\% \cos\theta_\tau$. Also it should be noted that there appeared linear dependence on the τ^+ and τ^- polarisations with corresponding components $D_z^{\tau^-}(Z^0) = D_z^{\tau^+}(Z^0) \sim 0.1\%(1+\cos\theta_\tau)^2$. In the fit of the large MC sample it was found that the influence of these corrections on the Michel parameters is of the order of 10^{-4} only.

Radiative corrections to the tau decays:

- Radiative leptonic decays $\tau^- \to \ell^- \bar{\nu}_\ell \nu_\tau \gamma$ (also called as internal bremsstrahlung). Analytical approach is based on: [34] ($\mathcal{O}(\alpha)$ order correction), [35] ($\mathcal{O}(\alpha^2 \ln^2(\frac{m_\mu}{m_e})$) order correction) and [36] ($\mathcal{O}(\alpha^2 \ln(\frac{m_\mu}{m_e})$) order correction) calculations. In the MC-based approach we rely on TAUOLA and PHOTOS generators [37, 38, 41–43].

- Radiative hadronic decay $\tau^- \to \pi^-\pi^0\nu_\tau\gamma$. In the analytical approach we use radiative form factor calculated in [39, 40]. PHOTOS generator [41–43] is used in the MC-based approach.

Event with radiative leptonic decay is shown in Fig. 12. In this case γ quantum is emitted by tau or by outgoing lepton (although 2 photons are symbolically shown in Fig. 12, in reality only one photon is emitted at a time and the process is described by two diagrams). To describe effect of radiative leptonic decays form factors $A(x^*)$ and $B(x^*)$ in Eq. 28 are modified as:

$$A(x^*) = A_0(x^*) + \rho A_1(x^*) + \eta A_2(x^*) + A_{\rm rad}(x^*),$$
$$B(x^*) = B_1(x^*) + \delta B_2(x^*) + B_{\rm rad}(x^*), \tag{47}$$

$$A_{\rm rad}(x^*) = \alpha \cdot a_1(x^*) + \alpha^2 \ln^2\left(\frac{M_\tau}{m_\ell}\right) \cdot a_2(x^*) + \alpha^2 \ln\left(\frac{M_\tau}{m_\ell}\right) \cdot a_3(x^*), \tag{48}$$

$$B_{\rm rad}(x^*) = \alpha \cdot b_1(x^*) + \alpha^2 \ln^2\left(\frac{M_\tau}{m_\ell}\right) \cdot b_2(x^*) + \alpha^2 \ln\left(\frac{M_\tau}{m_\ell}\right) \cdot b_3(x^*), \tag{49}$$

where $a_{1-3}(x^*)$ and $b_{1-3}(x^*)$ are radiative form factors, which can be found in [34–36].

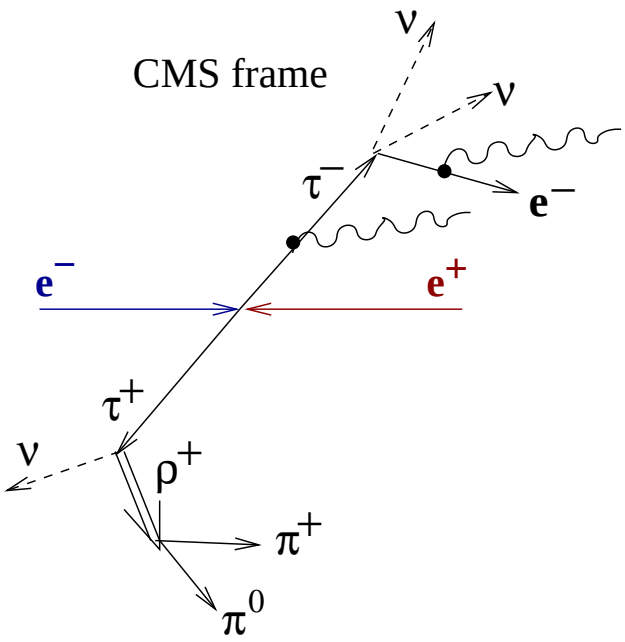

Figure 12: Radiative leptonic decay.

The internal bremsstrahlung in two-pion τ decay, i.e. $\tau^- \to \pi^-\pi^0\nu_\tau\gamma$ is shown in Fig. 14. The effect of radiative photon is described by special function $G_{EM}(m^2_{\pi\pi})$ calculated in [39, 40] and shown in Fig. 14. For the inclusive radiative decay $\tau^- \to \pi^-\pi^0\nu_\tau(\gamma)$ $(= \tau^- \to \pi^-\pi^0\nu_\tau + \tau^- \to \pi^-\pi^0\nu_\tau\gamma)$ $G_{EM}(m^2_{\pi\pi})$ factor modifies the $\pi^\pm\pi^0$ mass spectrum shape, described by W form factor (see Eq. 20) as:

$$W(m^2_{\pi\pi}) \to W(m^2_{\pi\pi}) \cdot G_{EM}(m^2_{\pi\pi}) \tag{50}$$

When all physical corrections are included the PDF for the individual event will be determined by "visible" differential cross section:

$$\mathcal{P}^{\rm vis}(\vec{z}|\vec{\Theta}) = \frac{\mathcal{F}^{\rm vis}(\vec{z}|\vec{\Theta})}{\mathcal{N}(\vec{\Theta})},\ \mathcal{F}^{\rm vis}(\vec{z}|\vec{\Theta}) = \frac{d\sigma_{\rm vis}(\ell^\mp,\rho^\pm)}{dp_\ell d\Omega_\ell dp_\rho d\Omega_\rho dm^2_{\pi\pi} d\tilde{\Omega}_\pi} = A_i^{\rm vis}(\vec{z})\Theta_i,$$

$$\mathcal{N}(\vec{\Theta}) = \int \mathcal{F}^{\rm vis}(\vec{z})d\vec{z} = C_i^{\rm vis}\Theta_i,\ C_i^{\rm vis} = \int A_i^{\rm vis}(\vec{z})d\vec{z} \tag{51}$$

Due to the finite detector resolution and piculiarities of experimental situation reconstructed parameters $\vec{z}^R$ of the particles produced in the detector

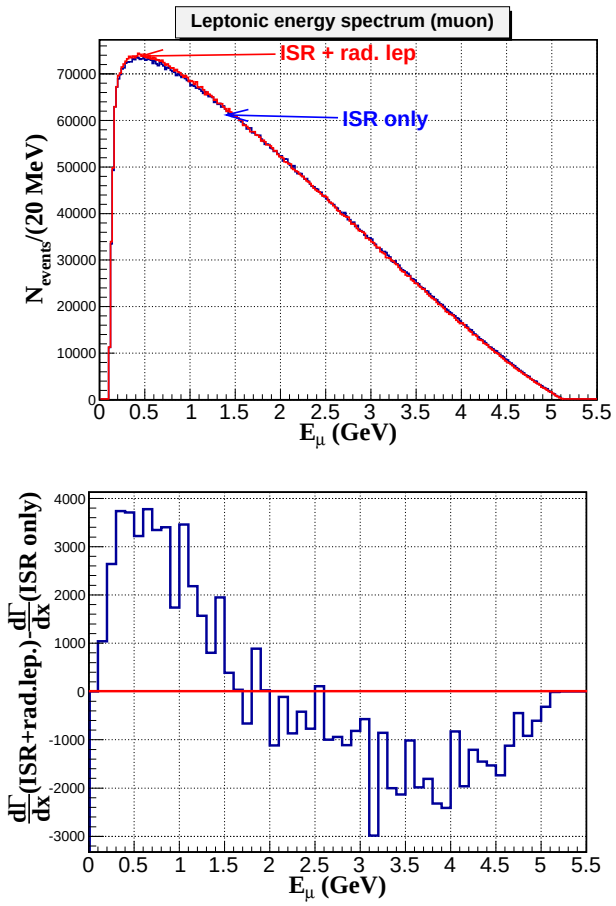

Figure 13: CMS energy spectrum of muon for MC ($\mu^{\mp}$; $\rho^{\pm}$) events (upper figure). Spectrum when only ISR effect is taken into account is shown by blue line, both effects, ISR and inner bremsstrahlung, were simulated to get spectrum shown by red line. The difference between these two spectra (lower figure). It is clearly seen that emission of additional photon results in the decrease of the muon energies.

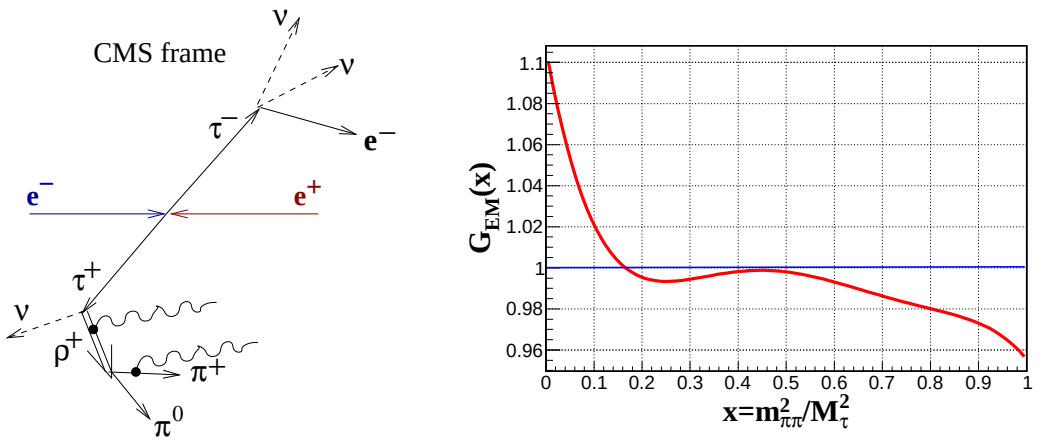

Figure 14: Effect of $\tau^- \to \pi^-\pi^0\nu_\tau\gamma$ (left). Radiative factor $G_{EM}(m^2_{\pi\pi})$ (right).

differ from their true values $\vec{z}$ ($\vec{z} = (p_\ell,\ \cos\theta_\ell,\ \phi_\ell,\ p_\rho,\ \cos\theta_\rho,\ \phi_\rho,\ m_{\pi\pi},\ \cos\tilde{\theta}_\pi,\ \tilde{\phi}_\pi)$). This distortion of parameters due to the detector effects is taken into account by resolution function $\mathcal{R}(\vec{z}^R, \vec{z})$. In the presence of the detector effects PDF($\mathcal{P}^{\rm vis}_R(\vec{z}^R|\vec{\Theta})$) can be written as:

$$\mathcal{P}^{\rm vis}_R(\vec{z}^R|\vec{\Theta}) = \frac{1}{\mathcal{N}(\vec{\Theta})}\int \mathcal{F}^{\rm vis}(\vec{z}|\vec{\Theta})\cdot\mathcal{R}(\vec{z}^R,\vec{z})d\vec{z} = \frac{1}{\mathcal{N}(\vec{\Theta})}A^{\rm vis}_{\rm Ri}(\vec{z}^R)\Theta_i,$$

$$\mathcal{N}(\vec{\Theta}) = C^{\rm vis}_{\rm Ri}\Theta_i,\ C^{\rm vis}_{\rm Ri} = \int A^{\rm vis}_{\rm Ri}(\vec{z}^R)d\vec{z}^R,$$

where $\mathcal{R}(\vec{z}^R, \vec{z})$ includes:

- track momentum resolution for $\ell^\mp(\ell = e, \mu)$ and $\pi^\pm$;
- γ energy and angular resolution for π^0;
- effect of external bremsstrahlung (in material of detector) for $e^\mp$ in $e^\mp - \rho^\pm$ events;
- beam energy spread.

Resolution function for one track is written as:

$$\mathcal{R}(\Delta p = \vec{p}^R - \vec{p}) = \frac{1}{(2\pi)^{3/2}\sqrt{\det(\hat{D})}}e^{-\frac{1}{2}\Delta p^T\hat{D}^{-1}\Delta p}, \qquad (52)$$

where $\vec{p}$ is true(generated) momentum of charged particle and $\vec{p}^R$ is its reconstructed momentum. The dependence of the $|\vec{p}^R|$ versus $|\vec{p}|$ for muons and electrons is shown in Fig. 15. Uncertainties for the track helix parameters

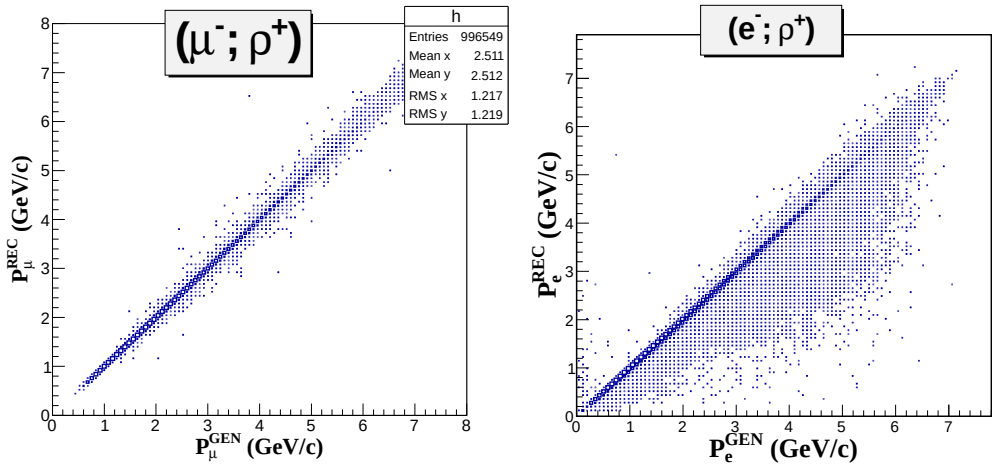

Figure 15: 2D scatter plot: $|\vec{p}^R|$ versus $|\vec{p}|$ for muons (left) and for electrons (right).

$(d_\rho,\ \phi_0,\ \kappa,\ d_z,\ \tan\lambda)$ [44] are taken from the Mdst_trk_fit panther table (array error(15)). They are propagated to the uncertainties of $\vec{p} = (p_x,\ p_y,\ p_z)$ giving the covariance matrix $\hat{D}$.

Angular $(\theta,\ \varphi)$ resolution of gammas is described by gaussian function. While energy resolution is described by asymmetric logarithmic gaussian function to fit the shape of the ECL energy response. This asymmetry is clearly seen in the dependence of reconstructed momentum of π^0, $|\vec{p}^R_{\pi^0}|$, versus generated one, $|\vec{p}_{\pi^0}|$, shown in Fig. 16.

From Fig. 15(right) strong asymmetry of the momentum response function is seen for electron, it is associated with effect of external bremsstrahlung. Bremsstrahlung photon energy(E_γ) spectrum per unit of length (for electron with energy $E_e >> \frac{m_e}{\alpha Z^{1/3}}$) is $\frac{dN_\gamma}{dxdE_\gamma} \simeq \frac{1}{X_0 E_\gamma}$. Hence the probability density function to emit bremsstrahlung photon can be written as:

$$f(\varepsilon, \theta_e) = (1-p)\delta(\varepsilon) + pH(\varepsilon - \varepsilon_{\min})\frac{1}{\varepsilon \ln\left(\frac{1}{\varepsilon_{\min}}\right)},$$

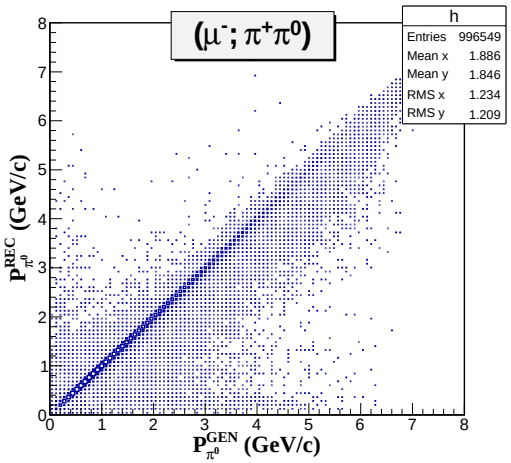

Figure 16: 2D scatter plot: $|\vec{p}^{R}|$ versus $|\vec{p}|$ for π^0 candidates.

$$p = \frac{L}{1-\varepsilon_{\min}} \ln\left(\frac{1}{\varepsilon_{\min}}\right),\ L = \frac{d_{\rm SVD} + d_{\text{vac. ch.}}}{\sin\theta_e}, \tag{53}$$

where: $\varepsilon = \frac{E_\gamma}{E_e}$, $\varepsilon_{\min} = \frac{E_{\gamma min}}{E_e} = 10^{-4}$ ($E_{\gamma\min}$ is chosen to be small enough so that $E_{\gamma\min}/E_e << \sigma_{p_e}/p_e$), $(d_{\rm SVD} + d_{\text{vac. ch.}})$ is amount of material before the drift chamber (CDC) in the units of radiation length (X_0) for the $\theta_e = 90°$. In Fig. 17 one can see the amount of material before CDC as a function of θ_e for two detector configurations, SVD-1 ($d_{\rm SVD} + d_{\text{vac. ch.}}(\text{SVD1}) = 1.9\%X_0$) and SVD-2 ($d_{\rm SVD} + d_{\text{vac. ch.}}(\text{SVD2}) = 2.7\%X_0$).

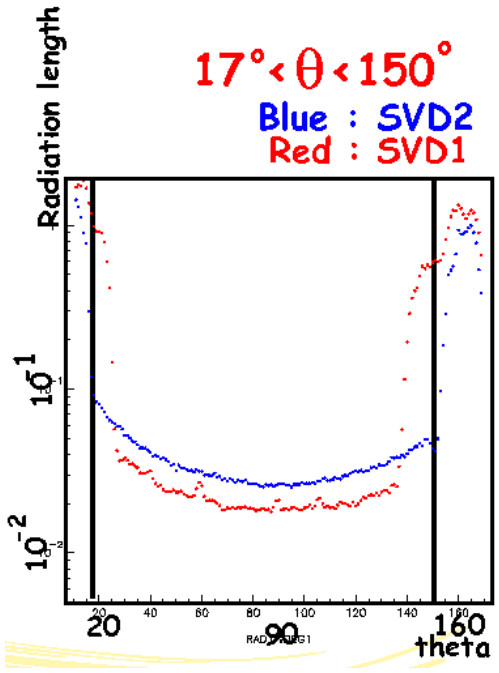

Figure 17: Amount of material before CDC in the units of X_0 as a function of θ_e from MC simulation. Data are shown for two detector configurations, SVD-1(red points) and SVD-2(blue points).

3 Selections and background

Selection of $\tau^+\tau^-$ events proceeds through three stages to suppress background while retaining high efficiency for the analysed decays. The cross sections of the main processes at the energy of the experiment (on the $\Upsilon(4S)$ resonance) are shown in Table 3.

Table 3: The main processes and their cross sections.

Process	σ, nb
$e^+e^- \to e^+e^-(\gamma)$ (radiative Bhabha) $15^o \leq \theta \leq 165^o$	123.5
$e^+e^- \to \mu^+\mu^-(\gamma)$	1.005
$e^+e^- \to q\overline{q}$ $(q = u, d, s, c)$	3.39
$e^+e^- \to b\overline{b}$	1.05
Two-photon processes $e^+e^- \to e^+e^- f\overline{f}$ $(f = u, d, s, c, e, \mu, \tau)$	72.6
$e^+e^- \to \tau^+\tau^-(\gamma)$	0.919

The first stage is preselection of $\tau^+\tau^-$ events at Belle, it is described in more detail in [45, 46]. The preselection suppresses the main background by a factor of ~ 100 retaining a 71% efficiency for $\tau^+\tau^-$ events.

At the second stage we apply additional criteria for further suppression of the background, primarily radiative Bhabha, $\mu\mu$ and two-photon events. Here we define a "**good track**" taking its parameters from the **Mdst_charged** panther table and applying cuts on a track transverse momentum $|\vec{P}|_\perp^{\rm LAB} > 0.1$ GeV/c and impact parameters: $dr < 0.5$ cm, $dz < 2.5$ cm. Then we apply the following selection criteria:

- Number of good tracks $2 \leq N_{\rm tracks} \leq 4$
- Total charge of good tracks $|Q_{\rm total}| \leq 1$
- Number of good photons with energy in CMS $N_\gamma \leq 5$ ($E_\gamma^{\rm CMS} > 0.08$ GeV)
- Total ECL energy deposition $\sum_{i=1}^{N_{\rm clusters}} E_i^{\rm LAB}({\rm ECL}) < 9$ GeV
- Missing mass 1 GeV/c$^2 \leq M_{\rm missing} \leq 7$ GeV/c^2

- Polar angle of the missing momentum $30^\circ \leq \theta^{\rm CMS}_{\rm missing} \leq 150^\circ$

In Fig. 18 one can see $M_{\rm missing}$ vs. $\theta^{\rm CMS}_{\rm missing}$ 2D-plots for experimental events, events of $\tau^+\tau^-$ MC, radiative Bhabha, $\mu^+\mu^-$ MC events and MC two-photon events. Applied cuts are also shown, we select events from the region inside a rectangular box. One can see that the cuts on $M_{\rm missing}$ and $\theta^{\rm CMS}_{\rm missing}$ provide essential background suppression.

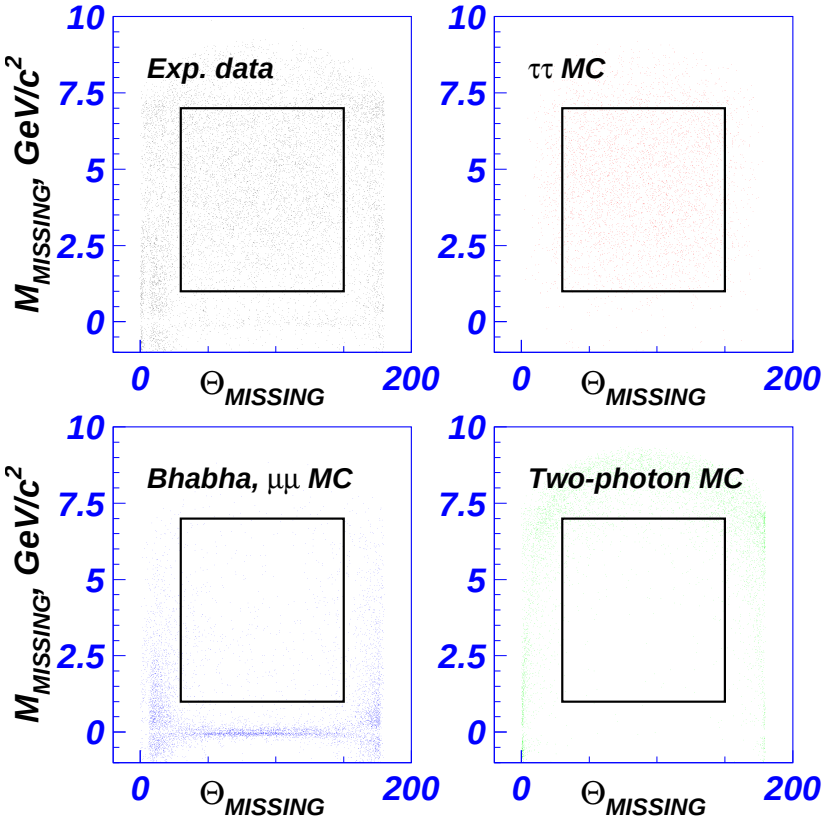

Figure 18: $M_{\rm missing}$ vs. $\theta^{\rm CMS}_{\rm missing}$ 2D-plots for experimental data, $\tau^+\tau^-$ MC, radiative Bhabha and $\mu^+\mu^-$ MC, two-photon MC events

At the third stage we select events having desired configuration $\ell^\mp - \pi^\pm\pi^0 (\ell = e, \mu)$:

- We select events with two oppositely charged tracks, one of them is identified as lepton ($eID, \mu ID > 0.9$) and the other one as pion ($PID(\pi/K) > 0.4$).

- π^0 candidate is reconstructed from the pair of gammas ($E_\gamma^{\rm LAB} > 80$ MeV) satisfying 115 MeV/$c^2 < M_{\gamma\gamma} <$ 150 MeV/c^2.
- $\cos(\vec{P}_{\rm lep}, \vec{P}_\pi) < 0$, $\cos(\vec{P}_{\rm lep}, \vec{P}_{\pi^0}) < 0$.
- 0.3 GeV/$c^2 < M_{\pi\pi^0} <$ 1.8 GeV/c^2, $P_{\pi^0}^{\rm CMS} > 0.3$ GeV/c
- To avoid an uncertainty due to the simulation of low energy fake ECL clusters we allow extra photons in an event with the total energy in the laboratory frame: $E_\gamma^{\rm LAB\ extra} < 0.1$ GeV (on the lepton side with $\cos(\vec{P}_\gamma^{\rm CMS}, \vec{P}_\rho^{\rm CMS}) < 0$) and $E_\gamma^{\rm LAB\ extra} < 0.1$ GeV (on the ρ side with $\cos(\vec{P}_\gamma^{\rm CMS}, \vec{P}_\rho^{\rm CMS}) > 0$).

The detection efficiency for signal events from MC simulation is: $\varepsilon_{\rm det}(e-\rho) = (11.53 \pm 0.01)\%$, $\varepsilon_{\rm det}(\mu - \rho) = (12.43 \pm 0.01)\%$.

After all selections it was found that the dominant background comes from the other τ decays, contribution from non-$\tau\tau$ processes is very small, $\lesssim 0.1\%$. The contents of the selected $e^\mp - \pi^\pm\pi^0$ and $\mu^\mp - \pi^\pm\pi^0$ samples were found from large sample of the generic $\tau^+\tau^-$ MC, see Table 4. It is clearly seen that for both configurations the dominant background comes from $\ell^\mp - \pi^\mp\pi^0\pi^0$ (or shortly $\ell - 3\pi$) events, for the $\mu^\mp - \pi^\pm\pi^0$ sample also notable is background from $\pi^\mp - \pi^\pm\pi^0$ (or shortly $\pi - \rho$), where pion is misidentified as muon.

Table 4: Background from the other τ decays for selected $e^\mp - \pi^\pm\pi^0$ and $\mu^\mp - \pi^\pm\pi^0$ samples.

Selected $e^\mp - \pi^\pm\pi^0$		Selected $\mu^\mp - \pi^\pm\pi^0$	
Mode	Contribution (%)	Mode	Contribution (%)
$e^\mp - \pi^\pm\pi^0$	88	$\mu^\mp - \pi^\pm\pi^0$	88
$e^\mp - \pi^\pm 2\pi^0$	10	$\mu^\mp - \pi^\pm 2\pi^0$	8.1
		$\pi^\mp - \pi^\pm\pi^0$	1.4
other	2	other	2.5

4 Method (2nd part)

General approach to take into account background in the unbinned maximum likelihood fit is to add PDF for each background component $\mathcal{P}_i^{BG}$ $(i = 1 \div N)$ according to its admixture (λ_i) explicitely:

$$\mathcal{P} = (1 - \lambda_1 - ... - \lambda_N)\mathcal{P}^{\text{Signal}} + \lambda_1 \mathcal{P}_1^{BG} + ... + \lambda_N \mathcal{P}_N^{BG} \tag{54}$$

The main background modes: $(e^{\mp};\ \pi^{\pm}2\pi^0)$, $(\mu^{\mp};\ \pi^{\pm}2\pi^0)$, $(\pi^{\mp};\ \pi^{\pm}\pi^0)$ and $(\pi^{\mp}\pi^0;\ \pi^{\pm}\pi^0)$ are included in the fit in the same way as the signal one, writing PDF explicitly, while the remaining background is taken into account using MC-based approach [15]. As a result the total PDF can be written as $(x = (p_\ell,\ \Omega_\ell,\ p_\rho,\ \Omega_\rho,\ m^2_{\pi\pi},\ \tilde{\Omega}_\pi),\ y = (p_{\pi^0},\ \Omega_{\pi^0}))$:

$$\mathcal{P}(x) = \frac{\varepsilon(x)}{\varepsilon} Z_{\text{sig}} \Bigg((1 - \lambda_{3\pi} - \lambda_\pi - \lambda_{\text{other}}) \frac{S(x)}{\int \frac{\varepsilon(x)}{\varepsilon} S(x) dx} + \lambda_{3\pi} \frac{\varepsilon}{\varepsilon_{3\pi}} \frac{Z_{3\pi}}{Z_{\text{sig}}} \frac{\tilde{B}_{3\pi}(x)}{\int \frac{\varepsilon(x)}{\varepsilon_{3\pi}} \tilde{B}_{3\pi}(x) dx} +$$

$$+ \lambda_\pi \frac{\tilde{B}_\pi(x)}{\int \frac{\varepsilon(x)}{\varepsilon} \tilde{B}_\pi(x) dx} + \lambda_\rho \frac{\tilde{B}_\rho(x)}{\int \frac{\varepsilon(x)}{\varepsilon} \tilde{B}_\rho(x) dx} + \lambda_{\text{other}} \frac{1}{Z_{\text{sig}}} \frac{B^{MC}_{\text{other}}(x)}{\int \frac{\varepsilon(x)}{\varepsilon} B^{MC}_{\text{other}}(x) dx} \Bigg), \tag{55}$$

$$\tilde{B}_{3\pi}(x) = \int 2(1 - \varepsilon_{\pi^0}(y)) \varepsilon_{\text{add}}(y) B_{3\pi}(x, y) dy, \tag{56}$$

$$\tilde{B}_\pi(x) = \frac{\varepsilon_\pi(x)}{\varepsilon(x)} B_\pi(x), \tag{57}$$

$$\tilde{B}_\rho(x) = \frac{\varepsilon_\pi(x)}{\varepsilon(x)} \int (1 - \varepsilon_{\pi^0}(y)) \varepsilon_{\text{add}}(y) B_\rho(x, y) dy, \tag{58}$$

$$\frac{\varepsilon_\pi(x)}{\varepsilon(x)} = \frac{\varepsilon^{\mu ID}_{\pi\to\mu}(p^{LAB}_\ell,\ \theta^{LAB}_\ell)}{\varepsilon^{\mu ID}_{\mu\to\mu}(p^{LAB}_\ell,\ \theta^{LAB}_\ell)} \text{ for } (\mu^{\pm};\ \rho^{\mp}) \text{ events}, \tag{59}$$

$$\frac{\varepsilon_\pi(x)}{\varepsilon(x)} = \frac{\varepsilon^{eID}_{\pi\to e}(p^{LAB}_\ell,\ \theta^{LAB}_\ell)}{\varepsilon^{eID}_{e\to e}(p^{LAB}_\ell,\ \theta^{LAB}_\ell)} \text{ for } (e^{\pm};\ \rho^{\mp}) \text{ events}, \tag{60}$$

where:

- $S(x)$ - density of the signal $(\ell^{\mp},\ \pi^{\pm}\pi^0)$ events given by Eq. 51;
- $Z_{\text{sig}} = \left[\int S(x) dx \right]^{-1}$ - signal PDF normalization factor;

- $B_{3\pi}(x,y)$ - density of background $(\ell^{\mp},\ \pi^{\pm}2\pi^0)$ events;
- $Z_{3\pi} = \left[\int B_{3\pi}(x,y)dxdy\right]^{-1}$ - $(\ell^{\mp},\ \pi^{\pm}2\pi^0)$ PDF normalization factor;
- $B_{\pi}(x)$ - density of background $(\pi^{\mp},\ \pi^{\pm}\pi^0)$ events;
- $B_{\rho}(x,y)$ - density of background $(\pi^{\mp}\pi^0,\ \pi^{\pm}\pi^0)$ events;
- $B^{MC}_{\text{other}}(x)$ - MC density of the remaining background;
- $\varepsilon(x)$ - detection efficiency in the 9D phase space;
- $\varepsilon = \frac{N^{MC}_{\text{sel}}}{N^{MC}_{\text{gen}}}$ - average detection efficiency of the signal events;
- $\varepsilon_{3\pi} = \frac{N^{MC}_{3\pi\text{sel}}}{N^{MC}_{3\pi\text{gen}}}$ - average detection efficiency of the $\ell - 3\pi$ events;
- $\varepsilon_{\pi^0}(y)$ - π^0 detection efficiency;
- $\varepsilon_{\text{add}}(y) = \varepsilon^{3\pi}_{\text{add}}(y)/\varepsilon^{\text{sig}}_{\text{add}}$ - ratio of efficiencies ($\varepsilon^{\text{sig}}_{\text{add}}(\varepsilon^{3\pi}_{\text{add}}(y))$ is efficiency of the $E^{LAB}_{\gamma rest}$ cut for the signal $(\ell - 3\pi)$ events);
- $\varepsilon_{\pi}(x)$ - detection efficiency for $(\pi^{\mp},\ \pi^{\pm}\pi^0)$ events;
- $\varepsilon^{\mu ID}_{\pi\to\mu}(p^{LAB}_{\ell},\ \theta^{LAB}_{\ell})$ - $\pi \to \mu$ misidentification efficiency;
- $\varepsilon^{\mu ID}_{\mu\to\mu}(p^{LAB}_{\ell},\ \theta^{LAB}_{\ell})$ - muon identification efficiency.
- $\varepsilon^{eID}_{\pi\to e}(p^{LAB}_{\ell},\ \theta^{LAB}_{\ell})$ - $\pi \to e$ misidentification efficiency;
- $\varepsilon^{eID}_{e\to e}(p^{LAB}_{\ell},\ \theta^{LAB}_{\ell})$ - electron identification efficiency.

Efficiency ratio in Eq. 59(60) was tabulated from MC as a function of $p^{\text{LAB}}_{\mu}(p^{\text{LAB}}_{e})$ and $\theta^{\text{LAB}}_{\mu}(\theta^{\text{LAB}}_{e})$ and used to evaluate $\tilde{B}_{\pi}(x)$ for each event. For the clarity, Eq. 55 can be rewritten in more detail (for the k-th event):

$$S^{(k)} = A^{(k)}_0 + A^{(k)}_1\rho + A^{(k)}_2\eta + A^{(k)}_3\xi_\rho\xi + A^{(k)}_4\xi_\rho\xi\delta \tag{61}$$

$$\tilde{B}^{(k)}_{3\pi} = \tilde{B}^{(k)}_{3\pi,0} + \tilde{B}^{(k)}_{3\pi,1}\rho + \tilde{B}^{(k)}_{3\pi,2}\eta + \tilde{B}^{(k)}_{3\pi,3}\xi_\rho\xi + \tilde{B}^{(k)}_{3\pi,4}\xi_\rho\xi\delta \tag{62}$$

$$\mathcal{P}^{(k)} = \frac{\varepsilon(x^{(k)})}{\varepsilon} Z_{\text{sig}} \Bigg((1-\lambda_{3\pi}-\lambda_{\pi}-\lambda_{\text{other}}) \frac{A^{(k)}_0 + A^{(k)}_1\rho + A^{(k)}_2\eta + A^{(k)}_3\xi_\rho\xi + A^{(k)}_4\xi_\rho\xi\delta}{\frac{1}{N^{MC}_{\text{sel}}} \sum_{i=1}^{N^{MC}_{\text{sel}}} \frac{A^{(i)}_0 + A^{(i)}_1\rho + A^{(i)}_2\eta + A^{(i)}_3\xi_\rho\xi + A^{(i)}_4\xi_\rho\xi\delta}{A^{(i)}_0 + A^{(i)}_1 0.75 + A^{(i)}_2 0.0 + A^{(i)}_3 1.0 + A^{(i)}_4 0.75}} +$$

$$+\lambda_{3\pi}\frac{Z_{3\pi}}{Z_{\rm sig}}\left(\frac{\varepsilon}{\varepsilon_{3\pi}}\right)\frac{\tilde{B}^{(k)}_{3\pi,0}+\tilde{B}^{(k)}_{3\pi,1}\rho+\tilde{B}^{(k)}_{3\pi,2}\eta+\tilde{B}^{(k)}_{3\pi,3}\xi_\rho\xi+\tilde{B}^{(k)}_{3\pi,4}\xi_\rho\xi\delta}{\frac{1}{N^{MC}_{3\pi,\rm sel}}\sum\limits_{i=1}^{N^{MC}_{3\pi,\rm sel}}\frac{\tilde{B}^{(i)}_{3\pi,0}+\tilde{B}^{(i)}_{3\pi,1}\rho+\tilde{B}^{(i)}_{3\pi,2}\eta+\tilde{B}^{(i)}_{3\pi,3}\xi_\rho\xi+\tilde{B}^{(i)}_{3\pi,4}\xi_\rho\xi\delta}{\tilde{B}^{(i)}_{3\pi,0}+\tilde{B}^{(i)}_{3\pi,1}0.75+\tilde{B}^{(i)}_{3\pi,2}0.0+\tilde{B}^{(i)}_{3\pi,3}1.0+\tilde{B}^{(i)}_{3\pi,4}0.75}}+$$

$$+\lambda_{\pi}\frac{\tilde{B}^{(k)}_{\pi}}{\frac{1}{N^{MC}_{\rm sel}}\sum\limits_{i=1}^{N^{MC}_{\rm sel}}\frac{\tilde{B}^{(i)}_{\pi}}{A^{(i)}_0+A^{(i)}_1 0.75+A^{(i)}_2 0.0+A^{(i)}_3 1.0+A^{(i)}_4 0.75}}+$$

$$+\lambda_{\rho}\frac{\tilde{B}^{(k)}_{\rho}}{\frac{1}{N^{MC}_{\rm sel}}\sum\limits_{i=1}^{N^{MC}_{\rm sel}}\frac{\tilde{B}^{(i)}_{\rho}}{A^{(i)}_0+A^{(i)}_1 0.75+A^{(i)}_2 0.0+A^{(i)}_3 1.0+A^{(i)}_4 0.75}}+$$

$$+\lambda_{\rm other}\frac{1}{Z_{\rm sig}}\frac{B^{MC}_{\rm other}(x)}{\int\frac{\varepsilon(x)}{\varepsilon}B^{MC}_{\rm other}(x)dx}\Bigg), \tag{63}$$

$$Z_{\rm sig}=\frac{1}{V_{9D}N^{\rm sig}_{\rm gen}}\sum_{i=1}^{N^{\rm sig}_{\rm gen}}\frac{1}{A^{(i)}_0+A^{(i)}_1 0.75+A^{(i)}_2 0.0+A^{(i)}_3 1.0+A^{(i)}_4 0.75}, \tag{64}$$

$$Z_{3\pi}=\frac{1}{V_{12D}N^{3\pi}_{\rm gen}}\sum_{i=1}^{N^{3\pi}_{\rm gen}}\frac{1}{B^{(i)}_{3\pi,0}+B^{(i)}_{3\pi,1}0.75+B^{(i)}_{3\pi,2}0.0+B^{(i)}_{3\pi,3}1.0+B^{(i)}_{3\pi,4}0.75}, \tag{65}$$

where $N^{\rm sig}_{\rm gen}(N^{3\pi}_{\rm gen})$ is number of the generated signal($\ell-3\pi$) MC events, $N^{MC}_{\rm sel}(N^{MC}_{3\pi,\rm sel})$ is number of the selected signal($\ell-3\pi$) MC events, $V_{9D}(V_{12D})$ is volume of the 9D(12D) phase space of the signal($\ell-3\pi$) events. In Eq. 63 the dominant background contributions, calculated analytically, are written explicitely through their PDF coefficients: A_i, $\tilde{B}_{3\pi,i}(i=0\div4)$, $\tilde{B}_\pi$, $\tilde{B}_\rho$. For the better perception of the formula, Michel parameters (and their SM values) are shown in blue color, normalization factors, $Z_{\rm sig}$ and $Z_{3\pi}$, are shown in green, their values are collected in Table 5.

Table 5: $Z_{\rm sig}$ and $Z_{3\pi}$ normalization factors for $\ell^{\pm}$-h$^{\mp}$ events ($\ell=e,\ \mu$, h$^{\mp}=\pi^{\mp}\pi^0,\ \pi^{\mp}\pi^0\pi^0$).

Factor	$e^{\pm}$-h$^{\mp}$	$\mu^{\pm}$-h$^{\mp}$
$Z_{\rm sig}$	3963	3812
$Z_{3\pi}$	381.7	366.4

4.1 Description of $(\ell^{\mp},\ \pi^{\pm}2\pi^0)$ background

To get the density of $(\ell^{\mp},\ \pi^{\pm}2\pi^0)$ events, $B_{3\pi}(x,y)$, we follow the same procedure, which was used for the signal events (see Eq. 28, 29, 30). To write the total differential cross section for $(\ell^{\mp},\ \pi^{\pm}2\pi^0)$ events we combine differential cross section of the $e^+e^- \to \tau^-(\vec{\zeta}^{*-})\tau^+(\vec{\zeta}^{*+})$ reaction given by Eq. 18, differential decay width of $\tau^{\mp}(\vec{\zeta}^{*}) \to \ell^{\mp}\nu\nu$ given by Eq. 28, and differential decay width of $\tau^{\pm}(P,\vec{\zeta}^{*\prime}) \to \pi^{\pm}(k_1)\pi^0(k_2)\pi^0(k_3)\nu(q)$:

$$\frac{d\Gamma(\tau^{\mp} \to \pi^{\mp}2\pi^0\nu)}{d\Omega^*_{3\pi}dm^2_{3\pi}d\hat{\Omega}_{\rho}dm^2_{\pi\pi}d\tilde{\Omega}_{\pi}} = \kappa_{3\pi}(A' \pm \vec{B}'\vec{\zeta}'^{*})W(m^2_{\pi\pi},m^2_{3\pi}), \tag{66}$$

$$W = \frac{\tilde{p}_{\pi}(m^2_{\pi\pi})}{m_{\pi\pi}}\frac{\hat{p}_{\rho}(m^2_{\pi\pi},m^2_{3\pi})}{m_{3\pi}}\frac{p^*_{3\pi}(m^2_{3\pi},M_{\tau})}{M_{\tau}},$$

$$\tilde{p}_{\pi}(m^2_{\pi\pi}) = \frac{\sqrt{(m^2_{\pi\pi}-(m_{\pi}+m_{\pi^0})^2)(m^2_{\pi\pi}-(m_{\pi}-m_{\pi^0})^2)}}{2m_{\pi\pi}},$$

$$\hat{p}_{\rho}(m^2_{\pi\pi},m^2_{3\pi}) = \frac{\sqrt{(m^2_{3\pi}-(m_{\pi\pi}+m_{\pi^0})^2)(m^2_{3\pi}-(m_{\pi\pi}-m_{\pi^0})^2)}}{2m_{3\pi}},$$

$$p^*_{3\pi}(m^2_{3\pi},M_{\tau}) = \frac{M_{\tau}}{2}\left(1-\frac{m^2_{3\pi}}{M^2_{\tau}}\right),$$

$$A' = H_1 + \xi_{a_1}H_2,\ \vec{B}' = \xi_{a_1}\vec{G}_1 + \vec{G}_2,\ \xi_{a_1} = 1$$

$$H_1 = (P,J^*)(q,J) + (P,J)(q,J^*) - (J,J^*)(P,q),$$

$$H_2 = ie^{\mu\nu\sigma\delta}J_{\mu}J^*_{\nu}P_{\sigma}q_{\delta},$$

$$G^{\lambda}_1 = M_{\tau}((q,J)J^{*\lambda} + (q,J^*)J^{\lambda} - (J,J^*)q^{\lambda}),$$

$$G^{\lambda}_2 = iM_{\tau}e^{\lambda\mu\nu\sigma}J_{\mu}J^*_{\nu}q_{\sigma},\ q = P-k,$$

where the $\pi^{\pm}\pi^0\pi^0$ hadronic current, J^{μ}, is written according to the CLEO model [47] with the dominant $\tau^- \to a^-_1(1260)\nu_{\tau}$ mechanism (see also Fig. 19, 20):

$$J^{\mu} = \beta_1 j^{\mu}_1(\rho\pi^0)_{\mathrm{S-wave}} + \beta_2 j^{\mu}_2(\rho'\pi^0)_{\mathrm{S-wave}} + \beta_3 j^{\mu}_3(\rho\pi^0)_{\mathrm{D-wave}} + \beta_4 j^{\mu}_4(\rho'\pi^0)_{\mathrm{D-wave}} +$$

$$+\beta_5 j^{\mu}_5(f_2(1270)\pi)_{\mathrm{P-wave}} + \beta_6 j^{\mu}_6(f_0(500)\pi)_{\mathrm{P-wave}} + \beta_7 j^{\mu}_7(f_0(1370)\pi)_{\mathrm{P-wave}} \tag{67}$$

$$\frac{d\sigma(\ell^{\mp},\pi^{\pm}2\pi^0)}{dE^*_{\ell}d\Omega^*_{\ell}d\Omega^*_{3\pi}dm^2_{3\pi}d\hat{\Omega}_{\rho}dm^2_{\pi\pi}d\tilde{\Omega}_{\pi}d\Omega_{\tau}} =$$

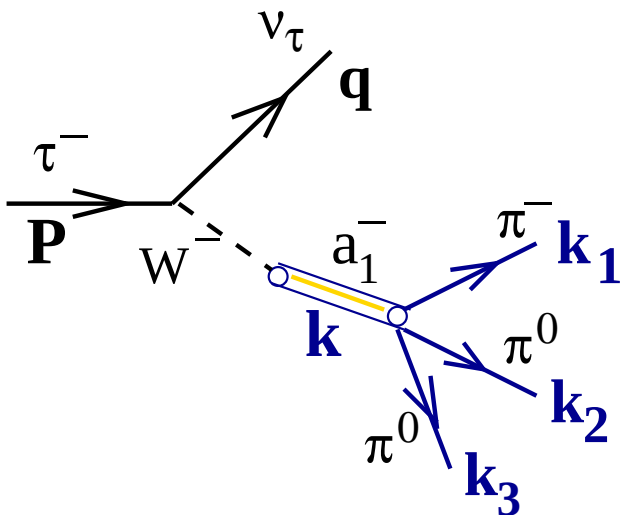

Figure 19: The $\tau^- \to \pi^-\pi^0\pi^0\nu_\tau$ decay is dominated by $\tau^- \to a_1^-(1260)\nu_\tau$ mechanism, where $a_1^- \to (\rho^-\pi^0)_{S-wave} \to \pi^-\pi^0\pi^0$.

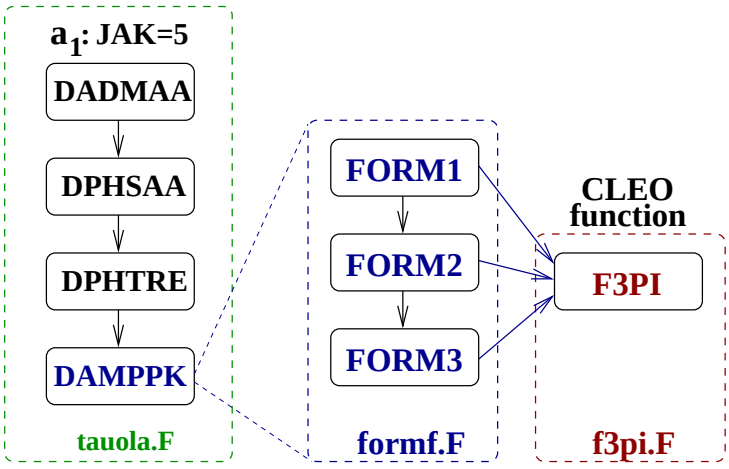

Figure 20: Flowchart of the part of TAUOLA generator to generate $\tau^- \to \pi^-\pi^0\pi^0\nu_\tau$ decay.

$$= \kappa_\ell \kappa_{3\pi} \frac{\alpha^2 \beta_\tau}{64 E_\tau^2} \big(D_0 A A' + B D_{ij} n^*_{\ell i} B'_j \big) W(m^2_{\pi\pi}, m^2_{3\pi}), \tag{68}$$

$$\frac{d\sigma(\ell^\mp, \pi^\pm 2\pi^0)}{dp_\ell d\Omega_\ell dp_\rho d\Omega_\rho dm^2_{\pi\pi} d\tilde{\Omega}_\pi dp_{\pi^0} d\Omega_{\pi^0}} = \int\limits_{\Phi_1}^{\Phi_2} \frac{d\sigma(\ell^\mp, \pi^\pm 2\pi^0)}{dE^*_\ell d\Omega^*_\ell d\Omega^*_{3\pi} dm^2_{3\pi} d\hat{\Omega}_\rho dm^2_{\pi\pi} d\tilde{\Omega}_\pi d\Omega_\tau} \times$$

$$\times \left| \frac{\partial(E^*_\ell, \Omega^*_\ell)}{\partial(p_\ell, \Omega_\ell)} \right| \cdot \left| \frac{\partial(\Omega^*_{3\pi}, \Omega_\tau)}{\partial(p_{3\pi}, \Omega_{3\pi}, \Phi_\tau)} \right| \cdot \left| \frac{\partial(m^2_{3\pi}, \hat{\Omega}_\rho, p_{3\pi}, \Omega_{3\pi})}{\partial(p_\rho, \Omega_\rho, p_{\pi^0}, \Omega_{\pi^0})} \right| d\Phi_\tau, \tag{69}$$

$$\left| \frac{\partial(\Omega^*_{3\pi}, \Omega_\tau)}{\partial(p_{3\pi}, \Omega_{3\pi}, \Phi_\tau)} \right| = \frac{M_\tau}{|\vec{p}_\tau|} \frac{p_{3\pi}}{E_{3\pi} p^*_{3\pi}}, \tag{70}$$

$$\left| \frac{\partial(m^2_{3\pi}, \hat{\Omega}_\rho, p_{3\pi}, \Omega_{3\pi})}{\partial(p_\rho, \Omega_\rho, p_{\pi^0}, \Omega_{\pi^0})} \right| = \frac{2 m_{3\pi}}{\hat{p}_\rho} \left(\frac{p_\rho p_{\pi^0}}{p_{3\pi}} \right)^2 \left(\frac{E_{3\pi}}{E_\rho E_{\pi^0}} \right), \tag{71}$$

where the parameters marked by hat are evaluated in the 3π rest frame. Radiative corrections, to get visible differential cross section of $\ell - 3\pi$ events, $\frac{d\sigma_{\rm vis}(\ell^\mp, \pi^\pm 2\pi^0)}{dp_\ell d\Omega_\ell dp_\rho d\Omega_\rho dm^2_{\pi\pi} d\tilde{\Omega}_\pi dp_{\pi^0} d\Omega_{\pi^0}}$, were taken into account using the same approach as for the signal events, see Eq. 43, 44, 46. As a result:

$$B_{3\pi}(x, y) = \frac{d\sigma_{\rm vis}(\ell^\mp, \pi^\pm 2\pi^0)}{dp_\ell d\Omega_\ell dp_\rho d\Omega_\rho dm^2_{\pi\pi} d\tilde{\Omega}_\pi dp_{\pi^0} d\Omega_{\pi^0}} \tag{72}$$

The inefficiency, $(1 - \varepsilon_{\pi^0}(y))\varepsilon_{\rm add}(y)$, in Eq. 56 was tabulated in 28 bins in π^0 momentum, $P^{\rm CMS}_{\pi^0}$, and in 20 bins in $\cos\theta^{\rm CMS}_{\pi^0}$ using large $\ell - 3\pi$ MC sample. Figure 21 shows the inefficiency as a function of the π^0 momentum, $P^{\rm CMS}_{\pi^0}$, in bins of the cosine of the π^0 polar angle, $\cos\theta^{\rm CMS}_{\pi^0}$, in CMS, while Fig. 22 shows the inefficiency in each of the 28 bins of the π^0 momentum.

4.2 Description of $(\pi^\mp,\ \pi^\pm\pi^0)$ background

In the $(\pi^\mp,\ \pi^\pm\pi^0)$ events the direction of τ axis in CMS is determined up to the two-fold ambiguity, described by Φ_1 and Φ_2 azimuthal angles, see Eq. 26 and Fig. 23. The total differential cross section for $(\pi^\mp,\ \pi^\pm\pi^0)$ events ($B_\pi(x)$ density) is written in the standard way combining differential cross section of reaction $e^+e^- \to \tau^-\tau^+$ given by Eq. 18, differential decay width of $\tau^\pm(\vec{\zeta}^{*\prime}) \to \rho^\pm\nu$ given by Eq. 20, and differential decay width of $\tau^\mp(\vec{\zeta}^*) \to \pi^\mp\nu$:

$$\frac{d\Gamma(\tau^\mp(\vec{\zeta}^*) \to \pi^\mp\nu)}{d\Omega^*_\pi} = \kappa_\pi (1 \pm \xi_\pi \vec{n}^*_\pi \vec{\zeta}^*), \tag{73}$$

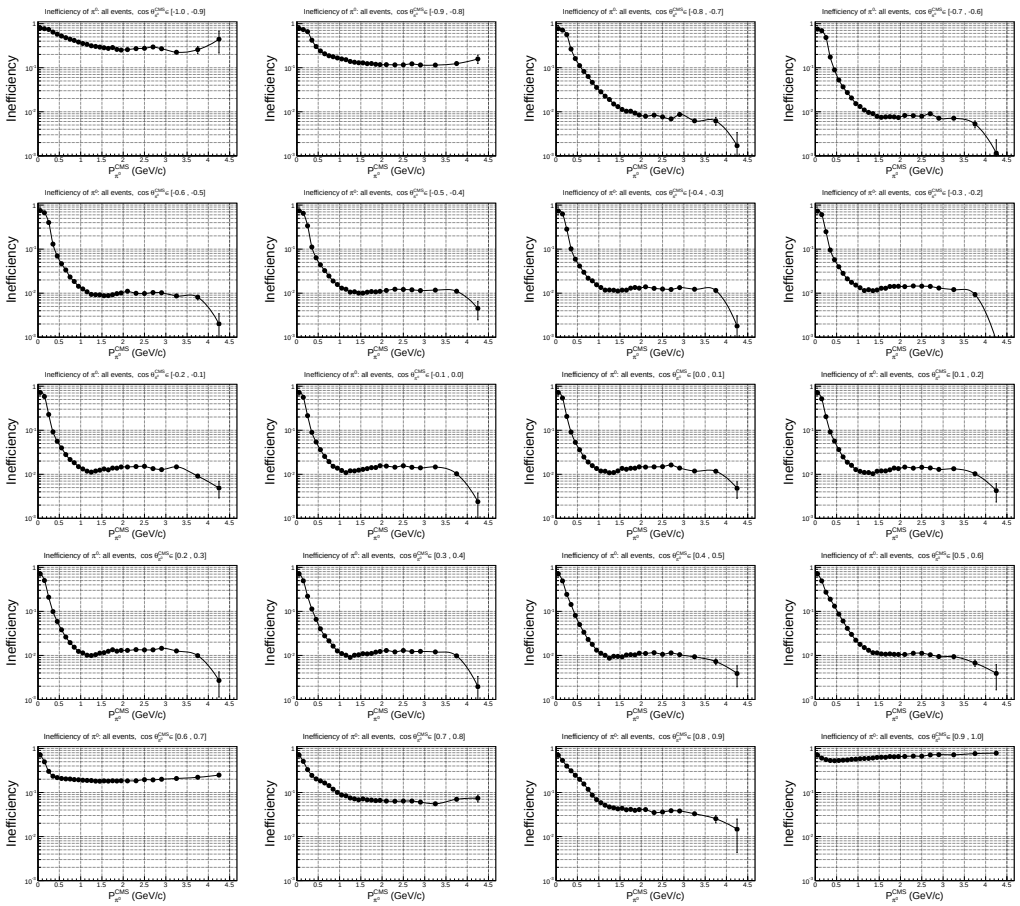

Figure 21: The inefficiency, $(1 - \varepsilon_{\pi^0}(y))\varepsilon_{\text{add}}(y)$, as a function of the π^0 momentum ($P_{\pi^0}^{\text{CMS}}$) in each of the 20 bins of the cosine of the π^0 polar angle ($\cos\theta_{\pi^0}^{\text{CMS}}$) in CMS.

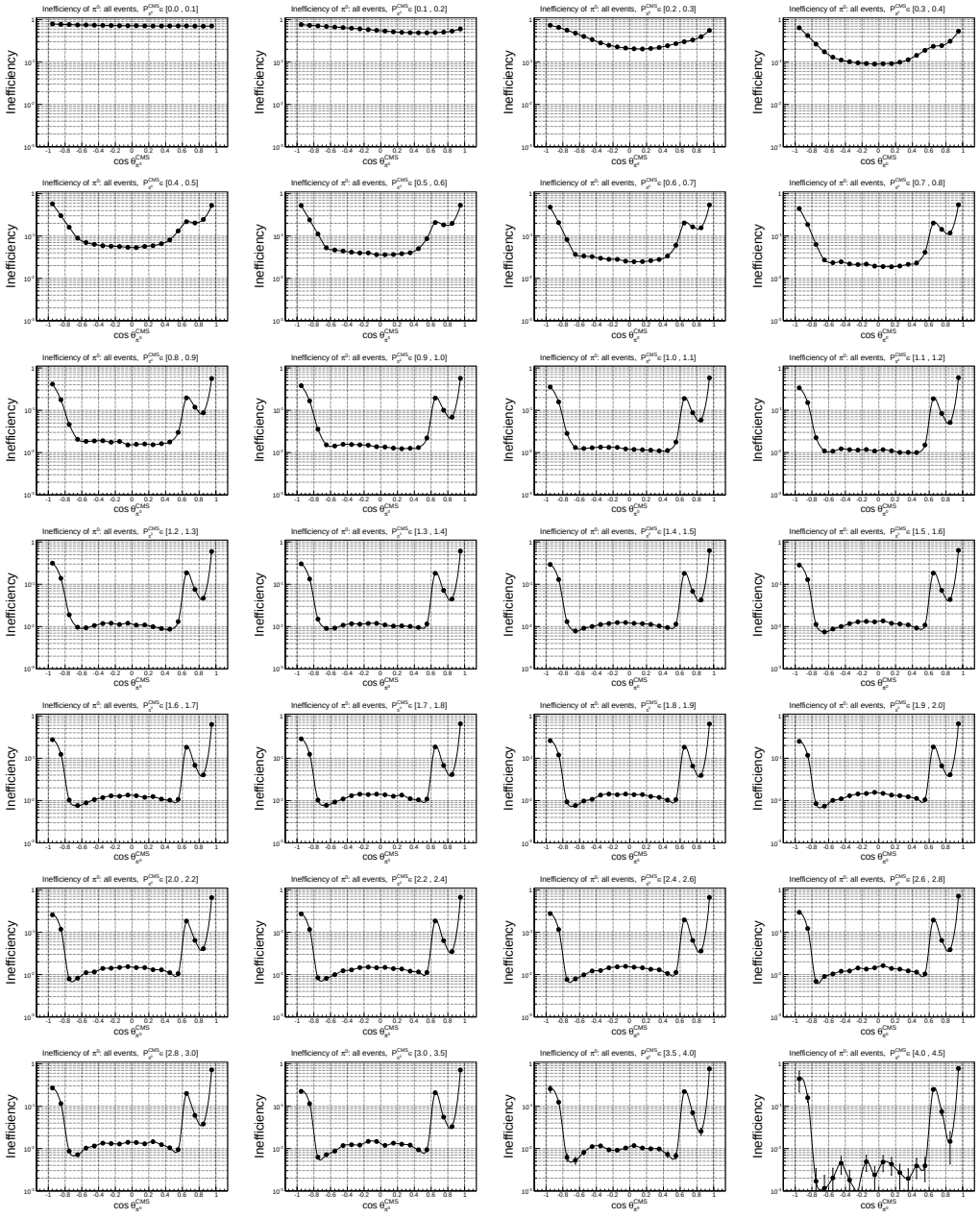

Figure 22: The inefficiency, $(1 - \varepsilon_{\pi^0}(y))\varepsilon_{\text{add}}(y)$, as a function of the cosine of the π^0 polar angle ($\cos\theta^{\text{CMS}}_{\pi^0}$) in each of the 28 bins of the π^0 momentum ($P^{\text{CMS}}_{\pi^0}$) in CMS.

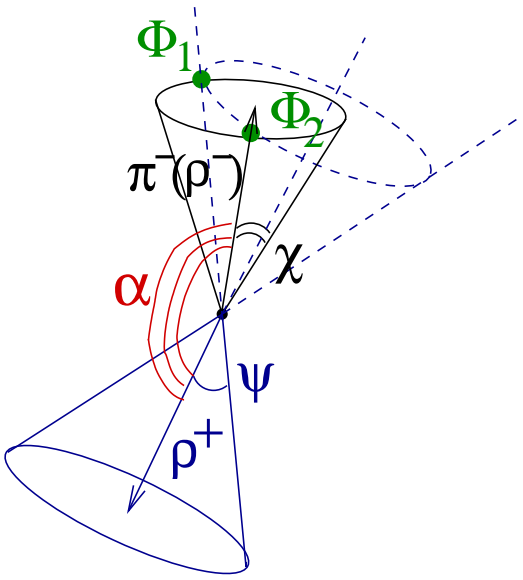

Figure 23: Two allowed τ axis directions for $(\pi^{\mp},\ \pi^{\pm}\pi^0)/(\pi^{\mp}\pi^0,\ \pi^{\pm}\pi^0)$ events.

$$\frac{d\sigma(\pi^{\mp},\rho^{\pm})}{d\Omega_{\pi}^{*}d\Omega_{\rho}^{*}dm_{\pi\pi}^{2}d\tilde{\Omega}_{\pi}d\Omega_{\tau}}=\kappa_{\pi}\kappa_{\rho}\frac{\alpha^{2}\beta_{\tau}}{64E_{\tau}^{2}}\left(D_{0}A'-\xi_{\rho}\xi_{\pi}D_{ij}n_{\pi i}^{*}B_{j}'\right),\ \xi_{\rho}\xi_{\pi}=1, \quad (74)$$

$$\frac{d\sigma(\pi^{\mp},\rho^{\pm})}{dp_{\pi}d\Omega_{\pi}dp_{\rho}d\Omega_{\rho}dm_{\pi\pi}^{2}d\tilde{\Omega}_{\pi}}=\sum_{\Phi_1,\Phi_2}\frac{d\sigma(\pi^{\mp},\rho^{\pm})}{d\Omega_{\pi}^{*}d\Omega_{\rho}^{*}dm_{\pi\pi}^{2}d\tilde{\Omega}_{\pi}d\Omega_{\tau}}\left|\frac{\partial(\Omega_{\pi}^{*},\Omega_{\rho}^{*},\Omega_{\tau})}{\partial(p_{\pi},\Omega_{\pi},p_{\rho},\Omega_{\rho})}\right| \quad (75)$$

$$\left|\frac{\partial(\Omega_{\pi}^{*},\Omega_{\rho}^{*},\Omega_{\tau})}{\partial(p_{\pi},\Omega_{\pi},p_{\rho},\Omega_{\rho})}\right|=\frac{\beta_{\pi}\beta_{\rho}}{\gamma_{\tau}^{2}\beta_{\tau}^{2}p_{\pi}^{*}p_{\rho}^{*}|\vec{n}_{\tau}\cdot(\vec{n}_{\rho}\times\vec{n}_{\pi})|},\ \vec{n}_{\pi}=\frac{\vec{p}_{\pi}}{p_{\pi}},\ \vec{n}_{\rho}=\frac{\vec{p}_{\rho}}{p_{\rho}},\ \vec{n}_{\tau}=\frac{\vec{p}_{\tau}}{p_{\tau}}, \quad (76)$$

$$\beta_{\pi}=\frac{p_{\pi}}{E_{\pi}},\ \beta_{\rho}=\frac{p_{\rho}}{E_{\rho}},\ p_{\pi}^{*}=\frac{M_{\tau}}{2}\left(1-\frac{m_{\pi}^{2}}{M_{\tau}^{2}}\right),\ p_{\rho}^{*}=\frac{M_{\tau}}{2}\left(1-\frac{m_{\pi\pi}^{2}}{M_{\tau}^{2}}\right), \quad (77)$$

Radiative corrections, to get visible differential cross section of $\pi-\rho$ events, $\frac{d\sigma_{\rm vis}(\pi^{\mp},\rho^{\pm})}{dp_{\pi}d\Omega_{\pi}dp_{\rho}d\Omega_{\rho}dm_{\pi\pi}^{2}d\tilde{\Omega}_{\pi}}$, were taken into account using the same approach as for the signal events, see Eq. 43, 44, 46. As a result:

$$B_{\pi}(x)=\frac{d\sigma_{\rm vis}(\pi^{\mp},\rho^{\pm})}{dp_{\pi}d\Omega_{\pi}dp_{\rho}d\Omega_{\rho}dm_{\pi\pi}^{2}d\tilde{\Omega}_{\pi}}. \quad (78)$$

4.3 Description of $(\pi^{\mp}\pi^0,\ \pi^{\pm}\pi^0)$ background

In the $(\pi^{\mp}\pi^0,\ \pi^{\pm}\pi^0)$ events the direction of τ axis in CMS is determined up to the two-fold ambiguity, described by Φ_1 and Φ_2 azimuthal angles, see

also Eq. 26 and Fig. 23. The total differential cross section for $(\pi^{\mp}\pi^0,\ \pi^{\pm}\pi^0)$ events is written in the standard way combining differential cross section of reaction $e^+e^- \to \tau^-\tau^+$ given by Eq. 18 and differential decay width of $\tau^{\pm}(\vec{\zeta}^{*\prime}) \to \rho^{\pm}\nu$ given by Eq. 20 $(\tau^-(A,\ \vec{B});\ \tau^+(A',\ \vec{B}'))$:

$$\frac{d\sigma(\rho^-,\rho^+)}{d\Omega^*_\rho dm^2_{\pi\pi} d\tilde{\Omega}_\pi d\Omega'^*_\rho dm'^2_{\pi\pi} d\tilde{\Omega}'_\pi d\Omega_\tau} = \kappa_\rho\kappa'_\rho \frac{\alpha^2\beta_\tau}{64E^2_\tau}\big(D_0AA' - \xi^2_\rho D_{ij}B_iB'_j\big),\ \xi^2_\rho = 1, \quad (79)$$

$$\frac{d\sigma(\rho^-,\rho^+)}{dp_\rho d\Omega_\rho dm^2_{\pi\pi} d\tilde{\Omega}_\pi dp'_\rho d\Omega'_\rho dm'^2_{\pi\pi} d\tilde{\Omega}'_\pi} = \sum_{\Phi_1,\Phi_2} \frac{d\sigma(\rho^-,\rho^+)}{d\Omega^*_\rho dm^2_{\pi\pi} d\tilde{\Omega}_\pi d\Omega'^*_\rho dm'^2_{\pi\pi} d\tilde{\Omega}'_\pi d\Omega_\tau} \left|\frac{\partial(\Omega^*_\rho,\Omega'^*_\rho,\Omega_\tau)}{\partial(p_\rho,\Omega_\rho,p'_\rho,\Omega'_\rho)}\right| \quad (80)$$

$$\frac{d\sigma(\rho^-,\rho^+)}{dp_\pi d\Omega_\pi dp_{\pi^0} d\Omega_{\pi^0} dp'_\rho d\Omega'_\rho dm'^2_{\pi\pi} d\tilde{\Omega}'_\pi} = \sum_{\Phi_1,\Phi_2} \frac{d\sigma(\rho^-,\rho^+)}{dp_\rho d\Omega_\rho dm^2_{\pi\pi} d\tilde{\Omega}_\pi dp'_\rho d\Omega'_\rho dm'^2_{\pi\pi} d\tilde{\Omega}'_\pi} \left|\frac{\partial(m^2_{\pi\pi},\tilde{\Omega}_\pi,p_\rho,\Omega_\rho)}{\partial(p_\pi,\Omega_\pi,p_{\pi^0},\Omega_{\pi^0})}\right| \quad (81)$$

$$\left|\frac{\partial(\Omega^*_\rho,\Omega'^*_\rho,\Omega_\tau)}{\partial(p_\rho,\Omega_\rho,p'_\rho,\Omega'_\rho)}\right| = \frac{\beta_\rho\beta'_\rho}{\gamma^2_\tau\beta^2_\tau p^*_\rho p'^*_\rho |\vec{n}_\tau\cdot(\vec{n}'_\rho\times\vec{n}_\rho)|},\ \vec{n}_\rho = \frac{\vec{p}_\rho}{p_\rho},\ \vec{n}'_\rho = \frac{\vec{p}'_\rho}{p'_\rho},\ \vec{n}_\tau = \frac{\vec{p}_\tau}{p_\tau}, \quad (82)$$

$$\beta_\rho = \frac{p_\rho}{E_\rho},\ \beta'_\rho = \frac{p'_\rho}{E'_\rho},\ p^*_\rho = \frac{M_\tau}{2}\left(1-\frac{m^2_{\pi\pi}}{M^2_\tau}\right),\ p'^*_\rho = \frac{M_\tau}{2}\left(1-\frac{m'^2_{\pi\pi}}{M^2_\tau}\right), \quad (83)$$

$$\left|\frac{\partial(m^2_{\pi\pi},\tilde{\Omega}_\pi,p_\rho,\Omega_\rho)}{\partial(p_\pi,\Omega_\pi,p_{\pi^0},\Omega_{\pi^0})}\right| = \frac{2m_{\pi\pi}}{\tilde{p}_\pi}\left(\frac{p_\pi p_{\pi^0}}{p_\rho}\right)^2\left(\frac{E_\rho}{E_\pi E_{\pi^0}}\right)^2, \quad (84)$$

$$\tilde{p}_\pi = \frac{\sqrt{[m^2_{\pi\pi}-(m_\pi+m_{\pi^0})^2][m^2_{\pi\pi}-(m_\pi-m_{\pi^0})^2]}}{2m_{\pi\pi}}. \quad (85)$$

Radiative corrections, to get visible differential cross section of $\rho-\rho$ events, $\frac{d\sigma_{\rm vis}(\rho^-,\rho^+)}{dp_\pi d\Omega_\pi dp_{\pi^0} d\Omega_{\pi^0} dp'_\rho d\Omega'_\rho dm'^2_{\pi\pi} d\tilde{\Omega}'_\pi}$ were taken into account using the same approach as for the signal events, see Eq. 43, 44, 46. As a result:

$$B_\rho(x,y) = \frac{d\sigma_{\rm vis}(\rho^-,\rho^+)}{dp_\pi d\Omega_\pi dp_{\pi^0} d\Omega_{\pi^0} dp'_\rho d\Omega'_\rho dm'^2_{\pi\pi} d\tilde{\Omega}'_\pi} \quad (86)$$

4.4 Description of the remaining background

To get PDF for the remaining background we use MC based method described in [15] (see also Fig. 24). In this method large MC sample of events of the remaining background is used. Each event is represented by a point in 9D parameter space $x = (p_\ell,\ \cos\theta_\ell,\ \varphi_\ell;\ p_\rho,\ \cos\theta_\rho,\ \varphi_\rho;\ m^2_{\pi\pi},\ \cos\tilde{\theta}_\pi,\ \tilde{\varphi_\pi})$. Around each i-th experimental event we choose 9D volume V_i, which is large enough to calculate likelihood function precisely, but at the same time limited to keep the nonlinearity of the PDF to be small. After that we count the

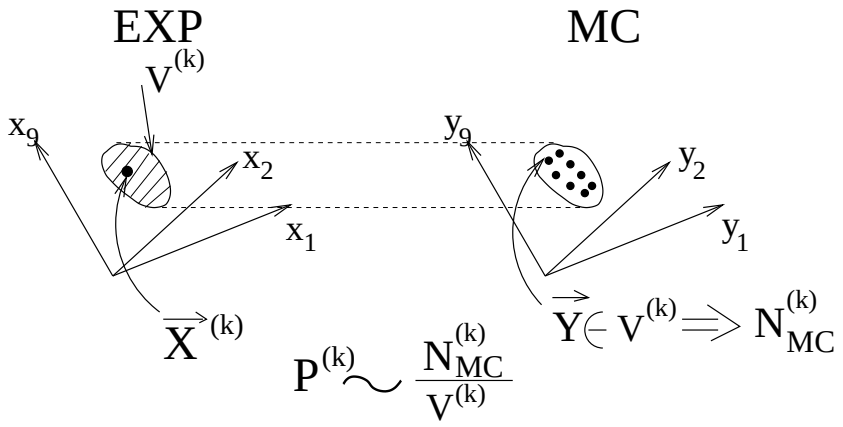

Figure 24: The idea of the MC based method [15].

number of the **selected MC events** $N^{\rm MC}_{\rm other}(x_i)$ in this volume and evaluate PDF (see also Eq. 55):

$$\mathcal{P}_{\rm other}(x_i) = \frac{\varepsilon(x_i) B^{MC}_{\rm other}(x_i)}{\int \varepsilon(x) B^{MC}_{\rm other}(x) dx} = \frac{N^{\rm MC}_{\rm other}(x_i)/V_i}{N^{\rm MC\ TOT}_{\rm other}}, \tag{87}$$

where: $N^{\rm MC\ TOT}_{\rm other}$ is the total number of selected MC events in the whole phase space.

$$\frac{B^{MC}_{\rm other}(x_i)}{\int \frac{\varepsilon(x)}{\varepsilon} B^{MC}_{\rm other}(x) dx} = \frac{\varepsilon}{\varepsilon(x_i)} \mathcal{P}_{\rm other}(x_i), \ \frac{\varepsilon}{\varepsilon(x_i)} = \frac{N^{\rm MC\ TOT}_{\rm signal}}{N^{\rm MC}_{\rm signal}(x_i)} \frac{N^{\rm gen}_{\rm signal}(x_i)}{N^{\rm gen\ TOT}_{\rm signal}}, \tag{88}$$

where: $N^{\rm gen}_{\rm signal}(x_i)$ - number of **generated signal** ($\ell^{\mp}$, $\pi^{\pm}\pi^0$) events in the V_i volume around x_i point, $N^{\rm MC}_{\rm signal}(x_i)$ - number of **selected signal** events in the V_i volume around x_i point, $N^{\rm gen\ TOT}_{\rm signal}$ - total number of generated signal events in the whole phase space, $N^{\rm MC\ TOT}_{\rm signal}$ - total number of selected signal events in the whole phase space. Substituting Eq. 87 into Eq. 88 we get:

$$\frac{B^{MC}_{\rm other}(x_i)}{\int \frac{\varepsilon(x)}{\varepsilon} B^{MC}_{\rm other}(x) dx} = \frac{N^{\rm MC\ TOT}_{\rm signal}}{N^{\rm MC\ TOT}_{\rm other}} \times \frac{N^{\rm MC}_{\rm other}(x_i)}{N^{\rm MC}_{\rm signal}(x_i)} \times \frac{N^{\rm gen}_{\rm signal}(x_i)/V_i}{N^{\rm gen\ TOT}_{\rm signal}} =$$

$$= \frac{1 - \lambda_{3\pi} - \lambda_{\pi} - \lambda_{\rm other}}{\lambda_{\rm other}} \times \frac{N^{\rm MC}_{\rm other}(x_i)}{N^{\rm MC}_{\rm signal}(x_i)} \times Z_{\rm sig} S_{\rm SM}(x_i), \tag{89}$$

where $\lambda_{3\pi} = N_{3\pi}^{\text{MC TOT}}/N_{\text{all}}^{\text{MC TOT}}$, $\lambda_{\pi} = N_{\pi}^{\text{MC TOT}}/N_{\text{all}}^{\text{MC TOT}}$, $\lambda_{\text{other}} = N_{\text{other}}^{\text{MC TOT}}/N_{\text{all}}^{\text{MC TOT}}$, $N_{\text{all}}^{\text{MC TOT}} = N_{\text{signal}}^{\text{MC TOT}} + N_{3\pi}^{\text{MC TOT}} + N_{\pi}^{\text{MC TOT}} + N_{\text{other}}^{\text{MC TOT}}$. The $S_{\text{SM}}(x_i)$ denotes the signal density with Michel parameters fixed to their Standard Model values. As a result Eq. 55 for the total PDF can be rewritten as:

$$\mathcal{P}(x) = \frac{\varepsilon(x)}{\varepsilon} Z_{\text{sig}} \Bigg((1-\lambda_{3\pi}-\lambda_{\pi}-\lambda_{\text{other}}) \frac{S(x)}{\int \frac{\varepsilon(x)}{\varepsilon} S(x) dx} + \lambda_{3\pi} \frac{\varepsilon}{\varepsilon_{3\pi}} \frac{Z_{3\pi}}{Z_{\text{sig}}} \frac{\tilde{B}_{3\pi}(x)}{\int \frac{\varepsilon(x)}{\varepsilon_{3\pi}} \tilde{B}_{3\pi}(x) dx} +$$

$$+\lambda_{\pi} \frac{\tilde{B}_{\pi}(x)}{\int \frac{\varepsilon(x)}{\varepsilon} \tilde{B}_{\pi}(x) dx} + (1-\lambda_{3\pi}-\lambda_{\pi}-\lambda_{\text{other}}) \frac{N_{\text{other}}^{\text{MC}}(x)}{N_{\text{signal}}^{\text{MC}}(x)} S_{\text{SM}}(x) \Bigg), \qquad (90)$$

where the ratio $N_{\text{other}}^{\text{MC}}(x)/N_{\text{signal}}^{\text{MC}}(x)$ is tabulated for each experimental point(event), x, using large generic $\tau^+\tau^-$ MC sample. It will be also helpful to rewrite the extended Eq. 63:

$$\mathcal{P}^{(k)} = \frac{\varepsilon(x^{(k)})}{\varepsilon} Z_{\text{sig}} \Bigg((1-\lambda_{3\pi}-\lambda_{\pi}-\lambda_{\text{other}}) \frac{A_0^{(k)} + A_1^{(k)}\rho + A_2^{(k)}\eta + A_3^{(k)}\xi_\rho\xi + A_4^{(k)}\xi_\rho\xi\delta}{\frac{1}{N_{\text{sel}}^{MC}} \sum_{i=1}^{N_{\text{sel}}^{MC}} \frac{A_0^{(i)} + A_1^{(i)}\rho + A_2^{(i)}\eta + A_3^{(i)}\xi_\rho\xi + A_4^{(i)}\xi_\rho\xi\delta}{A_0^{(i)} + A_1^{(i)}0.75 + A_2^{(i)}0.0 + A_3^{(i)}1.0 + A_4^{(i)}0.75}} +$$

$$+\lambda_{3\pi} \frac{Z_{3\pi}}{Z_{\text{sig}}} \left(\frac{\varepsilon}{\varepsilon_{3\pi}} \right) \frac{\tilde{B}_{3\pi,0}^{(k)} + \tilde{B}_{3\pi,1}^{(k)}\rho + \tilde{B}_{3\pi,2}^{(k)}\eta + \tilde{B}_{3\pi,3}^{(k)}\xi_\rho\xi + \tilde{B}_{3\pi,4}^{(k)}\xi_\rho\xi\delta}{\frac{1}{N_{3\pi,\text{sel}}^{MC}} \sum_{i=1}^{N_{3\pi,\text{sel}}^{MC}} \frac{\tilde{B}_{3\pi,0}^{(i)} + \tilde{B}_{3\pi,1}^{(i)}\rho + \tilde{B}_{3\pi,2}^{(i)}\eta + \tilde{B}_{3\pi,3}^{(i)}\xi_\rho\xi + \tilde{B}_{3\pi,4}^{(i)}\xi_\rho\xi\delta}{\tilde{B}_{3\pi,0}^{(i)} + \tilde{B}_{3\pi,1}^{(i)}0.75 + \tilde{B}_{3\pi,2}^{(i)}0.0 + \tilde{B}_{3\pi,3}^{(i)}1.0 + \tilde{B}_{3\pi,4}^{(i)}0.75}} +$$

$$+\lambda_{\pi} \frac{\tilde{B}_{\pi,0}^{(k)} + \tilde{B}_{\pi,1}^{(k)}\rho + \tilde{B}_{\pi,2}^{(k)}\eta + \tilde{B}_{\pi,3}^{(k)}\xi_\rho\xi + \tilde{B}_{\pi,4}^{(k)}\xi_\rho\xi\delta}{\frac{1}{N_{\text{sel}}^{MC}} \sum_{i=1}^{N_{\text{sel}}^{MC}} \frac{\tilde{B}_{\pi,0}^{(i)} + \tilde{B}_{\pi,1}^{(i)}\rho + \tilde{B}_{\pi,2}^{(i)}\eta + \tilde{B}_{\pi,3}^{(i)}\xi_\rho\xi + \tilde{B}_{\pi,4}^{(i)}\xi_\rho\xi\delta}{A_0^{(i)} + A_1^{(i)}0.75 + A_2^{(i)}0.0 + A_3^{(i)}1.0 + A_4^{(i)}0.75}} +$$

$$+(1-\lambda_{3\pi}-\lambda_{\pi}-\lambda_{\text{other}}) \frac{N_{\text{other}}^{\text{MC}}(x^{(k)})}{N_{\text{signal}}^{\text{MC}}(x^{(k)})} (A_0^{(k)} + A_1^{(k)}0.75 + A_2^{(k)}0.0 + A_3^{(k)}1.0 + A_4^{(k)}0.75) \Bigg), \qquad (91)$$

In reality, it is difficult to tabulate PDF in the 9D phase space taking into account all correlations with the acceptable accuracy (even large generic $\tau\tau$ MC sample available at Belle is quite far from to be enough). Number of the kinematical variables to tabulate PDF somehow should be reduced. We should find the main kinematical variables which allow us to describe essential features of the PDF. The dependence of the PDF on the remaining kinematical variables can be tabulated independently and added to the total

PDF as a separate multiplier(s). Another approach is just to integrate PDF over the remaining kinematical variables.

To find the main kinematical variables (to take into account the largest correlations) we monitored all 36 2D-correlations and 84 3D-correlations and found 11 notable 2D-correlations, see Fig. 25. All visible 3D-correlations are

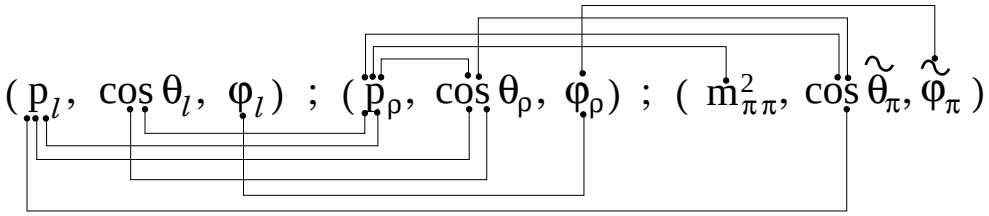

Figure 25: The largest 2D-correlations in the 9D phase space.

induced by these 11 2D-correlations. Some of the correlations are shown in Fig. 26, 27. Strong correlations are seen between lepton momentum

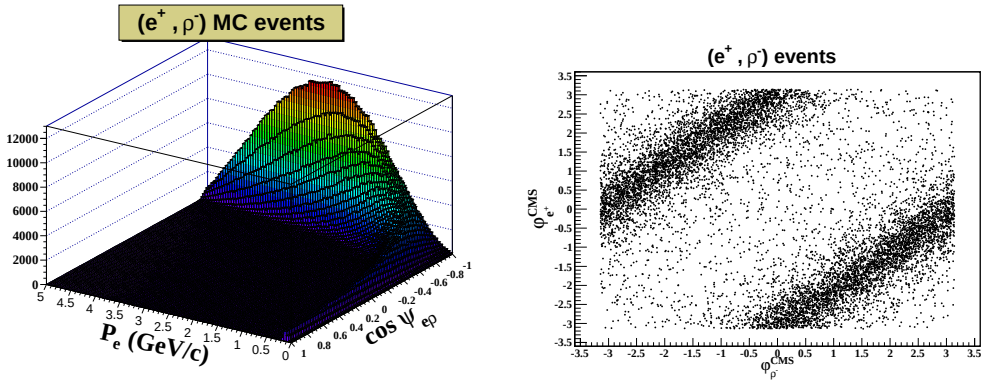

Figure 26: 2D-correlations: lepton momentum (P_e) versus cosine of the spatial angle between lepton and ρ in CMS ($\cos\psi_{e\rho}$) for the (e^+; ρ^-) events (left), lepton azimuthal angle ($\varphi^{\rm CMS}_{e^+}$) versus ρ azimuthal angle in CMS ($\varphi^{\rm CMS}_{\rho^-}$) for the ($e^+$; ρ^-) events (right).

and cosine of the spatial angle between lepton and ρ in CMS as well as between azimuthal angles of lepton and ρ in CMS. To take into account these correlations explicitely we can consider PDF for the following set of the kinematical variables: (p_ℓ, $\cos\psi_{\ell\rho}$, $\Delta\varphi_{\ell\rho}$; p_ρ, $\cos\theta_\rho$, φ_ρ; $m^2_{\pi\pi}$, $\cos\tilde{\theta}_\pi$, $\tilde{\varphi}_\pi$)

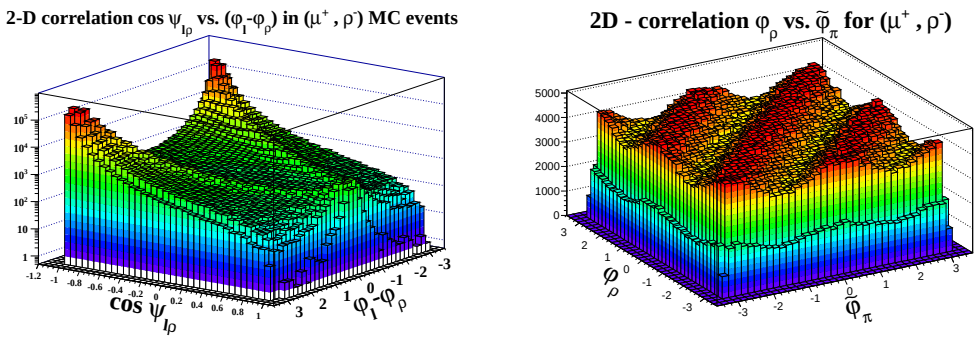

Figure 27: 2D-correlations: cosine of the spatial angle between lepton and ρ ($\cos\psi_{l\rho}$) versus difference of the lepton and ρ azimuthal angles in CMS ($\varphi_l - \varphi_\rho$) for the (μ^+; ρ^-) events (left), ρ azimuthal angle in CMS (φ_ρ) versus azimuthal angle of charged pion in the ρ rest frame ($\tilde{\varphi}_\pi$) for the (μ^+; ρ^-) events (right).

(θ_ℓ and φ_ℓ are changed by $\psi_{\ell\rho}$(spatial angle between ℓ and ρ) and $\Delta\varphi_{\ell\rho} = \varphi_\ell - \varphi_\rho$). The main 2D-correlations in this case are shown in Fig. 28.

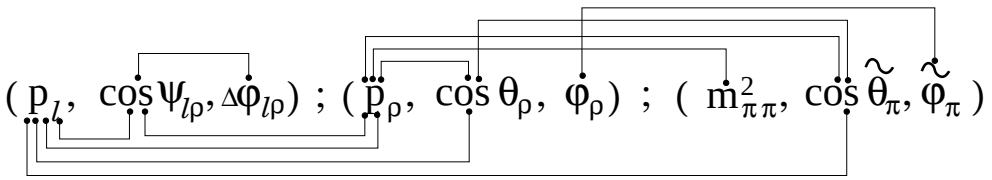

Figure 28: The largest 2D-correlations in the 9D phase space, θ_ℓ and φ_ℓ are changed by $\psi_{\ell\rho}$(spatial angle between ℓ and ρ) and $\Delta\varphi_{\ell\rho} = \varphi_\ell - \varphi_\rho$.

Figure 25 helps us to realize that if we introduce $\Delta\varphi_{\ell\rho} = \varphi_\ell - \varphi_\rho$ variable, the $\Delta\varphi_{\ell\rho}$ and (φ_ρ, $\tilde{\varphi}_\pi$) are decoupled from the remaining six variables (p_ℓ, $\cos\theta_\ell$, p_ρ, $\cos\theta_\rho$, $m^2_{\pi\pi}$, $\cos\tilde{\theta}_\pi$). So, the total PDF, $\mathcal{P}_{\rm tot}$, can be written as a product of three independent PDFs:

$$\mathcal{P}_{\rm tot} = \mathcal{P}_{\rm 6D}(p_\ell,\ \cos\theta_\ell,\ p_\rho,\ \cos\theta_\rho,\ m^2_{\pi\pi},\ \cos\tilde{\theta}_\pi)\mathcal{P}_{\rm 2D}(\varphi_\rho,\ \tilde{\varphi}_\pi)\mathcal{P}_{\rm 1D}(\Delta\varphi_{\ell\rho}).$$

From Fig. 28 it is clear that the (φ_ρ, $\tilde{\varphi}_\pi$) 2D-subspace is decoupled from the remaining 7D-subspace (p_ℓ, $\cos\psi_{\ell\rho}$, $\Delta\varphi_{\ell\rho}$, p_ρ, $\cos\theta_\rho$, $m^2_{\pi\pi}$, $\cos\tilde{\theta}_\pi$), so the total PDF can be written as a product of two independent PDFs:

$$\mathcal{P}_{\rm tot} = \mathcal{P}_{\rm 7D}(p_\ell,\ \cos\psi_{\ell\rho},\ \Delta\varphi_{\ell\rho},\ p_\rho,\ \cos\theta_\rho,\ m^2_{\pi\pi},\ \cos\tilde{\theta}_\pi)\mathcal{P}_{\rm 2D}(\varphi_\rho,\ \tilde{\varphi}_\pi).$$

For each of $\mathcal{P}_{7\mathrm{D}}$, $\mathcal{P}_{6\mathrm{D}}$, $\mathcal{P}_{2\mathrm{D}}$, $\mathcal{P}_{1\mathrm{D}}$ PDFs we use MC based method described in [15]. Actually, we tested various schemes for the total PDF, some of them are presented below:

- $\mathcal{P}_{1\mathrm{D}}(p_\ell)\cdot\mathcal{P}_{1\mathrm{D}}(\cos\theta_\ell)\cdot\mathcal{P}_{1\mathrm{D}}(\varphi_\ell)\cdot\mathcal{P}_{1\mathrm{D}}(p_\rho)\cdot\mathcal{P}_{1\mathrm{D}}(\cos\theta_\rho)\cdot\mathcal{P}_{1\mathrm{D}}(\varphi_\rho)\cdot\mathcal{P}_{1\mathrm{D}}(m^2_{\pi\pi})\cdot\mathcal{P}_{1\mathrm{D}}(\cos\tilde{\theta}_\pi)\cdot\mathcal{P}_{1\mathrm{D}}(\tilde{\varphi}_\pi)$: each of 9 1D-PDFs is tabulated independently, correlations are not taken into account;

- $\mathcal{P}_{6\mathrm{D}}(p_\ell,\ \cos\theta_\ell,\ p_\rho,\ \cos\theta_\rho,\ m^2_{\pi\pi},\ \cos\tilde{\theta}_\pi)\cdot\mathcal{P}_{2\mathrm{D}}(\varphi_\rho,\ \tilde{\varphi}_\pi)\cdot\mathcal{P}_{1\mathrm{D}}(\Delta\varphi_{\ell\rho})$: all correlations are taken into account, poor accuracy of the tabulation of the $\mathcal{P}_{6\mathrm{D}}$, Fig. 29 shows the distributions of $N^{\mathrm{MC}}_{\mathrm{other}}(x)$ and $N^{\mathrm{MC}}_{\mathrm{signal}}(x)$ for the 6D-part, 2D-part and 1D-part;

- $\mathcal{P}_{7\mathrm{D}}(p_\ell,\ \cos\psi_{\ell\rho},\ \Delta\varphi_{\ell\rho},\ p_\rho,\ \cos\theta_\rho,\ m^2_{\pi\pi},\ \cos\tilde{\theta}_\pi)\cdot\mathcal{P}_{2\mathrm{D}}(\varphi_\rho,\ \tilde{\varphi}_\pi)$: all correlations are taken into account, poor accuracy of the tabulation of the $\mathcal{P}_{7\mathrm{D}}$;

- $\mathcal{P}_{7\mathrm{D}}(p_\ell,\ \cos\theta_\ell,\ p_\rho,\ \cos\theta_\rho,\ \Delta\varphi_{\ell\rho},\ \cos\tilde{\theta}_\pi,\ \tilde{\varphi}_\pi)$: integrated over 2 kinematical variables, most of the correlations are taken into account, poor accuracy of the $\mathcal{P}_{7\mathrm{D}}$ tabulation, Fig. 30 shows the distributions of $N^{\mathrm{MC}}_{\mathrm{other}}(x_{7\mathrm{D}})$ and $N^{\mathrm{MC}}_{\mathrm{signal}}(x_{7\mathrm{D}})$ for this scheme;

- $\mathcal{P}_{6\mathrm{D}}(p_\ell,\ \cos\theta_\ell,\ p_\rho,\ \cos\theta_\rho,\ m^2_{\pi\pi},\ \Delta\varphi_{\ell\rho})$: integrated over 3 kinematical variables, most of the correlations are taken into account, poor accuracy of the $\mathcal{P}_{6\mathrm{D}}$ tabulation;

- $\mathcal{P}_{5\mathrm{D}}(p_\ell,\ \cos\theta_\ell,\ p_\rho,\ \cos\theta_\rho,\ m^2_{\pi\pi})$: integrated over 4 kinematical variables, the main correlations are taken into account, poor accuracy of the $\mathcal{P}_{5\mathrm{D}}$ tabulation;

- $\mathcal{P}_{4\mathrm{D}}(p_\ell,\ p_\rho,\ \omega,\ \cos\psi_{\ell\rho})$($\omega$ is helicity sensitive variable, defined in Eq. 27): reduced PDF, the main correlations are taken into account;

- $\mathcal{P}_{4\mathrm{D}}(p_\ell,\ p_\rho,\ \omega,\ \cos\psi_{\ell\rho})\cdot\mathcal{P}_{1\mathrm{D}}(\varphi_\ell)\cdot\mathcal{P}_{1\mathrm{D}}(\varphi_\rho)\cdot\mathcal{P}_{1\mathrm{D}}(m^2_{\pi\pi})\cdot\mathcal{P}_{1\mathrm{D}}(\cos\tilde{\theta}_\pi)\cdot\mathcal{P}_{1\mathrm{D}}(\tilde{\varphi}_\pi)$: the main correlations are taken into account in the $\mathcal{P}_{4\mathrm{D}}$, all the other kinematical variables are included in the PDF multiplicatively;

- $\mathcal{P}_{3\mathrm{D}}(p_\ell,\ p_\rho,\ \cos\psi_{\ell\rho})$: reduced 3D-PDF, tabulated with high accuracy, Fig. 31 shows the distributions of $N^{\mathrm{MC}}_{\mathrm{other}}(x_{3\mathrm{D}})$ and $N^{\mathrm{MC}}_{\mathrm{signal}}(x_{3\mathrm{D}})$ for this scheme;

- $\mathcal{P}_{3D}(p_\ell,\ p_\rho,\ \omega)$: reduced 3D-PDF, tabulated with high accuracy, Fig. 32 shows the distributions of $N^{MC}_{other}(x_{3D})$ and $N^{MC}_{signal}(x_{3D})$ for this scheme;
- $\mathcal{P}_{3D}(p_\ell,\ \cos\psi_{\ell\rho},\ \omega)$: reduced 3D-PDF, tabulated with high accuracy;
- $\mathcal{P}_{2D}(p_\ell,\ \cos\psi_{\ell\rho})$: reduced 2D-PDF, tabulated with high accuracy;
- $\mathcal{P}_{2D}(p_\ell,\ \omega)$: reduced 2D-PDF, tabulated with high accuracy;
- $\mathcal{P}_{5D}(p_\ell,\ \cos\psi_{\ell\rho},\ p_\rho,\ \cos\theta_\rho,\ \cos\tilde{\theta}_\pi)\cdot\mathcal{P}_{2D}(\varphi_\rho,\ \tilde{\varphi}_\pi)\cdot\frac{\mathcal{P}_{2D}(p_\rho,\ m^2_{\pi\pi})}{\mathcal{P}_{1D}(p_\rho)}\cdot\frac{\mathcal{P}_{2D}(\cos\psi_{\ell\rho},\ \Delta\varphi_{\ell\rho})}{\mathcal{P}_{1D}(\cos\psi_{\ell\rho})}$: in this scheme all 2D-correlations are taken into account, poor accuracy of the $\mathcal{P}_{5D}$ tabulation;
- $\mathcal{P}_{3D}(p_\ell,\ \cos\psi_{\ell\rho},\ p_\rho)\cdot\mathcal{P}_{2D}(\varphi_\rho,\ \tilde{\varphi}_\pi)\cdot\frac{\mathcal{P}_{2D}(p_\ell,\ \cos\theta_\rho)}{\mathcal{P}_{1D}(p_\ell)}\cdot\frac{\mathcal{P}_{2D}(p_\rho,\ \cos\tilde{\theta}_\pi)}{\mathcal{P}_{1D}(p_\rho)}\cdot\frac{\mathcal{P}_{2D}(p_\rho,\ m^2_{\pi\pi})}{\mathcal{P}_{1D}(p_\rho)}\cdot\frac{\mathcal{P}_{2D}(\cos\psi_{\ell\rho},\ \Delta\varphi_{\ell\rho})}{\mathcal{P}_{1D}(\cos\psi_{\ell\rho})}$: in this scheme all 2D-correlations are taken into account, $\mathcal{P}_{3D}$ is tabulated with high accuracy.

As the total number of experimental(MC) events is of the order of 10 million, to tabulate the $N^{MC}_{other}(x)/N^{MC}_{signal}(x)$ ratio we have to perform double cycle of about $10M\times10M$ size (i.e. $\sim 10^{14}$ standard calculations), which is quite CPU heavy operation. To reduce CPU time we applied simple parallelization algorithm, namely whole MC sample was subdivided into about 120 subsamples, so that each subsample is processed by a separate CPU core. After that all subsamples are processed simultaneously by 120 CPU cores, it takes $20\div40$ hours to tabulate $N^{MC}_{other}(x)/N^{MC}_{signal}(x)$ ratio for all experimental events.

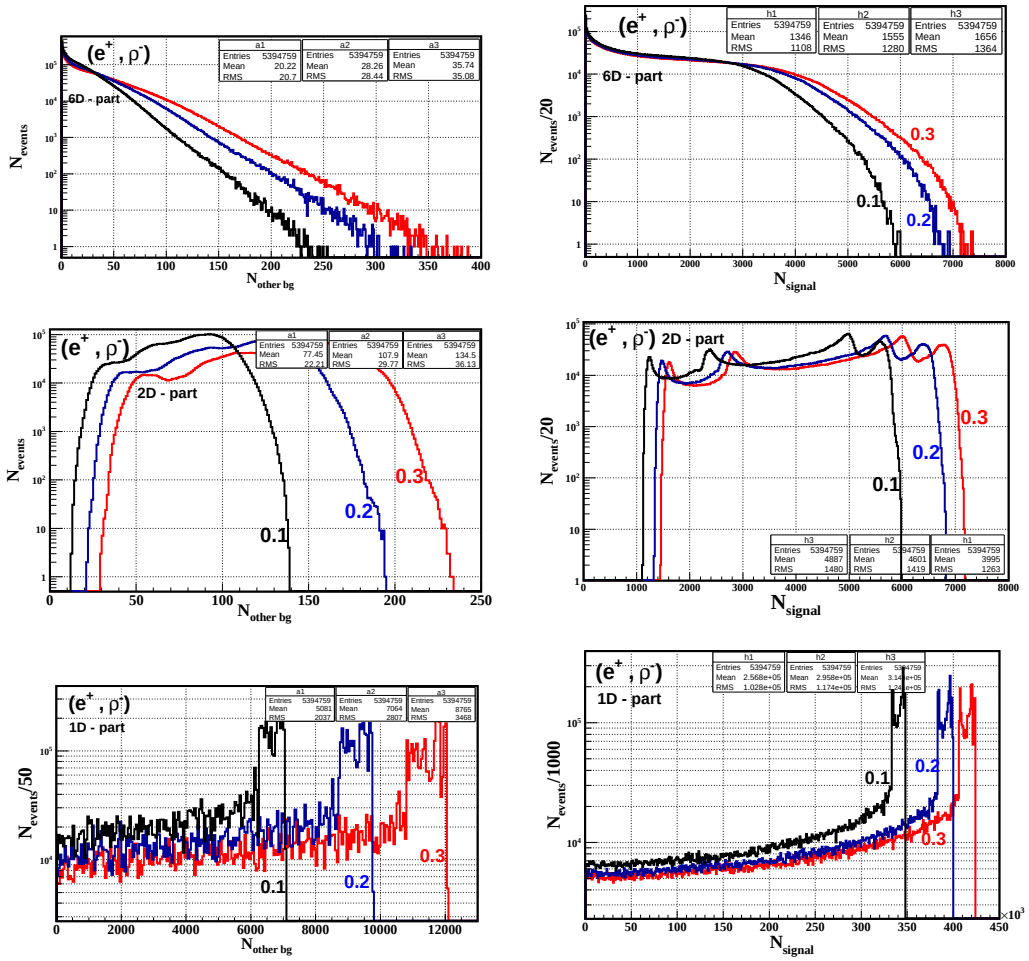

Figure 29: Distributions of $N^{\rm MC}_{\rm other}(x)$ (left) and $N^{\rm MC}_{\rm signal}(x)$ (right) in the 6D $\times$ 2D $\times$ 1D-scheme for the $(e^+;\ \rho^-)$ events, 6D-PDF component (top), 2D-PDF component (middle), 1D-PDF component for three different cuts on the extra γ energy ($E^{\rm LAB}_{\gamma\ \rm rest} < 0.1,\ 0.2,\ 0.3$ GeV/c^2).

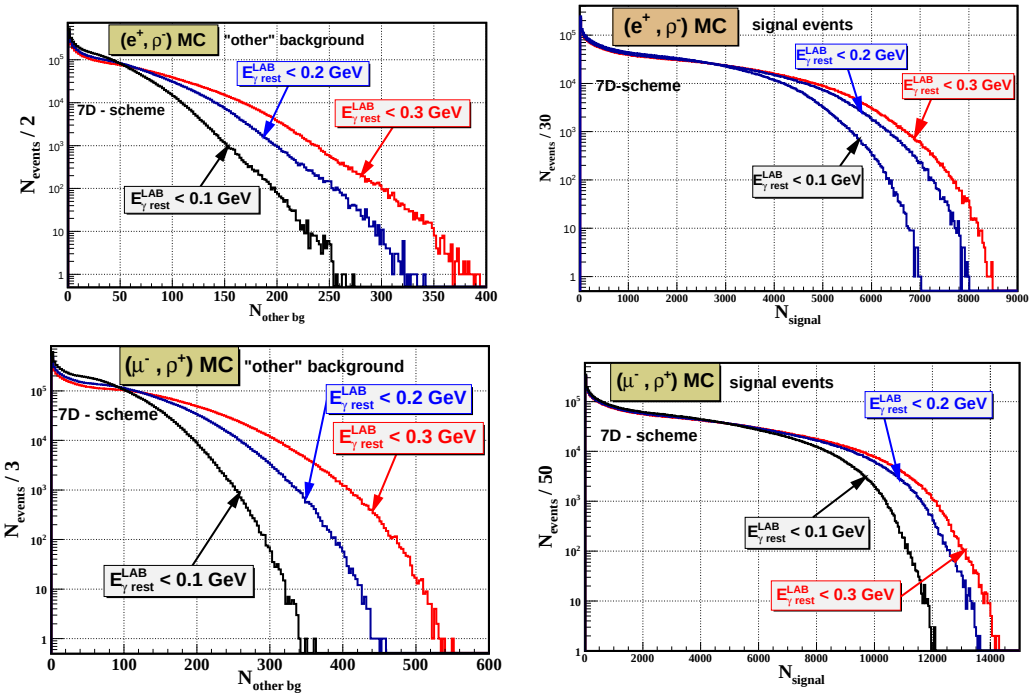

Figure 30: Distributions of $N^{\rm MC}_{\rm other}(x_{\rm 7D})$ (left) and $N^{\rm MC}_{\rm signal}(x_{\rm 7D})$ (right) in the 7D-scheme for the $(e^+;\ \rho^-)$ (top) and $(\mu^-;\ \rho^+)$ (bottom) events for three different cuts on the extra γ energy ($E^{\rm LAB}_{\gamma\ \rm rest} < 0.1,\ 0.2,\ 0.3$ GeV/c^2).

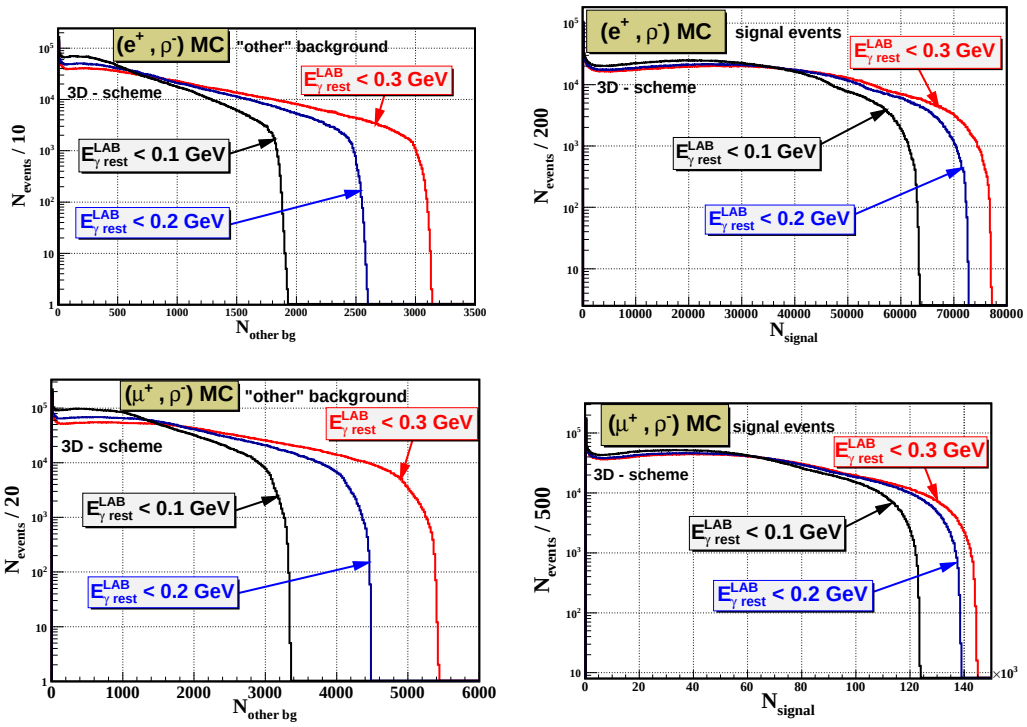

Figure 31: Distributions of $N^{\rm MC}_{\rm other}(x_{\rm 3D})$ (left) and $N^{\rm MC}_{\rm signal}(x_{\rm 3D})$ (right) in the 3D-scheme for the $(e^+;\ \rho^-)$ (top) and $(\mu^+;\ \rho^-)$ (bottom) events for three different cuts on the extra γ energy ($E^{\rm LAB}_{\gamma\ \rm rest} < 0.1,\ 0.2,\ 0.3$ GeV/c^2).

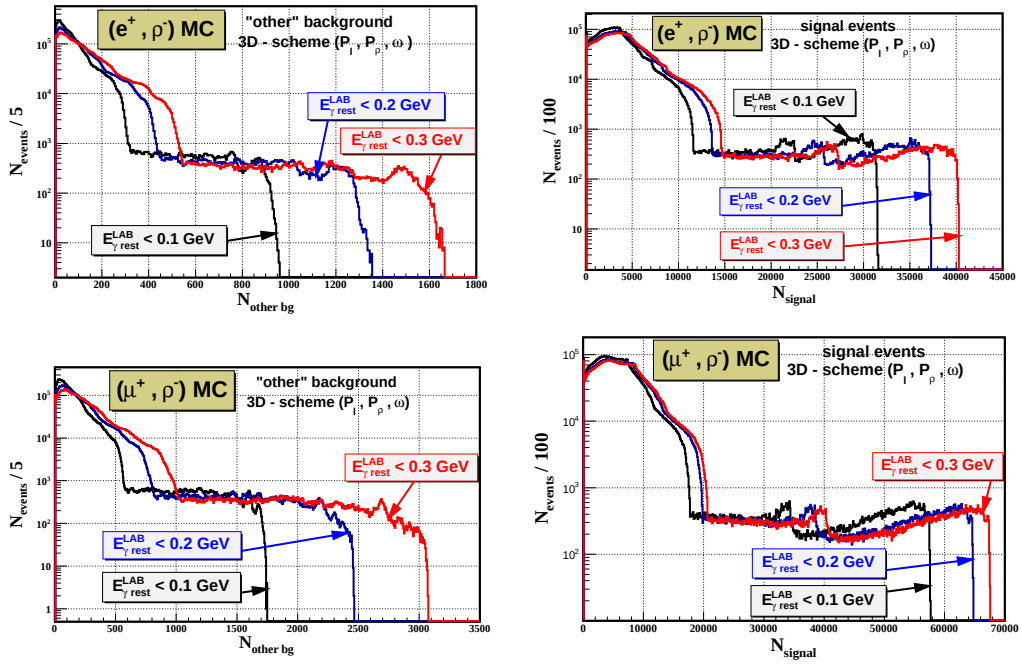

Figure 32: Distributions of $N^{\rm MC}_{\rm other}(x_{\rm 3D})$ (left) and $N^{\rm MC}_{\rm signal}(x_{\rm 3D})$ (right) in the 3D-scheme($\mathcal{P}_{\rm 3D}(p_\ell,\ p_\rho,\ \omega)$) for the $(e^+;\ \rho^-)$ (top) and $(\mu^+;\ \rho^-)$ (bottom) events for three different cuts on the extra γ energy ($E^{\rm LAB}_{\gamma\ \rm rest}$ $<$ 0.1, 0.2, 0.3 GeV/c^2).

5 Validation of the fit procedure

Validation of the fitter was done using full generic $\tau^+\tau^-$ MC data sample (of the CASEA type) available at Nagoya cluster. We selected about 4×10M events of 4 configurations $(\ell^\mp,\ \rho^\pm)$ $(\ell = e,\ \mu)$. The following tests have been done:

- fit of only signal MC $(\ell^\mp;\ \pi^\pm\pi^0)$ $(\ell = e,\ \mu)$ events;
- fit of only background MC $(\ell^\mp;\ \pi^\pm\pi^0\pi^0)$ $(\ell = e,\ \mu)$ events;
- fit of the signal + dominant background $((e^\mp;\ \pi^\pm\pi^0) + (e^\mp;\ \pi^\pm\pi^0\pi^0)$ or $(\mu^\mp;\ \pi^\pm\pi^0) + (\mu^\mp;\ \pi^\pm\pi^0\pi^0) + (\pi^\mp;\ \pi^\pm\pi^0))$ events;
- fit of all selected MC events (i.e. $(e^\mp;\ \pi^\pm\pi^0) + (e^\mp;\ \pi^\pm\pi^0\pi^0)$+"other" or $(\mu^\mp;\ \pi^\pm\pi^0) + (\mu^\mp;\ \pi^\pm\pi^0\pi^0) + (\pi^\mp;\ \pi^\pm\pi^0)$+"other")

For each configuration 10M MC data sample has been splitted into two statistically independent 5M parts. The first subsample is used to calculate normalization, and the second one is fitted to extract Michel parameters (MP). Due to the strong $\frac{m_e}{M_\tau}$ suppression of the term containing η MP (see Eq. 8) $(e^\mp;\ \pi^\pm\pi^0)$ events are not sensitive to the η MP. That is why in the fit of $(e^\mp;\ \pi^\pm\pi^0)$ events we fixed η MP to its SM value $(\eta = 0)$.

To study validity of the fitter we also performed the fits of the MC samples with different non-SM values of MP. For each SM value of MP we produced the samples with the MP shifted by $\pm 3\sigma$, $\pm 6\sigma$ and $\pm 10\sigma$, where σ is statistical uncertainty of the particular MP in the fit. Such samples were prepared from the initial one (generated with the SM values of MP) with help of the reweighting method.

Table 6 shows result of the fit of the signal $(e^\mp;\ \pi^\pm\pi^0)$ MC samples. In Fig. 33 electron energy spectrum and disribution of the likelihood per event are shown for the fitted $(e^-;\ \pi^+\pi^0)$ MC sample, histograms show the theoretical expectations while points with errors – fitted MC data.

Electron and ρ energy spectra for three different regions in the tau helicity sensitive parameter, ω (see Eq. 27), for $(e^-;\ \pi^+\pi^0)$ events are shown in Fig. 34, 35. The effect of spin-spin correlation of taus is clearly seen (compare also Fig. 34 with Fig. 7). Study of the fitter bias for $(e^\pm;\ \pi^\mp\pi^0)$ events is demonstrated in Fig. 36, 37. It is seen that there is no notable bias on the level of 10^{-3} for all Michel parameters.

Table 6: Result of the fit of 5M MC samples: $(e^+;\ \pi^-\pi^0)$ (left) and $(e^-;\ \pi^+\pi^0)$ (right).

$(e^+;\ \pi^-\pi^0)$				
ρ	=	0.7506	$\pm$	0.0010
η	=	0	-	fixed
ξ	=	1.0026	$\pm$	0.0043
$\xi\delta$	=	0.7544	$\pm$	0.0027

$(e^-;\ \pi^+\pi^0)$				
ρ	=	0.7497	$\pm$	0.0010
η	=	0	-	fixed
ξ	=	1.0016	$\pm$	0.0043
$\xi\delta$	=	0.7510	$\pm$	0.0027

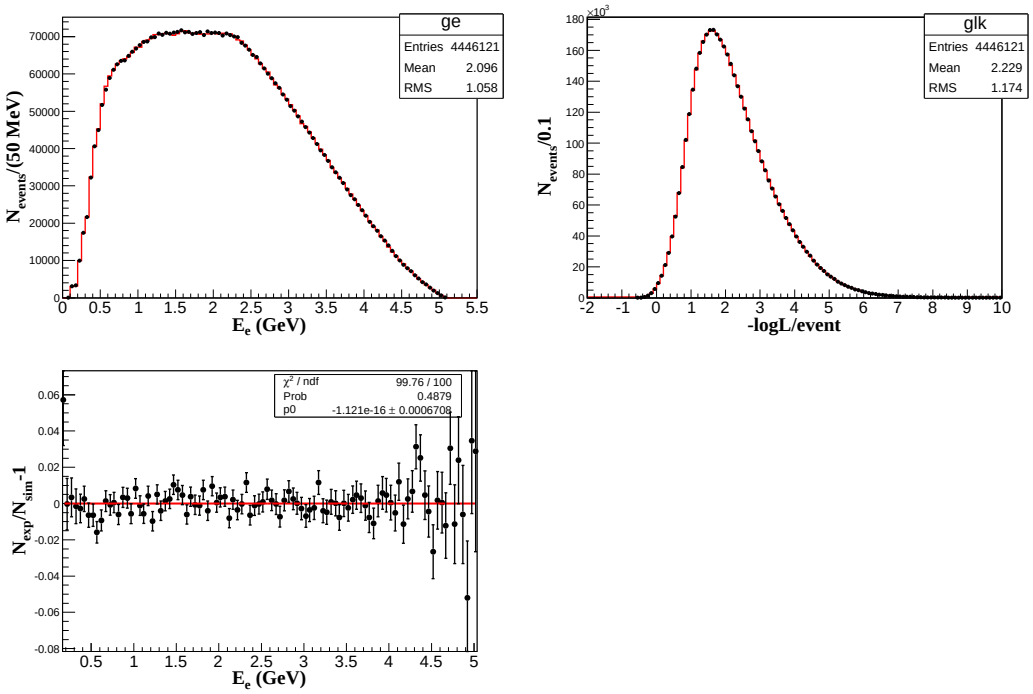

Figure 33: Result of the fit of 5M MC $(e^-;\ \pi^+\pi^0)$ events. Electron energy spectrum (left) and disribution of the likelihood per event (right), histograms show the theoretical expectations, points with errors – fitted MC data. Relative difference of the expected energy spectrum and fitted one shows good quality of the fit.

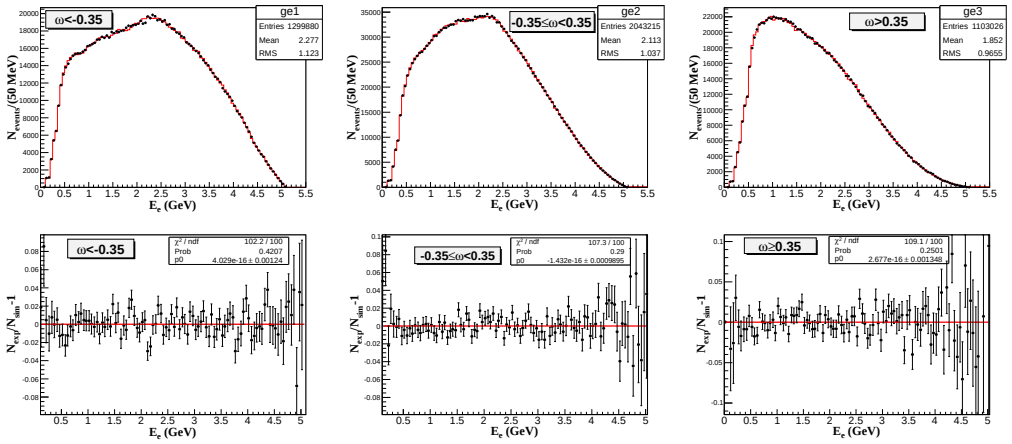

Figure 34: Electron energy spectra for three different regions in ω parameter: $\omega < -0.35$ (left), $-0.35 < \omega < 0.35$ (middle), $\omega > 0.35$ (right). The effect of spin-spin correlation of taus is demonstrated by the difference of these spectrum shapes.

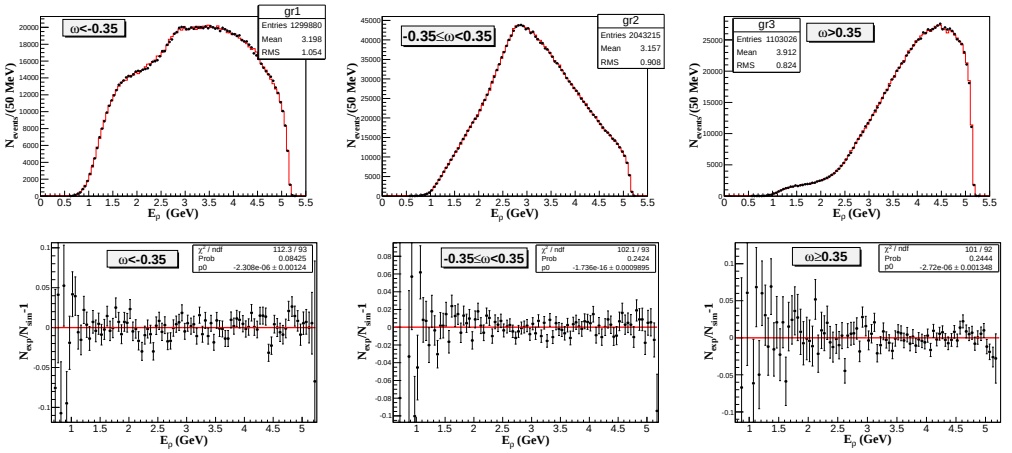

Figure 35: ρ energy spectra for three different regions in ω parameter: $\omega < -0.35$ (left), $-0.35 < \omega < 0.35$ (middle), $\omega > 0.35$ (right). The effect of spin-spin correlation of taus is demonstrated by the difference of these spectrum shapes.

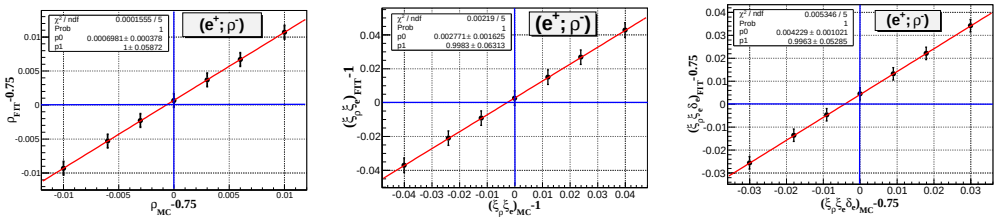

Figure 36: Study of the fitter bias for $(e^+;\ \pi^-\pi^0)$ events. Dependences of the fit results versus generator values are shown for Michel parameters (deviations from the SM values): $\rho - 0.75$ (left), $\xi_\rho\xi - 1$ (middle), $\xi_\rho\xi\delta - 0.75$ (right).

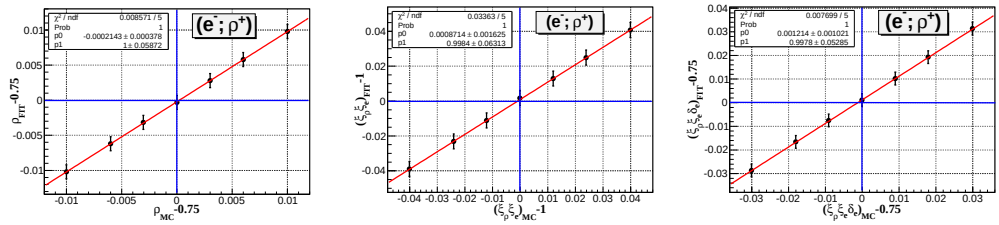

Figure 37: Study of the fitter bias for $(e^-;\ \pi^+\pi^0)$ events. Dependences of the fit results versus generator values are shown for Michel parameters (deviations from the SM values): $\rho - 0.75$ (left), $\xi_\rho\xi - 1$ (middle), $\xi_\rho\xi\delta - 0.75$ (right).

Table 7 shows result of the fit of $(\mu^{\mp};\ \pi^{\pm}\pi^0)$ MC samples. In Fig. 38 μ^+ energy spectrum and disribution of the likelihood per event are shown for the fitted $(\mu^+;\ \pi^-\pi^0)$ MC sample, histograms show the theoretical expectations while points with errors – fitted MC data. In the fit of only $(\mu^-;\ \pi^+\pi^0)$ MC events we observe small, but notable bias ($\sim (1 \div 3)\%$) for ρ, η and ξ Michel parameters. μ^+ and ρ^- energy spectra for three different regions in

Table 7: Result of the fit of 5M MC samples: $(\mu^+;\ \pi^-\pi^0)$ (left) and $(\mu^-;\ \pi^+\pi^0)$ (right).

$(\mu^+;\ \pi^-\pi^0)$				
ρ	=	0.7468	$\pm$	0.0026
η	=	-0.0083	$\pm$	0.0101
ξ	=	0.9933	$\pm$	0.0050
$\xi\delta$	=	0.7501	$\pm$	0.0032

$(\mu^-;\ \pi^+\pi^0)$				
ρ	=	0.7600	$\pm$	0.0027
η	=	0.0280	$\pm$	0.0102
ξ	=	1.0140	$\pm$	0.0051
$\xi\delta$	=	0.7512	$\pm$	0.0032

the tau helicity sensitive parameter, ω, for $(\mu^+;\ \pi^-\pi^0)$ events are shown in Fig. 39, 40. The effect of spin-spin correlation of taus is clearly seen (compare also Fig. 39 with Fig. 7). Study of the fitter bias for $(\mu^{\pm};\ \pi^{\mp}\pi^0)$ events is demonstrated in Fig. 50, 51. It is seen that for the $(\mu^-;\ \pi^+\pi^0)$ MC events the observed bias is reproduced also for the non-SM generator values of Michel parameters.

It was found that the observed bias comes from the finite statistical accuracy of the normalisation coefficients $C_i,\ i = 0 \div 4$. Fig. 41-44 show the distributions of $B_i^{(k)},\ i = 0 \div 4$, see Eq. 39, they are used in the evaluation of the normalisation coefficients C_i, which are simply mean values of the corresponding $B_i^{(k)}$-histograms. Coefficients C_i are calculated for the MC sample, which is actually used for the normalisation, as well as for the MC sample, which is used for the fit. The values C_i obtained for the $E^{LAB}_{\mathrm{rest}\gamma} < 40$ MeV cut (where we observe the largest bias) are summarized in Table 8. Two coefficients provide the dominant contribution to the total normalisation, C_0 and C_1. While the relative statistical uncertainty of the C_0 coefficient is about 0.03%, the uncertainty of the C_1 coefficient is much larger - about 0.5%.

To check the effect of the finite accuracy of the normalization coefficients MC sample was separated into 5 subsamples (with almost equal statistics), four subsamples (streams) were used to calculate normalization and one stream was used in the fit. Table 9 shows fit result for the $(\mu^{\pm};\ \pi^{\mp}\pi^0)$ events. Figure 45 demonstrates 1σ-, 2σ- and 3σ-contours of the likelihood

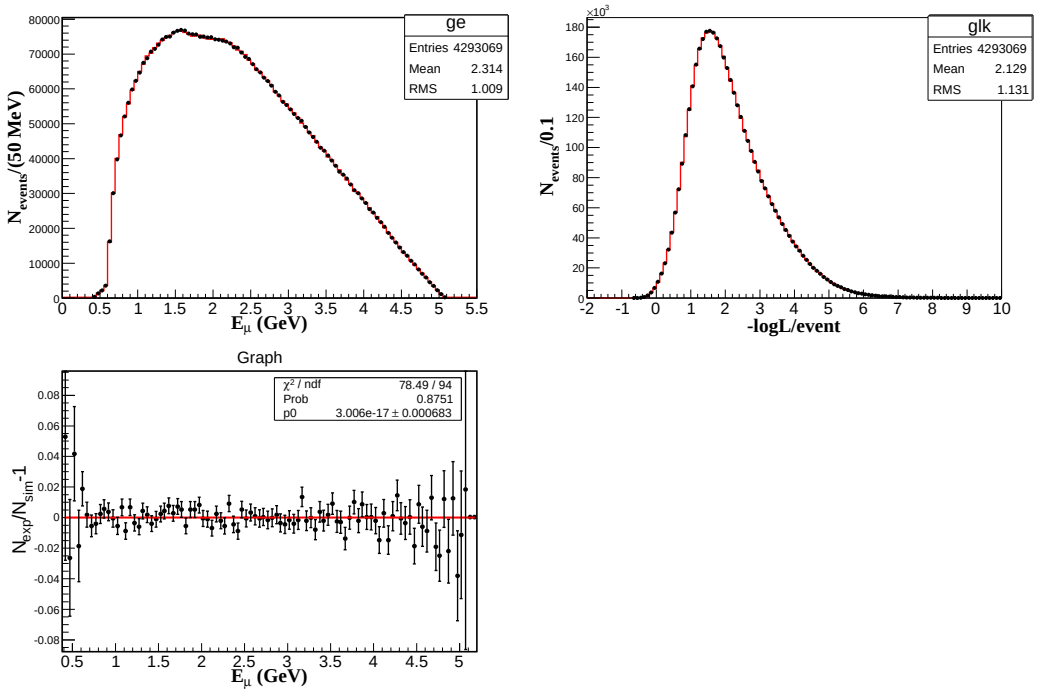

Figure 38: Result of the fit of 5M MC ($\mu^+;\ \pi^-\pi^0$) events. Muon energy spectrum (left) and disribution of the likelihood per event (right), histograms show the theoretical expectations, points with errors – fitted MC data. Relative difference of the expected energy spectrum and fitted one shows good quality of the fit.

Table 8: Normalisation coefficients C_i for the ($\mu^+;\ \pi^-\pi^0$) and ($\mu^-;\ \pi^+\pi^0$) events. Energy of additional photons in laboratory frame was required to be $E^{LAB}_{\mathrm{rest}\gamma} < 40$ MeV.

C_i	($\mu^+;\ \pi^-\pi^0$)		($\mu^-;\ \pi^+\pi^0$)	
	norm.	fit	norm.	fit
C_0	0.93958 ± 0.00027	0.94053 ± 0.00027	0.94055 ± 0.00027	0.94028 ± 0.00027
C_1	0.07206 ± 0.00034	0.07104 ± 0.00034	0.07075 ± 0.00034	0.07121 ± 0.00034
C_2	0.18983 ± 0.00009	0.19007 ± 0.00009	0.19029 ± 0.00009	0.19027 ± 0.00009
C_3	0.00810 ± 0.00008	0.00821 ± 0.00008	0.00805 ± 0.00008	0.00820 ± 0.00008
C_4	-0.00230 ± 0.00013	-0.00269 ± 0.00013	-0.00222 ± 0.00013	-0.00250 ± 0.00013

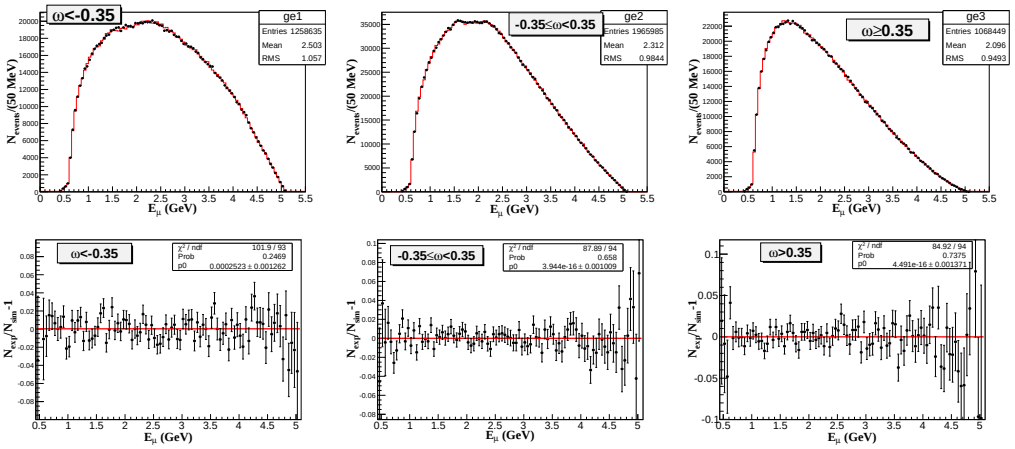

Figure 39: Muon energy spectra for three different regions in ω parameter: $\omega < -0.35$ (left), $-0.35 < \omega < 0.35$ (middle), $\omega > 0.35$ (right). The effect of spin-spin correlation of taus is demonstrated by the difference of these spectrum shapes.

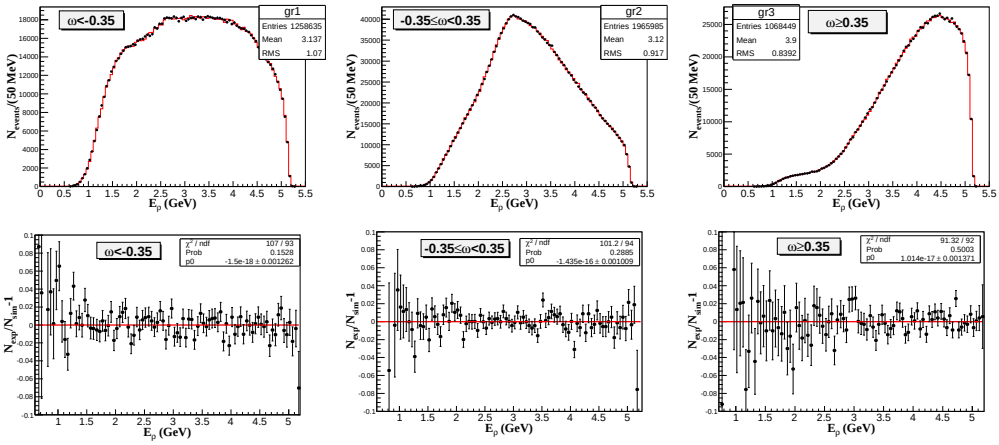

Figure 40: ρ^- energy spectra for three different regions in ω parameter: $\omega < -0.35$ (left), $-0.35 < \omega < 0.35$ (middle), $\omega > 0.35$ (right). The effect of spin-spin correlation of taus is demonstrated by the difference of these spectrum shapes.

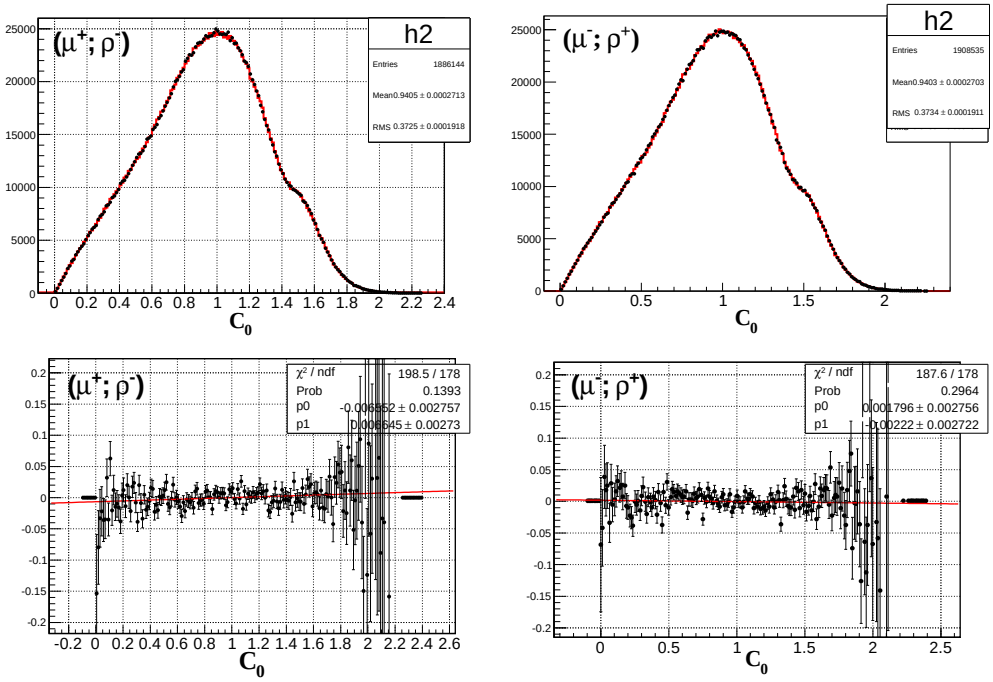

Figure 41: Distribution of $B_0^{(k)}$ for the $(\mu^+;\ \pi^-\pi^0)$ (upper left) and $(\mu^-;\ \pi^+\pi^0)$ (upper right) events (see Eq. 39, the mean value of this distribution gives normalisation coefficient $C_0 = (1/N_{\rm MC}) \cdot \sum_{k=1}^{N_{\rm MC}} B_0^{(k)}$). Red histogram shows the distribution for the MC sample used to calculate normalisation coefficients ($C_0(\text{norm}) = 0.93958 \pm 0.00027$ for the $(\mu^+;\ \pi^-\pi^0)$ events, $C_0(\text{norm}) = 0.94055 \pm 0.00027$ for the $(\mu^-;\ \pi^+\pi^0)$ events), points with errors - for the MC sample used in the fit ($C_0(\text{fit}) = 0.94053 \pm 0.00027$ for the $(\mu^+;\ \pi^-\pi^0)$ events, $C_0(\text{fit}) = 0.94028 \pm 0.00027$ for the $(\mu^-;\ \pi^+\pi^0)$ events). Relative difference of the distributions for normalisation MC sample and for the fit MC sample is also shown for the $(\mu^+;\ \pi^-\pi^0)$ (lower left) and $(\mu^-;\ \pi^+\pi^0)$ (right) events. Red line shows the result of the fit by the first order polynomial function.

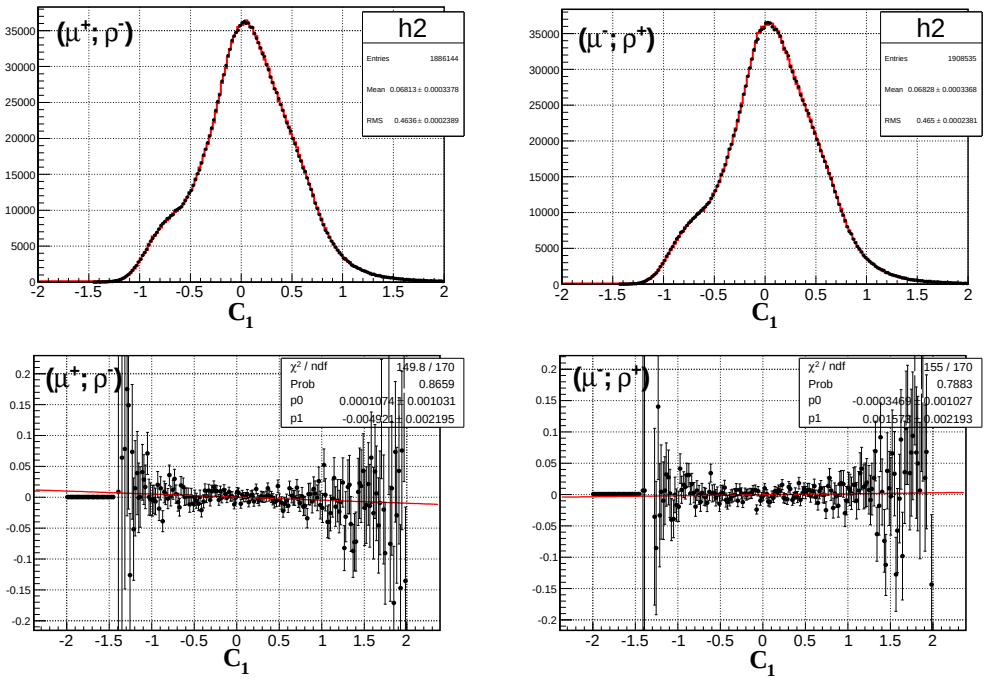

Figure 42: Distribution of $B_1^{(k)}$ for the $(\mu^+;\ \pi^-\pi^0)$ (upper left) and $(\mu^-;\ \pi^+\pi^0)$ (upper right) events (see Eq. 39, the mean value of this distribution gives normalisation coefficient $C_1 = (1/N_{\rm MC}) \cdot \sum\limits_{k=1}^{N_{\rm MC}} B_1^{(k)}$). Red histogram shows the distribution for the MC sample used to calculate normalisation coefficients ($C_1({\rm norm}) = 0.07206 \pm 0.00034$ for the $(\mu^+;\ \pi^-\pi^0)$ events, $C_1({\rm norm}) = 0.07075 \pm 0.00034$ for the $(\mu^-;\ \pi^+\pi^0)$ events), points with errors - for the MC sample used in the fit ($C_1({\rm fit}) = 0.07104 \pm 0.00034$ for the $(\mu^+;\ \pi^-\pi^0)$ events, $C_1({\rm fit}) = 0.07121 \pm 0.00034$ for the $(\mu^-;\ \pi^+\pi^0)$ events). Relative difference of the distributions for normalisation MC sample and for the fit MC sample is also shown for the $(\mu^+;\ \pi^-\pi^0)$ (lower left) and $(\mu^-;\ \pi^+\pi^0)$ (right) events. Red line shows the result of the fit by the first order polynomial function.

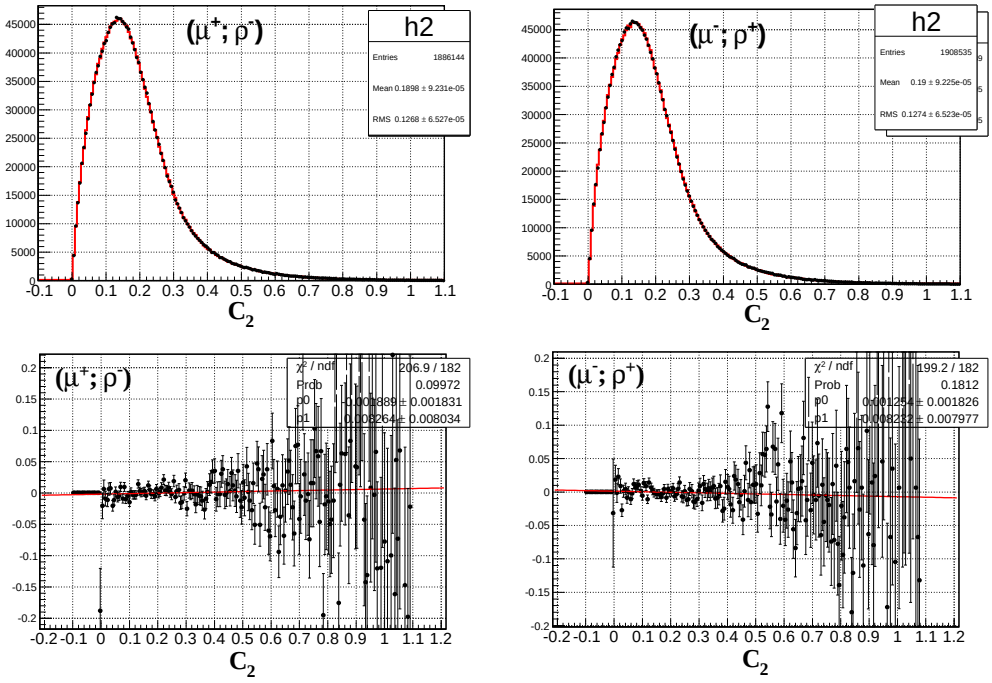

Figure 43: Distribution of $B_2^{(k)}$ for the $(\mu^+;\ \pi^-\pi^0)$ (upper left) and $(\mu^-;\ \pi^+\pi^0)$ (upper right) events (see Eq. 39, the mean value of this distribution gives normalisation coefficient $C_2 = (1/N_{\rm MC}) \cdot \sum_{k=1}^{N_{\rm MC}} B_2^{(k)}$). Red histogram shows the distribution for the MC sample used to calculate normalisation coefficients ($C_2({\rm norm}) = 0.18983 \pm 0.00009$ for the $(\mu^+;\ \pi^-\pi^0)$ events, $C_2({\rm norm}) = 0.19029 \pm 0.00009$ for the $(\mu^-;\ \pi^+\pi^0)$ events), points with errors - for the MC sample used in the fit ($C_2({\rm fit}) = 0.19007 \pm 0.00009$ for the $(\mu^+;\ \pi^-\pi^0)$ events, $C_2({\rm fit}) = 0.19027 \pm 0.00009$ for the $(\mu^-;\ \pi^+\pi^0)$ events). Relative difference of the distributions for normalisation MC sample and for the fit MC sample is also shown for the $(\mu^+;\ \pi^-\pi^0)$ (lower left) and $(\mu^-;\ \pi^+\pi^0)$ (right) events. Red line shows the result of the fit by the first order polynomial function.

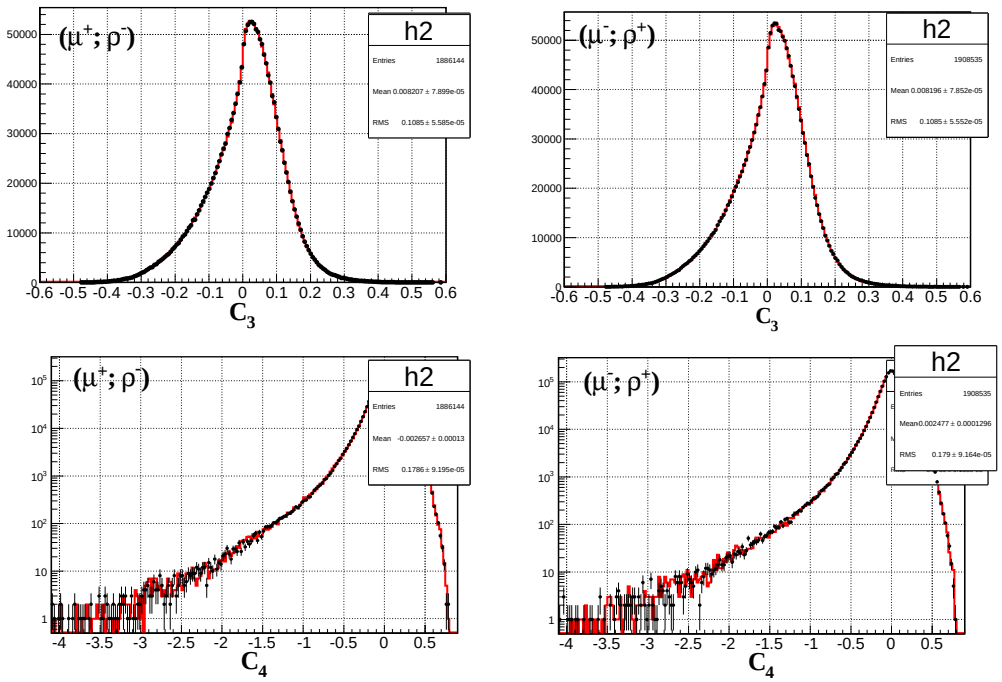

Figure 44: Distribution of $B_3^{(k)}$ for the $(\mu^+;\ \pi^-\pi^0)$ (upper left) and $(\mu^-;\ \pi^+\pi^0)$ (upper right) events (see Eq. 39, the mean value of this distribution gives normalisation coefficient $C_3 = (1/N_{\rm MC}) \cdot \sum_{k=1}^{N_{\rm MC}} B_3^{(k)}$). Distribution of $B_4^{(k)}$ for the $(\mu^+;\ \pi^-\pi^0)$ (lower left) and $(\mu^-;\ \pi^+\pi^0)$ (lower right) events. Red histogram shows the distribution for the MC sample used to calculate normalisation coefficients, points with errors - for the MC sample used in the fit. For the $(\mu^+;\ \pi^-\pi^0)$ events: $C_3({\rm norm}) = 0.00810 \pm 0.00008$, $C_3({\rm fit}) = 0.00821 \pm 0.00008$, $C_4({\rm norm}) = -0.00230 \pm 0.00013$, $C_4({\rm fit}) = -0.00269 \pm 0.00013$. For the $(\mu^-;\ \pi^+\pi^0)$ events: $C_3({\rm norm}) = 0.00805 \pm 0.00008$, $C_3({\rm fit}) = 0.00820 \pm 0.00008$, $C_4({\rm norm}) = -0.00222 \pm 0.00013$, $C_4({\rm fit}) = -0.00250 \pm 0.00013$.

function for this fit on the $\rho - \eta$ plane, large correlation between ρ and η Michel parameters is clearly seen. Figures 46-49 show the dependences of

Table 9: Result of the fit of 1 MC stream (4 MC streams were used for the normalization) for the $(\mu^{\pm};\ \pi^{\mp}\pi^0)$ events.

$(\mu^+;\ \pi^-\pi^0)$			$(\mu^-;\ \pi^+\pi^0)$		
ρ	=	0.7486 ± 0.0062	ρ	=	0.7523 ± 0.0062
η	=	-0.0139 ± 0.0233	η	=	0.0056 ± 0.0232
ξ	=	0.9915 ± 0.0117	ξ	=	1.0034 ± 0.0118
$\xi\delta$	=	0.7479 ± 0.0076	$\xi\delta$	=	0.7507 ± 0.0076

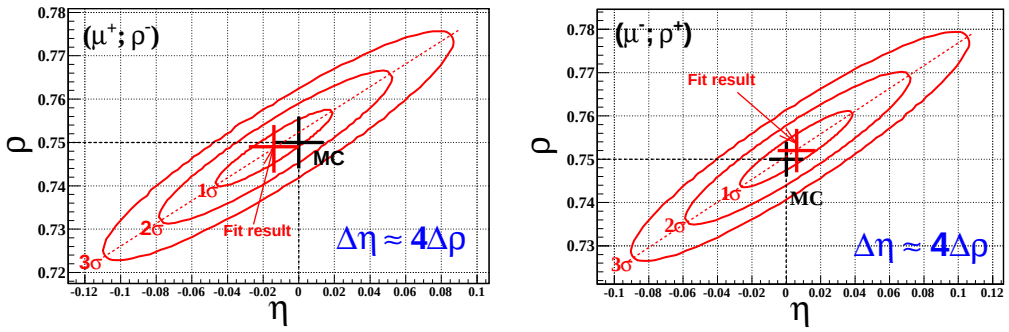

Figure 45: Result of the fit of 1 MC stream (4 MC streams were used for the normalization) on the $\rho - \eta$ plane for the $(\mu^{\pm};\ \pi^{\mp}\pi^0)$ events. Shown are 1σ-, 2σ- and 3σ-contours of the likelihood function.

the optimal values of Michel parameters on the serial number $(1 \div 5)$ of the fitted MC stream for the $(\mu^{\pm};\ \pi^{\mp}\pi^0)$ events. Clearly seen is reasonable statistical fluctuation of the fit results around SM values of Michel parameters.

We tested the validity of the PDF for the $(\ell^{\pm};\ \pi^{\mp}\pi^0\pi^0)$ $(\ell = e,\ \mu)$ events. Figures 52-55 show result of the fit of the generated $(\ell^{\pm};\ \pi^{\mp}\pi^0\pi^0)$ events, where one of the π^0 is not registered in the fiducial volume of the detector (one or both daughter photons of this π^0 are missed). The detected photon from the missed π^0 is considered as an extra photon, and we applied a cut on the total energy of the extra photons in the event ($E^{\rm LAB}_{\gamma\ {\rm extra}}$). To get final PDF full differential cross section (with effects of ISR) is numerically integrated on the parameters of the undetected π^0. It is seen that Michel

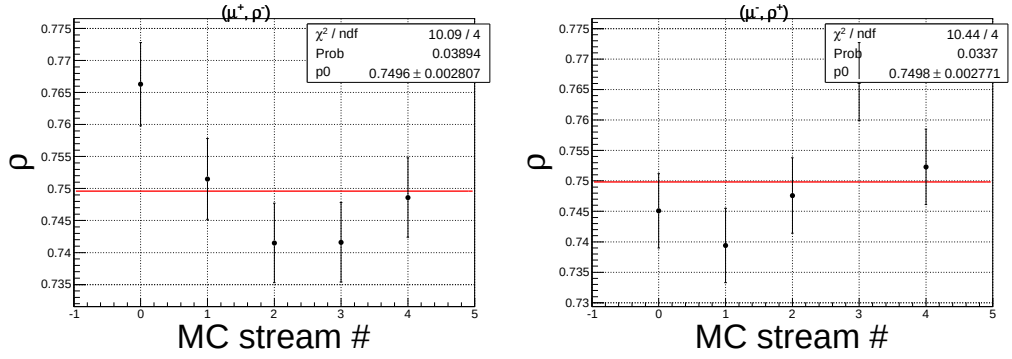

Figure 46: Optimal value of ρ Michel parameter as a function of the serial number of the fitted MC stream for the $(\mu^+;\ \pi^-\pi^0)$ (left) and $(\mu^-;\ \pi^+\pi^0)$ (right) events.

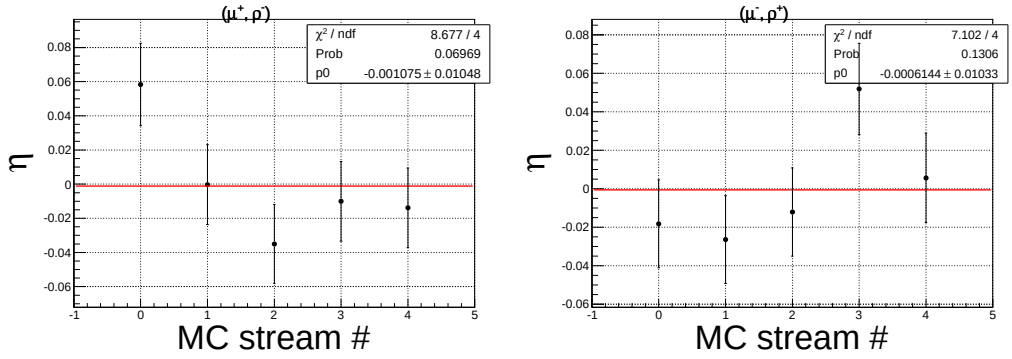

Figure 47: Optimal value of η Michel parameter as a function of the serial number of the fitted MC stream for the $(\mu^+;\ \pi^-\pi^0)$ (left) and $(\mu^-;\ \pi^+\pi^0)$ (right) events.

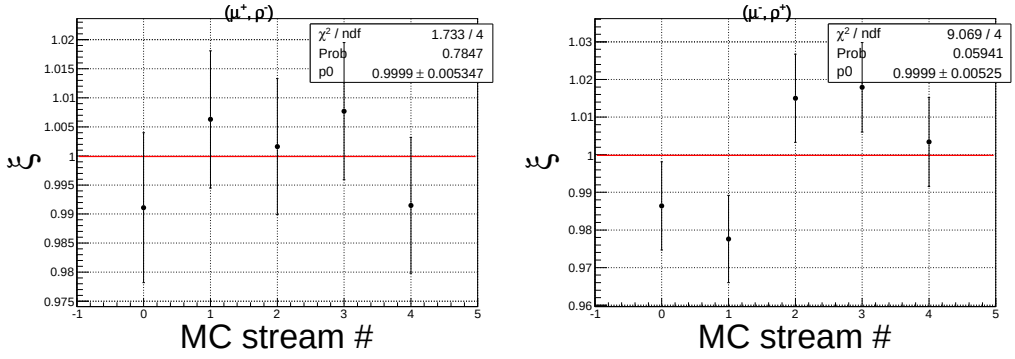

Figure 48: Optimal value of ξ Michel parameter as a function of the serial number of the fitted MC stream for the $(\mu^+;\ \pi^-\pi^0)$ (left) and $(\mu^-;\ \pi^+\pi^0)$ (right) events.

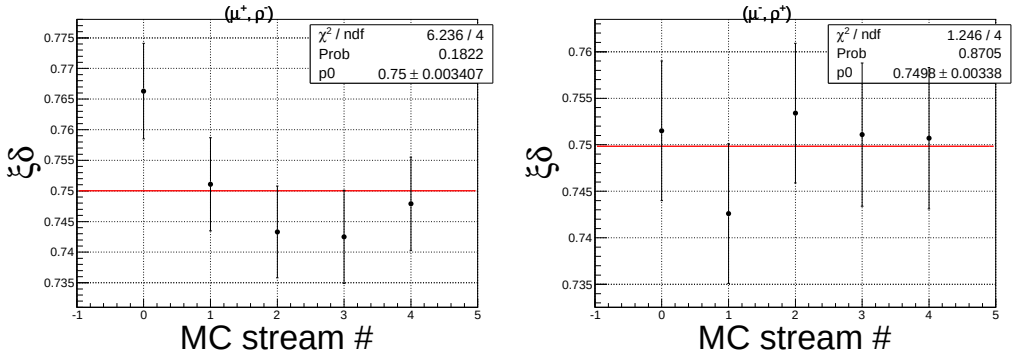

Figure 49: Optimal value of $\xi\delta$ Michel parameter as a function of the serial number of the fitted MC stream for the $(\mu^+;\ \pi^-\pi^0)$ (left) and $(\mu^-;\ \pi^+\pi^0)$ (right) events.

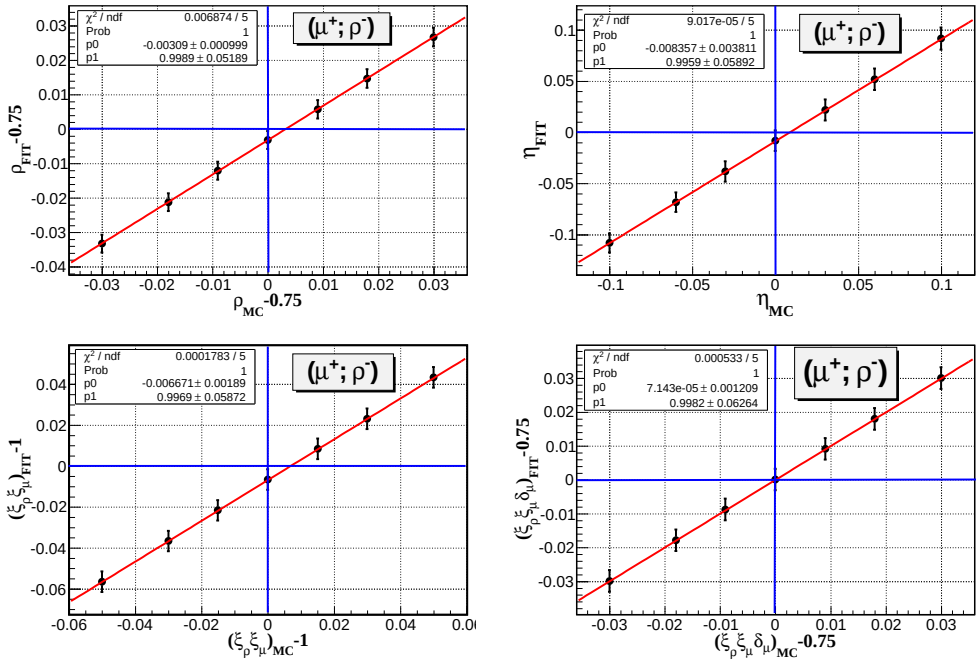

Figure 50: Study of the fitter bias for $(\mu^+;\ \pi^-\pi^0)$ events. Dependences of the fit results versus generator values are shown for Michel parameters (deviations from the SM values): $\rho-0.75$ and $\xi_\rho\xi-1$ (left), η and $\xi_\rho\xi\delta-0.75$ (right).

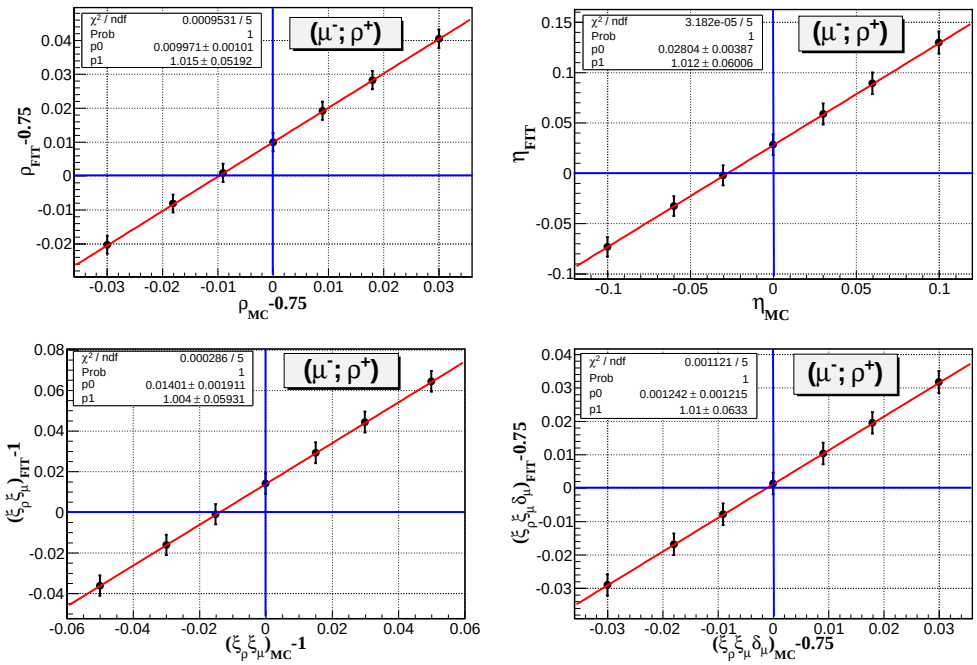

Figure 51: Study of the fitter bias for $(\mu^-;\ \pi^+\pi^0)$ events. Dependences of the fit results versus generator values are shown for Michel parameters (deviations from the SM values): $\rho - 0.75$ and $\xi_\rho\xi - 1$ (left), η and $\xi_\rho\xi\delta - 0.75$ (right).

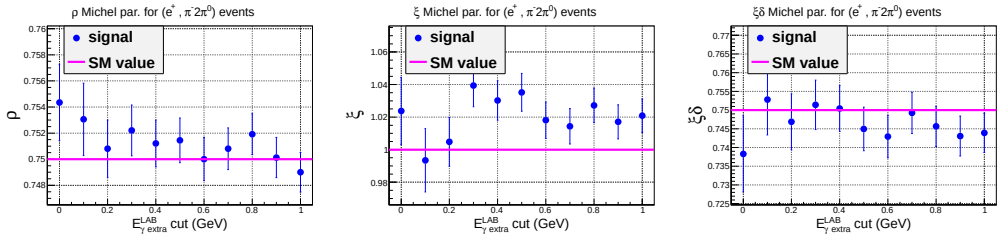

Figure 52: Result of the fit of the generated $(e^+;\ \pi^-\pi^0\pi^0)$ events as a function of the extra gamma energy $(E^{\rm LAB}_{\gamma\ \rm extra})$ cut.

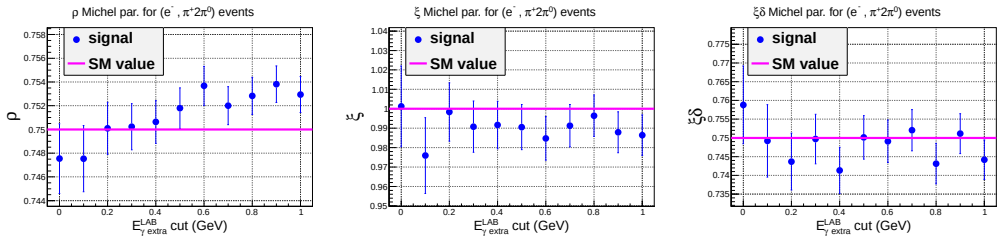

Figure 53: Result of the fit of the generated $(e^-;\ \pi^+\pi^0\pi^0)$ events as a function of the extra gamma energy $(E^{\mathrm{LAB}}_{\gamma\ \mathrm{extra}})$ cut.

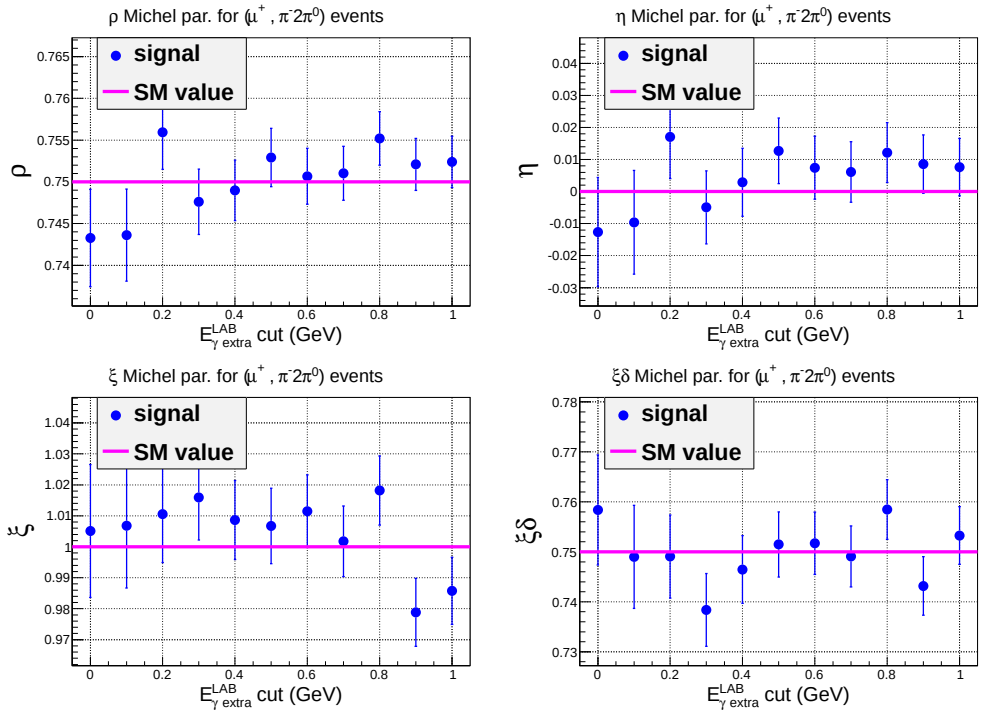

Figure 54: Result of the fit of the generated $(\mu^+;\ \pi^-\pi^0\pi^0)$ events as a function of the extra gamma energy $(E^{\mathrm{LAB}}_{\gamma\ \mathrm{extra}})$ cut.

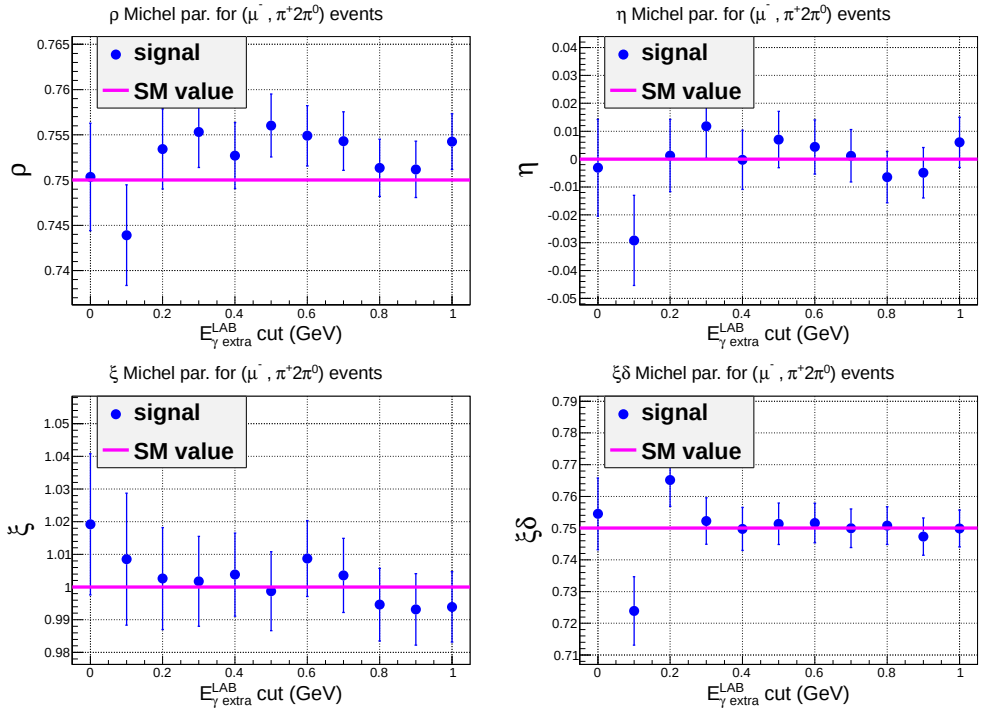

Figure 55: Result of the fit of the generated $(\mu^-;\ \pi^+\pi^0\pi^0)$ events as a function of the extra gamma energy $(E^{\rm LAB}_{\gamma\ {\rm extra}})$ cut.

parameters are reasonably reproduced in the wide range of the $E^{\rm LAB}_{\gamma\ {\rm extra}}$ cut values. In the next test we approximated $(\ell^{\pm};\ \pi^{\mp}\pi^0\pi^0)$ $(\ell = e,\ \mu)$ events passed through full MC simulation procedure and all selection criteria (except $E^{\rm LAB}_{\gamma\ {\rm extra}}$ cut), obtained results are shown in Fig. 56-59. Half of the selected sample was used to calculate normalization coefficients, and the remaining part was used in the fit. Again, to get the final PDF full differential cross section (with effects of ISR) is numerically integrated on the parameters of the undetected π^0, in this case the π^0 reconstruction inefficiency was taken from MC, see Fig. 21, 22. The statistics of MC $(\ell^{\pm};\ \pi^{\mp}\pi^0\pi^0)$ events

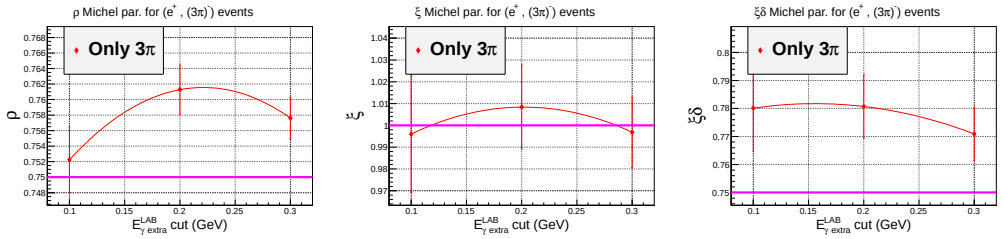

Figure 56: Result of the fit of the MC $(e^+;\ \pi^-\pi^0\pi^0)$ events as a function of the extra gamma energy $(E^{\rm LAB}_{\gamma\ {\rm extra}})$ cut.

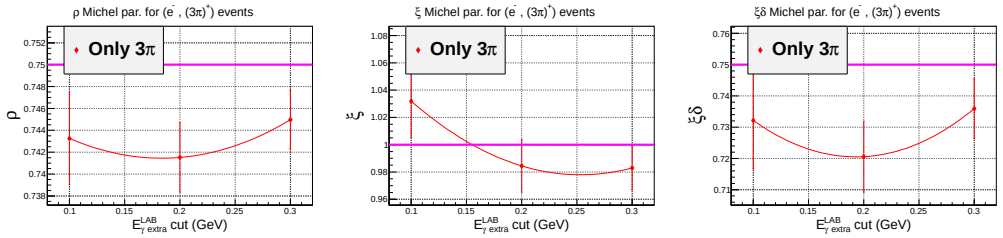

Figure 57: Result of the fit of the MC $(e^-;\ \pi^+\pi^0\pi^0)$ events as a function of the extra gamma energy $(E^{\rm LAB}_{\gamma\ {\rm extra}})$ cut.

was not enough to calculate normalization coefficients with high accuracy, so the systematic bias in Michel parameters seen in Fig. 56-59 is explained by statistical uncertainties in the normalization coefficients.

Then the validity of the fitter was tested with the combined MC samples:

- $(\ell^{\pm};\ \pi^{\mp}\pi^0) \oplus (\ell^{\pm};\ \pi^{\mp}\pi^0\pi^0)$ $(\ell = e,\ \mu)$;

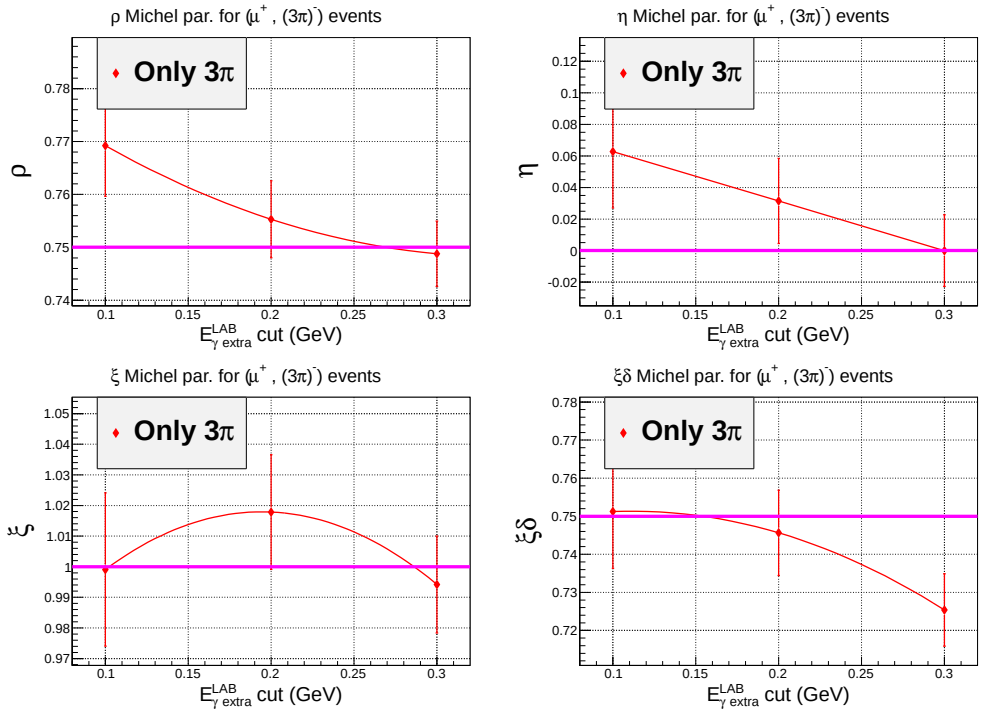

Figure 58: Result of the fit of the MC (μ^+; $\pi^-\pi^0\pi^0$) events as a function of the extra gamma energy ($E^{\rm LAB}_{\gamma\ {\rm extra}}$) cut.

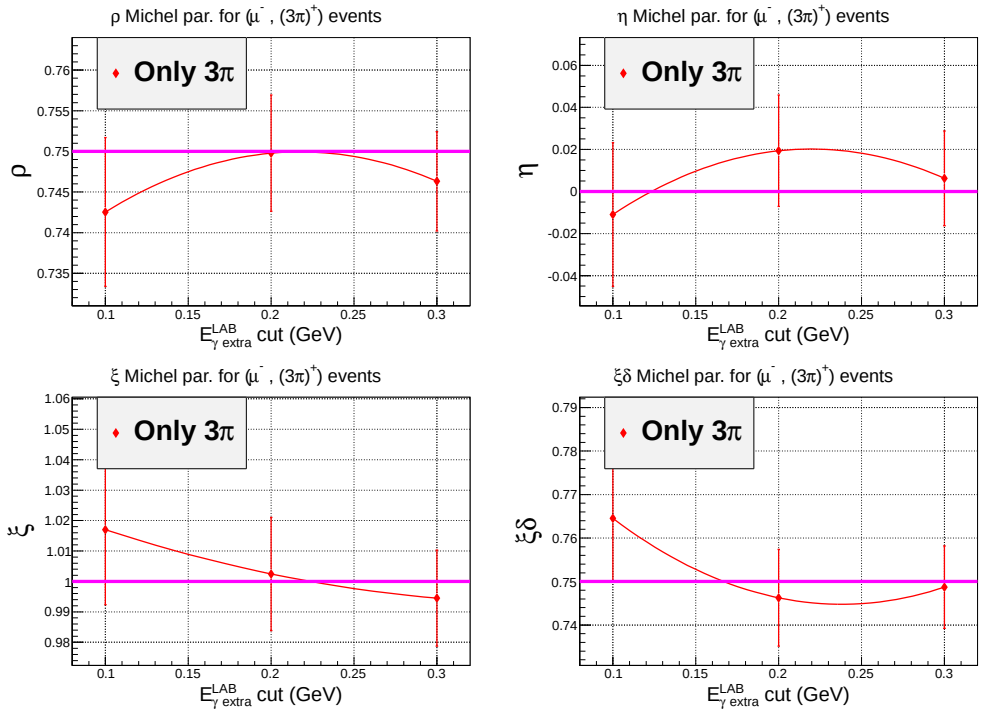

Figure 59: Result of the fit of the MC (μ^-; $\pi^+\pi^0\pi^0$) events as a function of the extra gamma energy ($E^{\rm LAB}_{\gamma\ {\rm extra}}$) cut.

- $(\mu^{\pm};\ \pi^{\mp}\pi^0) \oplus (\mu^{\pm};\ \pi^{\mp}\pi^0\pi^0) \oplus (\pi^{\pm};\ \pi^{\mp}\pi^0)$;
- whole MC sample (i.e.: $(\ell^{\pm};\ \pi^{\mp}\pi^0) \oplus (\ell^{\pm};\ \pi^{\mp}\pi^0\pi^0) \oplus (\pi^{\pm};\ \pi^{\mp}\pi^0)$(for $\ell = \mu$) $\oplus$ "other").

We performed the fits for the three different cuts on the extra γ energy in laboratory frame: $E^{\rm LAB}_{\gamma\ \rm rest} < 0.1,\ \mathbf{0.2},\ 0.3$ GeV. The $E^{\rm LAB}_{\gamma\ \rm rest} < 0.2$ GeV cut is considered to be the nominal one. In Table 10 we collect fit results of the $(e^{\pm};\ \pi^{\mp}\pi^0) \oplus (e^{\pm};\ \pi^{\mp}\pi^0\pi^0)$ and $(\mu^{\pm};\ \pi^{\mp}\pi^0) \oplus (\mu^{\pm};\ \pi^{\mp}\pi^0\pi^0) \oplus (\pi^{\pm};\ \pi^{\mp}\pi^0)$ MC samples (for the nominal $E^{\rm LAB}_{\gamma\ \rm rest}$ cut).

Table 10: Result of the fit of the $(e^{\pm};\ \pi^{\mp}\pi^0)\oplus(e^{\pm};\ \pi^{\mp}\pi^0\pi^0)$ and $(\mu^{\pm};\ \pi^{\mp}\pi^0)\oplus(\mu^{\pm};\ \pi^{\mp}\pi^0\pi^0) \oplus (\pi^{\pm};\ \pi^{\mp}\pi^0)$ MC samples.

$(e^+;\ \pi^-\pi^0)$				
ρ	=	0.7523	$\pm$	0.0010
η	=	0	-	fixed
ξ	=	0.9994	$\pm$	0.0043
$\xi\delta$	=	0.7535	$\pm$	0.0027

$(e^-;\ \pi^+\pi^0)$				
ρ	=	0.7485	$\pm$	0.0010
η	=	0	-	fixed
ξ	=	0.9973	$\pm$	0.0043
$\xi\delta$	=	0.7453	$\pm$	0.0027

$(\mu^+;\ \pi^-\pi^0)$				
ρ	=	0.7458	$\pm$	0.0021
η	=	-0.0164	$\pm$	0.0079
ξ	=	1.0030	$\pm$	0.0039
$\xi\delta$	=	0.7569	$\pm$	0.0026

$(\mu^-;\ \pi^+\pi^0)$				
ρ	=	0.7433	$\pm$	0.0021
η	=	-0.0121	$\pm$	0.0079
ξ	=	0.9912	$\pm$	0.0039
$\xi\delta$	=	0.7581	$\pm$	0.0026

Figures 60-64 show result of the fit of MC events, in the fit of all selected events the remaining background was described by the PDF tabulated as $\mathcal{P}_{\rm 6D}(p_\ell,\ \cos\theta_\ell,\ p_\rho,\ \cos\theta_\rho,\ m^2_{\pi\pi},\ \cos\tilde{\theta}_\pi) \cdot \mathcal{P}_{\rm 2D}(\varphi_\rho,\ \tilde{\varphi}_\pi) \cdot \mathcal{P}_{\rm 1D}(\Delta\varphi_{\ell\rho})$.

Figures 65-69 show result of the fit of MC events, in the fit of all selected events the remaining background was described by the PDF tabulated as $\mathcal{P}_{\rm 4D}(p_\ell,\ p_\rho,\ \omega,\ \cos\psi_{\ell\rho}) \cdot \mathcal{P}_{\rm 1D}(\varphi_\ell) \cdot \mathcal{P}_{\rm 1D}(\varphi_\rho) \cdot \mathcal{P}_{\rm 1D}(m^2_{\pi\pi}) \cdot \mathcal{P}_{\rm 1D}(\cos\tilde{\theta}_\pi) \cdot \mathcal{P}_{\rm 1D}(\tilde{\varphi}_\pi)$.

Notable bias of the ρ and η parameters seen in the 6D$\otimes$2D$\otimes$1D fit is explained by the coarse tabulation of the $\mathcal{P}_{\rm 6D}$ on the lepton momentum, p_ℓ. In the 4D$\otimes$1D[5] fit, ρ and η parameters are reproduced better as the size of the cell in the p_ℓ direction can be done several times smaller (i.e. ρ and η parameters are sensitive to the fine details of the p_ℓ distribution). However, the systematic bias of the ξ and $\xi\delta$ parameters is observed in both cases. It remains in the fits regardless the scheme to describe the remaining background we use, see Sect. 4.4. Even if we use the scheme where all 2D

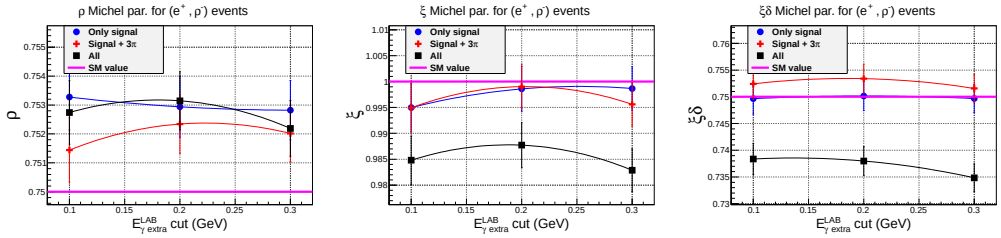

Figure 60: 6D⊗2D⊗1D scheme: optimal values of Michel parameters, ρ (left), ξ (middle), $\xi\delta$ (right), from the fit of the selected $(e^+;\ \pi^-\pi^0)$ MC events as a function of the extra gamma energy ($E^{\rm LAB}_{\gamma\ \rm extra}$) cut. Separately shown are: the fit of only signal events (blue filled circles), the fit of the $(e^+;\ \pi^-\pi^0) \oplus (e^+;\ \pi^-\pi^0\pi^0)$ events (red crosses), the fit of all selected events (black filled squares). Magenta line shows the SM expectation for the corresponding Michel parameter.

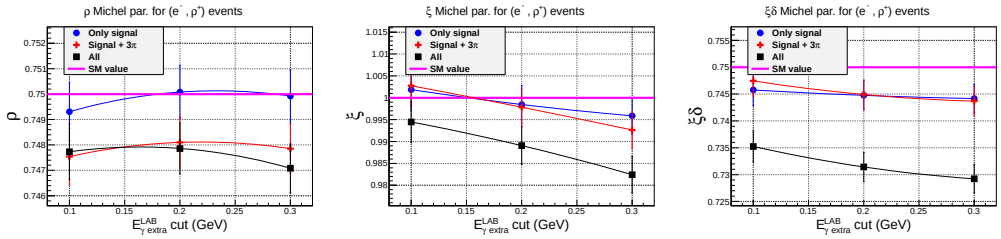

Figure 61: 6D⊗2D⊗1D scheme: optimal values of Michel parameters, ρ (left), ξ (middle), $\xi\delta$ (right), from the fit of the selected $(e^-;\ \pi^+\pi^0)$ MC events as a function of the extra gamma energy ($E^{\rm LAB}_{\gamma\ \rm extra}$) cut. Separately shown are: the fit of only signal events (blue filled circles), the fit of the $(e^-;\ \pi^+\pi^0) \oplus (e^-;\ \pi^+\pi^0\pi^0)$ events (red crosses), the fit of all selected events (black filled squares). Magenta line shows the SM expectation for the corresponding Michel parameter.

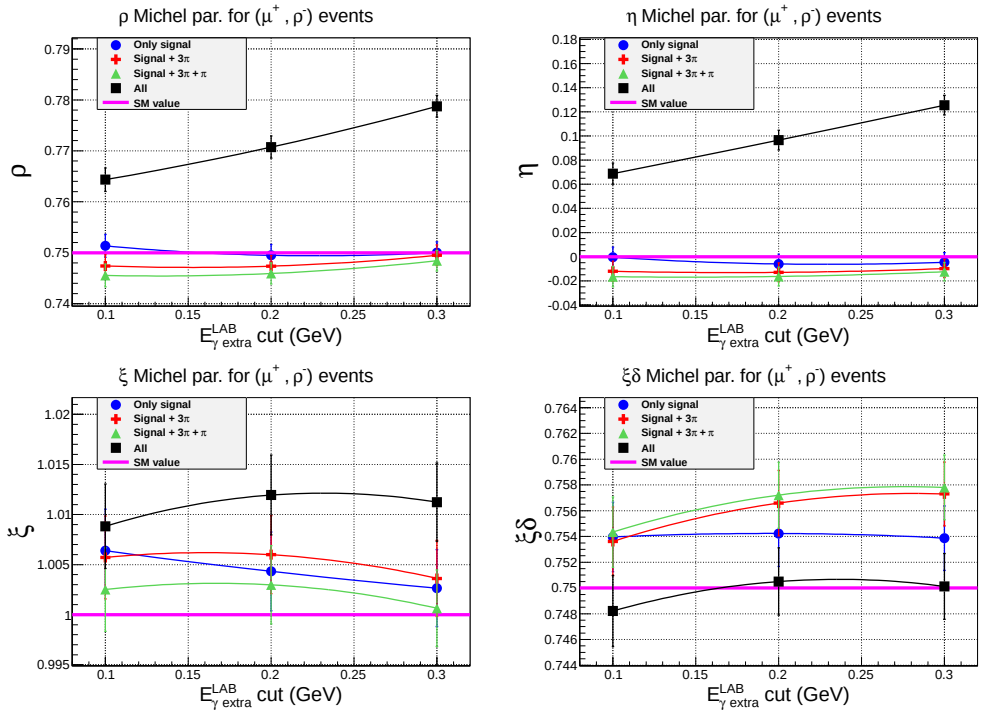

Figure 62: 6D⊗2D⊗1D scheme: optimal values of Michel parameters, ρ (upper left), η (upper right), ξ (lower left), $\xi\delta$ (lower right), from the fit of the selected $(\mu^+;\ \pi^-\pi^0)$ MC events as a function of the extra gamma energy ($E^{\rm LAB}_{\gamma\ {\rm extra}}$) cut. Separately shown are: the fit of only signal events (blue filled circles), the fit of the $(\mu^+;\ \pi^-\pi^0) \oplus (\mu^+;\ \pi^-\pi^0\pi^0)$ events (red crosses), the fit of the $(\mu^+;\ \pi^-\pi^0) \oplus (\mu^+;\ \pi^-\pi^0\pi^0) \oplus (\pi^+;\ \pi^-\pi^0)$ (green filled triangles), the fit of all selected events (black filled squares). Magenta line shows the SM expectation for the corresponding Michel parameter.

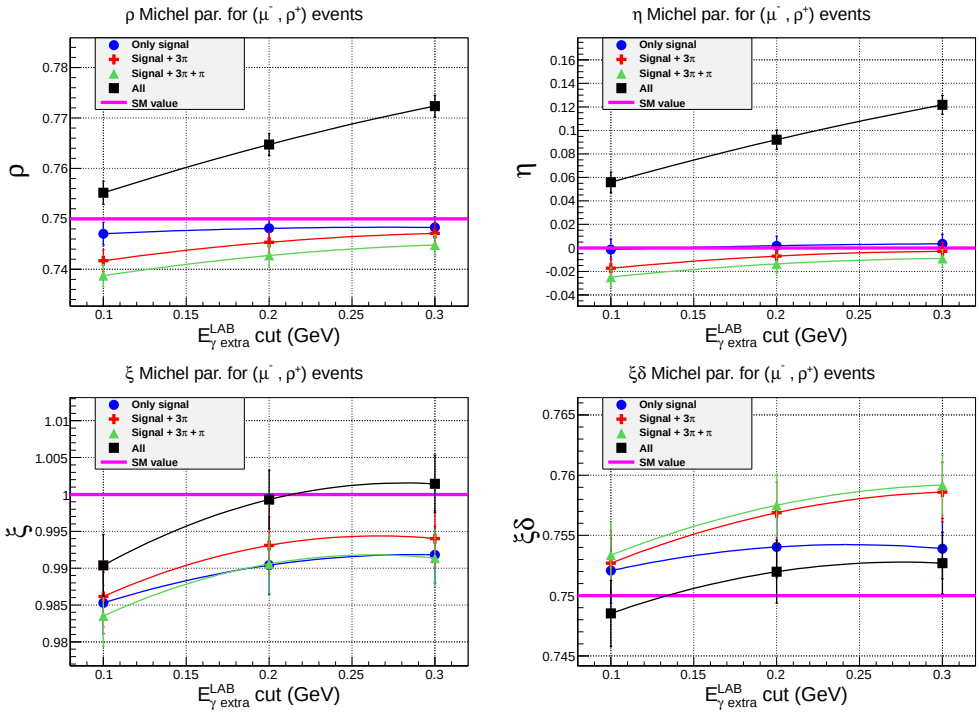

Figure 63: 6D⊗2D⊗1D scheme: optimal values of Michel parameters, ρ (upper left), η (upper right), ξ (lower left), $\xi\delta$ (lower right), from the fit of the selected $(\mu^-;\ \pi^+\pi^0)$ MC events as a function of the extra gamma energy ($E^{\rm LAB}_{\gamma\ {\rm extra}}$) cut. Separately shown are: the fit of only signal events (blue filled circles), the fit of the $(\mu^-;\ \pi^+\pi^0) \oplus (\mu^-;\ \pi^+\pi^0\pi^0)$ events (red crosses), the fit of the $(\mu^-;\ \pi^+\pi^0) \oplus (\mu^-;\ \pi^+\pi^0\pi^0) \oplus (\pi^-;\ \pi^+\pi^0)$ (green filled triangles), the fit of all selected events (black filled squares). Magenta line shows the SM expectation for the corresponding Michel parameter.

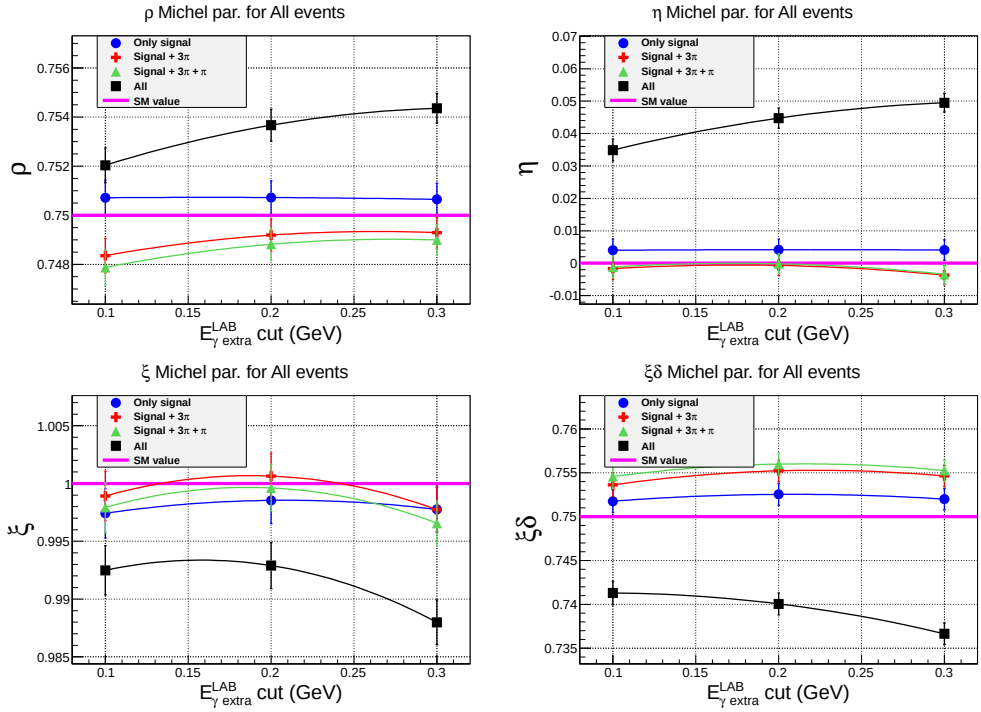

Figure 64: 6D⊗2D⊗1D scheme: optimal values of Michel parameters, ρ (upper left), η (upper right), ξ (lower left), $\xi\delta$ (lower right), from the **simultaneous fit** of the selected $(e^{\pm};\ \pi^{\mp}\pi^0)$ and $(\mu^{\pm};\ \pi^{\mp}\pi^0)$ MC events as a function of the extra gamma energy ($E^{\rm LAB}_{\gamma\ \rm extra}$) cut. Separately shown are: the fit of only signal events (blue filled circles), the fit of the $(\mu^-;\ \pi^+\pi^0) \oplus (\mu^-;\ \pi^+\pi^0\pi^0)$ events (red crosses), the fit of the $(\mu^-;\ \pi^+\pi^0) \oplus (\mu^-;\ \pi^+\pi^0\pi^0) \oplus (\pi^-;\ \pi^+\pi^0)$ (green filled triangles), the fit of all selected events (black filled squares). Magenta line shows the SM expectation for the corresponding Michel parameter.

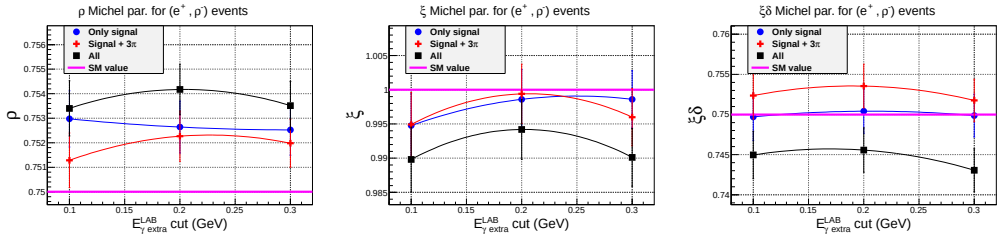

Figure 65: 4D⊗1D[5] scheme: optimal values of Michel parameters, ρ (left), ξ (middle), $\xi\delta$ (right), from the fit of the selected $(e^+;\ \pi^-\pi^0)$ MC events as a function of the extra gamma energy ($E^{\rm LAB}_{\gamma\ {\rm extra}}$) cut. Separately shown are: the fit of only signal events (blue filled circles), the fit of the $(e^+;\ \pi^-\pi^0) \oplus (e^+;\ \pi^-\pi^0\pi^0)$ events (red crosses), the fit of all selected events (black filled squares). Magenta line shows the SM expectation for the corresponding Michel parameter.

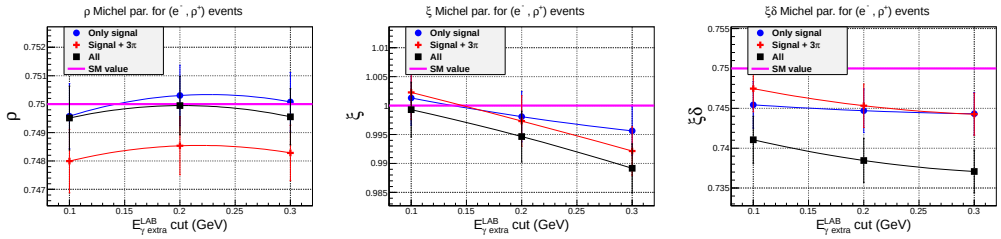

Figure 66: 4D⊗1D[5] scheme: optimal values of Michel parameters, ρ (left), ξ (middle), $\xi\delta$ (right), from the fit of the selected $(e^-;\ \pi^+\pi^0)$ MC events as a function of the extra gamma energy ($E^{\rm LAB}_{\gamma\ {\rm extra}}$) cut. Separately shown are: the fit of only signal events (blue filled circles), the fit of the $(e^-;\ \pi^+\pi^0) \oplus (e^-;\ \pi^+\pi^0\pi^0)$ events (red crosses), the fit of all selected events (black filled squares). Magenta line shows the SM expectation for the corresponding Michel parameter.

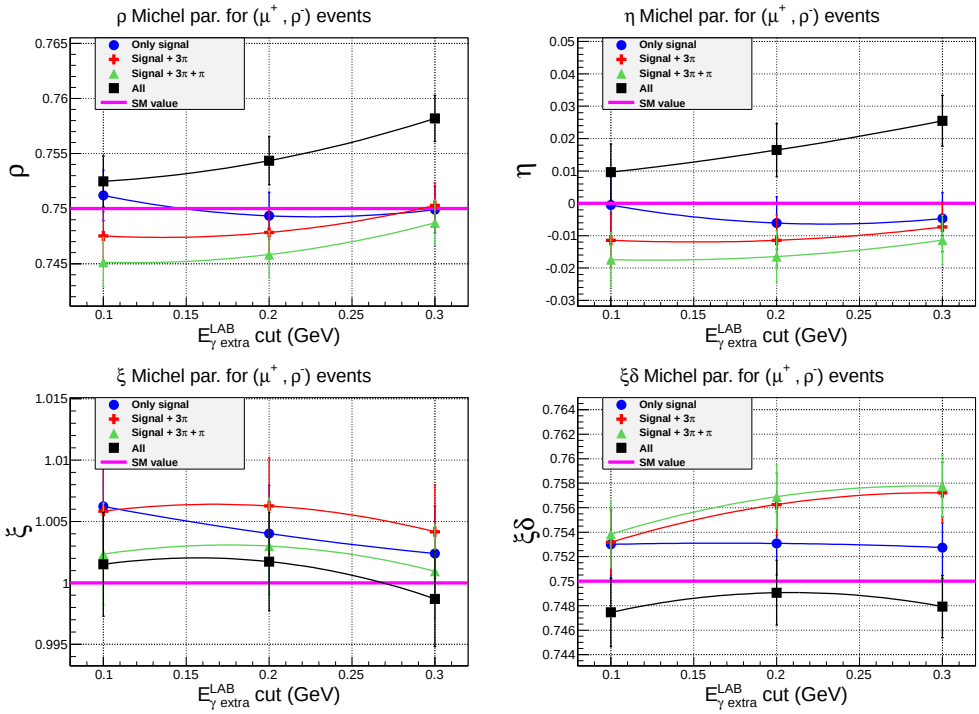

Figure 67: 4D⊗1D[5] scheme: optimal values of Michel parameters, ρ (upper left), η (upper right), ξ (lower left), $\xi\delta$ (lower right), from the fit of the selected $(\mu^+;\ \pi^-\pi^0)$ MC events as a function of the extra gamma energy ($E^{\rm LAB}_{\gamma\ {\rm extra}}$) cut. Separately shown are: the fit of only signal events (blue filled circles), the fit of the $(\mu^+;\ \pi^-\pi^0) \oplus (\mu^+;\ \pi^-\pi^0\pi^0)$ events (red crosses), the fit of the $(\mu^+;\ \pi^-\pi^0) \oplus (\mu^+;\ \pi^-\pi^0\pi^0) \oplus (\pi^+;\ \pi^-\pi^0)$ (green filled triangles), the fit of all selected events (black filled squares). Magenta line shows the SM expectation for the corresponding Michel parameter.

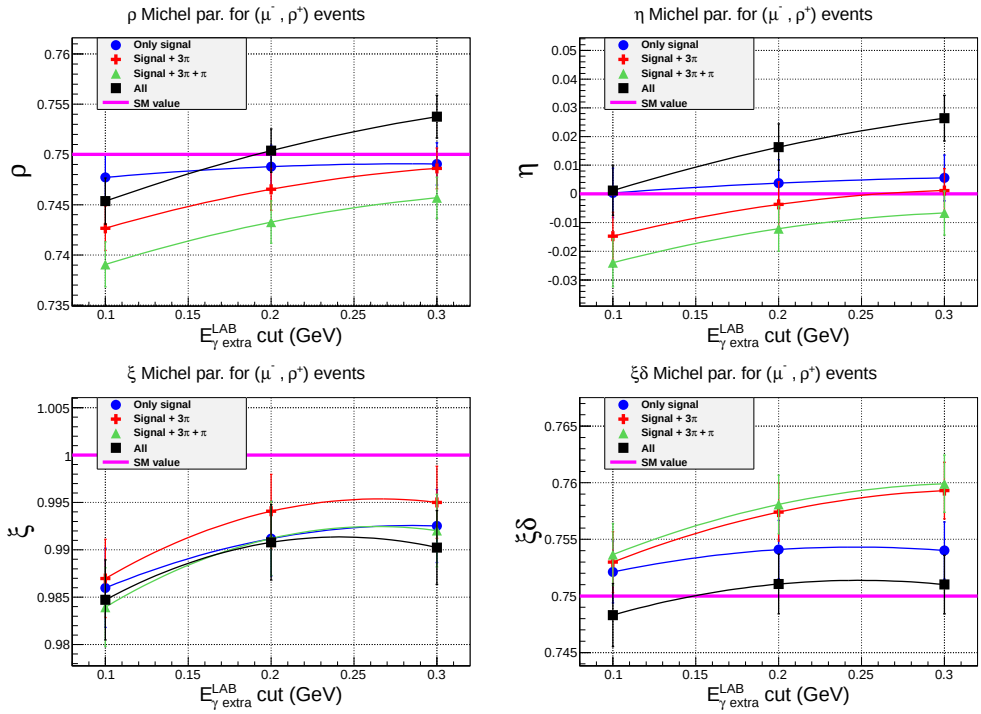

Figure 68: 4D⊗1D[5] scheme: optimal values of Michel parameters, ρ (upper left), η (upper right), ξ (lower left), $\xi\delta$ (lower right), from the fit of the selected $(\mu^-;\ \pi^+\pi^0)$ MC events as a function of the extra gamma energy ($E^{\rm LAB}_{\gamma\ {\rm extra}}$) cut. Separately shown are: the fit of only signal events (blue filled circles), the fit of the $(\mu^-;\ \pi^+\pi^0) \oplus (\mu^-;\ \pi^+\pi^0\pi^0)$ events (red crosses), the fit of the $(\mu^-;\ \pi^+\pi^0) \oplus (\mu^-;\ \pi^+\pi^0\pi^0) \oplus (\pi^-;\ \pi^+\pi^0)$ (green filled triangles), the fit of all selected events (black filled squares). Magenta line shows the SM expectation for the corresponding Michel parameter.

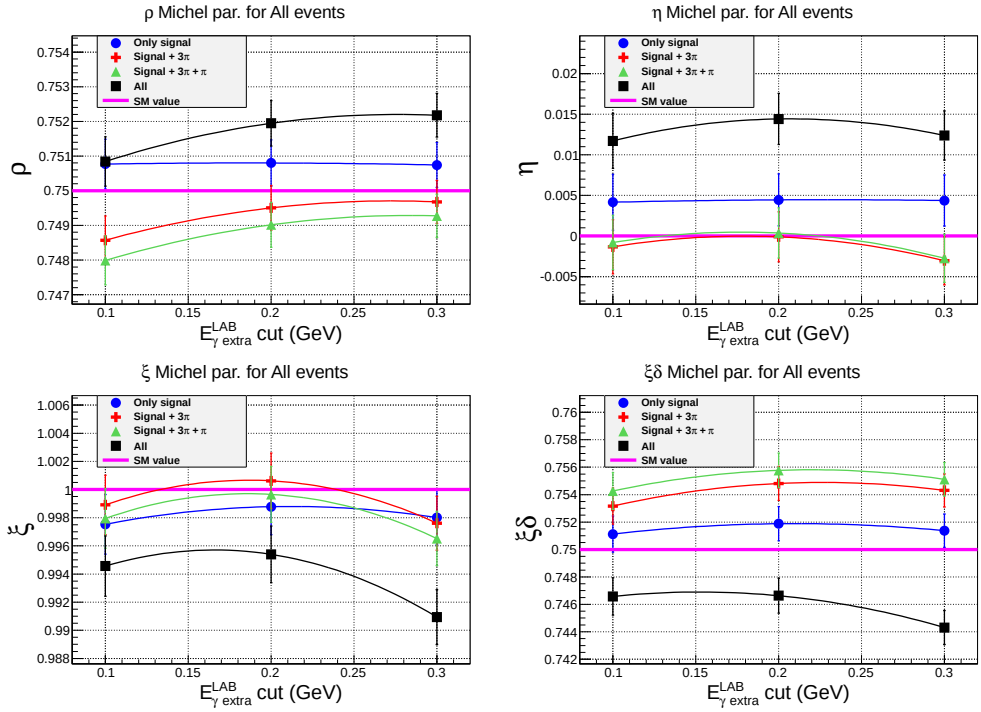

Figure 69: 4D⊗1D[5] scheme: optimal values of Michel parameters, ρ (upper left), η (upper right), ξ (lower left), $\xi\delta$ (lower right), from the **simultaneous fit** of the selected $(e^{\pm};\ \pi^{\mp}\pi^0)$ and $(\mu^{\pm};\ \pi^{\mp}\pi^0)$ MC events as a function of the extra gamma energy ($E^{\rm LAB}_{\gamma\ \rm extra}$) cut. Separately shown are: the fit of only signal events (blue filled circles), the fit of the $(\mu^-;\ \pi^+\pi^0)\oplus(\mu^-;\ \pi^+\pi^0\pi^0)$ events (red crosses), the fit of the $(\mu^-;\ \pi^+\pi^0)\oplus(\mu^-;\ \pi^+\pi^0\pi^0)\oplus(\pi^-;\ \pi^+\pi^0)$ (green filled triangles), the fit of all selected events (black filled squares). Magenta line shows the SM expectation for the corresponding Michel parameter.

correlations for the remaining background are tabulated with good accuracy, like $\mathcal{P}_{3D}(p_\ell,\ \cos\psi_{\ell\rho},\ p_\rho)\cdot\mathcal{P}_{2D}(\varphi_\rho,\ \tilde{\varphi}_\pi)\cdot\frac{\mathcal{P}_{2D}(p_\ell,\ \cos\theta_\rho)}{\mathcal{P}_{1D}(p_\ell)}\cdot\frac{\mathcal{P}_{2D}(p_\rho,\ \cos\tilde{\theta_\pi})}{\mathcal{P}_{1D}(p_\rho)}\cdot\frac{\mathcal{P}_{2D}(p_\rho,\ m^2_{\pi\pi})}{\mathcal{P}_{1D}(p_\rho)}\cdot\frac{\mathcal{P}_{2D}(\cos\psi_{\ell\rho},\ \Delta\varphi_{\ell\rho})}{\mathcal{P}_{1D}(\cos\psi_{\ell\rho})}$ scheme, nevertheless the bias of the ξ and $\xi\delta$ parameters is still observed, see Fig. 70-74. This represents one of the main sources of the systematic uncertainties in the ξ and $\xi\delta$ Michel parameters.

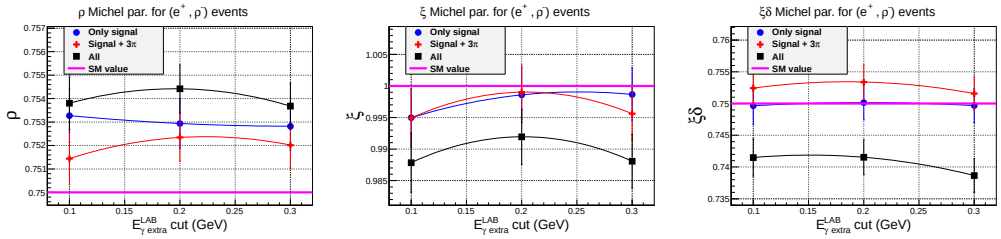

Figure 70: 3D$\otimes$2D^5/1D^4 scheme: optimal values of Michel parameters, ρ (left), ξ (middle), $\xi\delta$ (right), from the fit of the selected $(e^+;\ \pi^-\pi^0)$ MC events as a function of the extra gamma energy ($E^{\rm LAB}_{\gamma\ \rm extra}$) cut. Separately shown are: the fit of only signal events (blue filled circles), the fit of the $(e^+;\ \pi^-\pi^0)\oplus(e^+;\ \pi^-\pi^0\pi^0)$ events (red crosses), the fit of all selected events (black filled squares). Magenta line shows the SM expectation for the corresponding Michel parameter.

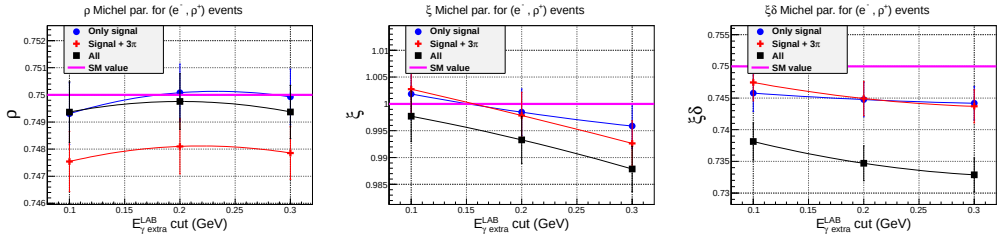

Figure 71: 3D$\otimes$2D^5/1D^4 scheme: optimal values of Michel parameters, ρ (left), ξ (middle), $\xi\delta$ (right), from the fit of the selected $(e^-;\ \pi^+\pi^0)$ MC events as a function of the extra gamma energy ($E^{\rm LAB}_{\gamma\ {\rm extra}}$) cut. Separately shown are: the fit of only signal events (blue filled circles), the fit of the $(e^-;\ \pi^+\pi^0) \oplus (e^-;\ \pi^+\pi^0\pi^0)$ events (red crosses), the fit of all selected events (black filled squares). Magenta line shows the SM expectation for the corresponding Michel parameter.

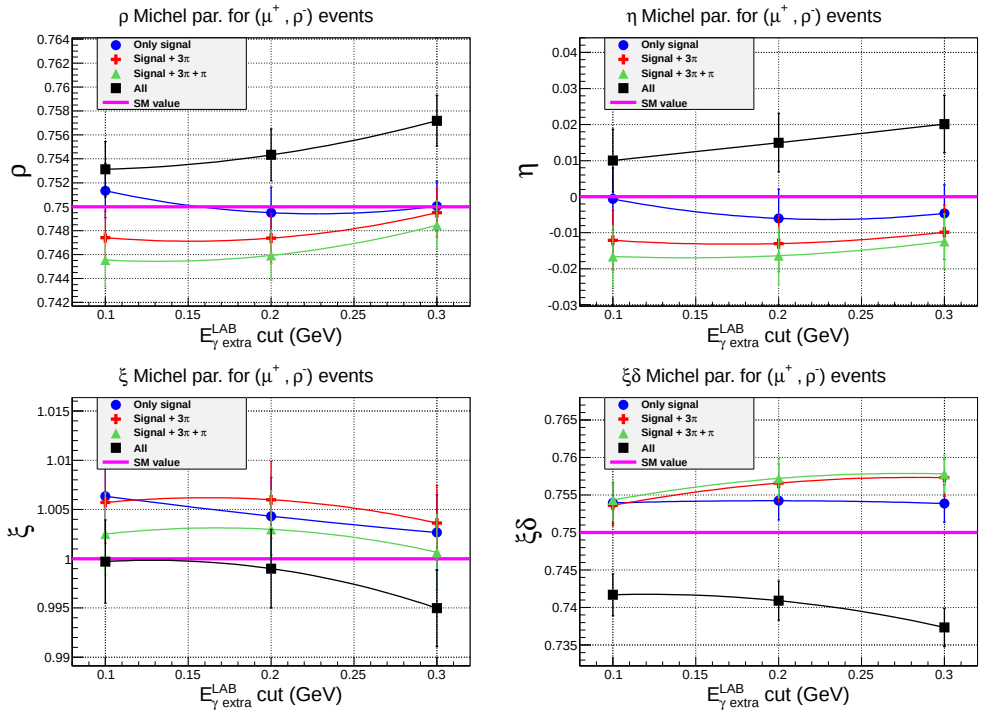

Figure 72: 3D⊗2D^5/1D^4 scheme: optimal values of Michel parameters, ρ (upper left), η (upper right), ξ (lower left), $\xi\delta$ (lower right), from the fit of the selected $(\mu^+;\ \pi^-\pi^0)$ MC events as a function of the extra gamma energy ($E^{\rm LAB}_{\gamma\ {\rm extra}}$) cut. Separately shown are: the fit of only signal events (blue filled circles), the fit of the $(\mu^+;\ \pi^-\pi^0) \oplus (\mu^+;\ \pi^-\pi^0\pi^0)$ events (red crosses), the fit of the $(\mu^+;\ \pi^-\pi^0) \oplus (\mu^+;\ \pi^-\pi^0\pi^0) \oplus (\pi^+;\ \pi^-\pi^0)$ (green filled triangles), the fit of all selected events (black filled squares). Magenta line shows the SM expectation for the corresponding Michel parameter.

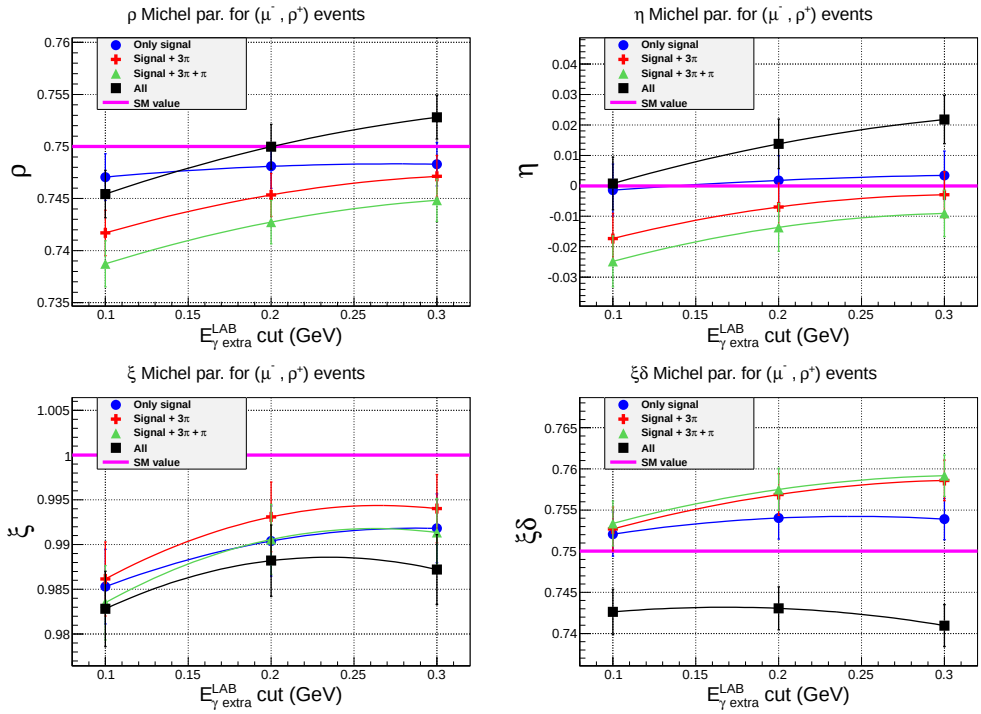

Figure 73: 3D⊗2D^5/1D^4 scheme: optimal values of Michel parameters, ρ (upper left), η (upper right), ξ (lower left), $\xi\delta$ (lower right), from the fit of the selected $(\mu^-;\ \pi^+\pi^0)$ MC events as a function of the extra gamma energy ($E^{\rm LAB}_{\gamma\ {\rm extra}}$) cut. Separately shown are: the fit of only signal events (blue filled circles), the fit of the $(\mu^-;\ \pi^+\pi^0) \oplus (\mu^-;\ \pi^+\pi^0\pi^0)$ events (red crosses), the fit of the $(\mu^-;\ \pi^+\pi^0) \oplus (\mu^-;\ \pi^+\pi^0\pi^0) \oplus (\pi^-;\ \pi^+\pi^0)$ (green filled triangles), the fit of all selected events (black filled squares). Magenta line shows the SM expectation for the corresponding Michel parameter.

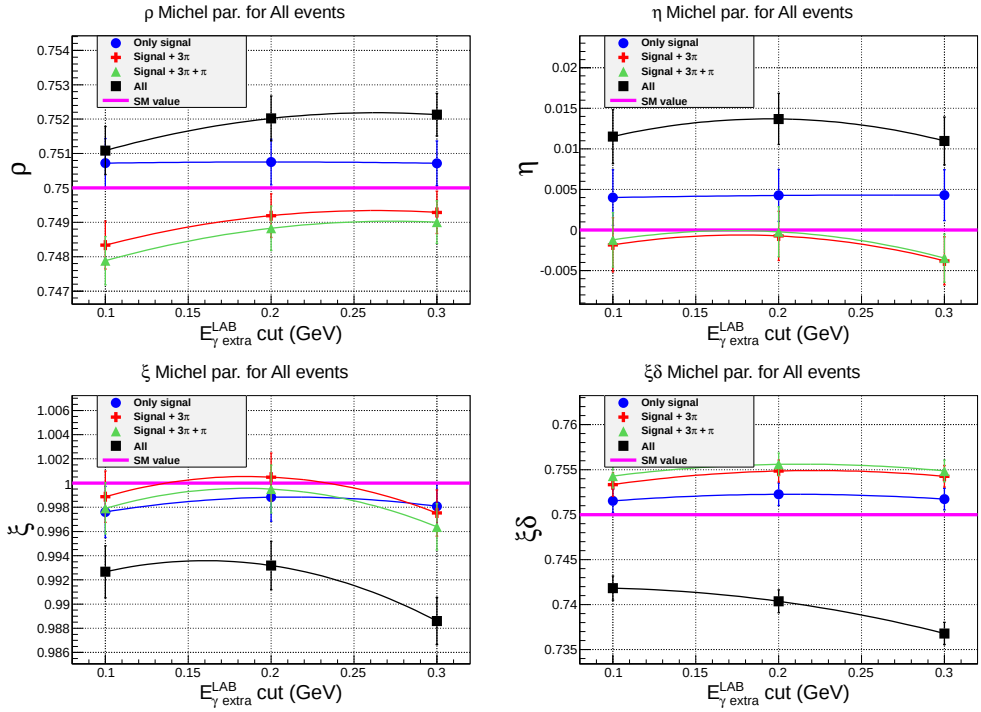

Figure 74: 3D⊗2D^5/1D^4 scheme: optimal values of Michel parameters, ρ (upper left), η (upper right), ξ (lower left), $\xi\delta$ (lower right), from the **simultaneous fit** of the selected $(e^{\pm};\ \pi^{\mp}\pi^0)$ and $(\mu^{\pm};\ \pi^{\mp}\pi^0)$ MC events as a function of the extra gamma energy ($E^{\rm LAB}_{\gamma\ \rm extra}$) cut. Separately shown are: the fit of only signal events (blue filled circles), the fit of the $(\mu^-;\ \pi^+\pi^0) \oplus (\mu^-;\ \pi^+\pi^0\pi^0)$ events (red crosses), the fit of the $(\mu^-;\ \pi^+\pi^0) \oplus (\mu^-;\ \pi^+\pi^0\pi^0) \oplus (\pi^-;\ \pi^+\pi^0)$ (green filled triangles), the fit of all selected events (black filled squares). Magenta line shows the SM expectation for the corresponding Michel parameter.

6 Analysis of experimental data

For the analysis we use an experimental data sample of $\int Ldt = 485$ fb^{-1} collected at the $\Upsilon(4S)$ resonance, which corresponds to $N_{\tau\tau} = 446 \times 10^6$. "caseA" statistics of experiments $7 \div 27$, $39 \div 55$ is used, experiments $31 \div 37$ were excluded because of the lack of the trigger information (Mdst_trg table) for these data. After all selections described in Section 3 and special requirements on Belle GDL output trigger bits, described in this Section later, about 5.5 million events of all four configurations ($(e^+;\pi^-\pi^0)$, $(e^-;\pi^+\pi^0)$, $(\mu^+;\pi^-\pi^0)$, $(\mu^-;\pi^+\pi^0)$) were selected for the fit.

In Fig. 75,75,76, 77,78 distributions of the main kinematical parameters are shown for $(e;\pi\pi^0)$ events. Fig. 80 shows the distributions of μ momentum and energy of ρ candidate for $(\mu;\pi\pi^0)$ events. From Fig. 77 it is clearly seen that the experimental electron momentum spectrum in comparison with MC one is notably shifted to higher momenta. This effect is explained by strong nonuniformity of the trigger efficiency as a function of electron momentum for $(e;\pi\pi^0)$ events, which is not properly reproduced by MC simulation. Some disagreement between experiment and MC can be also observed for muon momentum spectrum, see Fig. 80. Besides the effect of the trigger efficiency there is also effect of the lepton identification efficiency experiment/MC correction, which should be taken into account. In general, of particular importance are efficiency corrections to the lepton parameters, influence of the experiment/MC corrections to the ρ meson parameters on Michel parameters is expected to be notably smaller.

6.1 Trigger efficiency corrections

Fig. 81 and 82 show MC trigger efficiency as a function of lepton momentum for $(e^+,\ \rho^-)$ and $(\mu^+,\ \rho^-)$ events respectively. For the $(e^+,\ \rho^-)$ case quite strong dependence is seen, trigger efficiency varies from $\sim$100% at small momenta down to $\sim$70% at high momenta. Fig. 83,84 show the comparison of the MC and experimental distributions of GDL output trigger bits for the SVD-1 and SVD-2 $(e^+;\ \rho^-)$ data samples. And Fig. 85,86 - for the SVD-1 and SVD-2 $(\mu^+;\ \rho^-)$ data samples. It is clearly seen that MC simulation does not reproduce correctly relative frequencies of different trigger bits. If the efficiency is high (close to 100%) such a disagreement does not cause large difference between experimental and MC trigger efficiencies. But if the efficiency essentially differs from 100% (like for $(e,\ \rho)$ events) the experi-

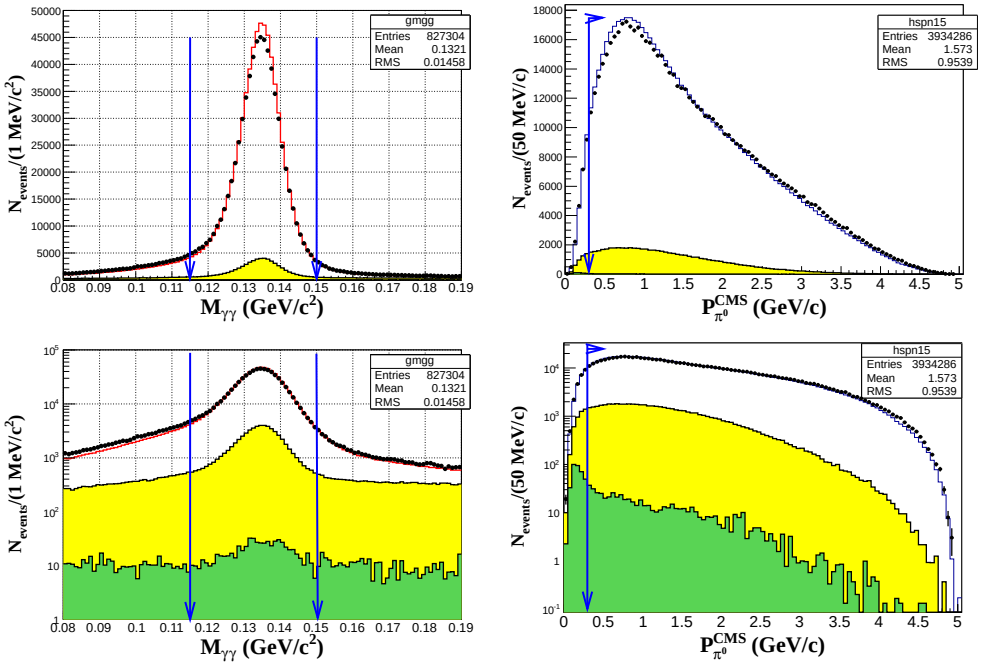

Figure 75: $\gamma\gamma$ invariant mass (left) and absolute momentum in CMS (right) of the π^0 candidate in $(e^+;\pi^-\pi^0)$ events. Upper figures are shown in normal (linear) vertical scale, lower figures – in logarithmic scale. Open histograms - full MC simulation, yellow shaded histograms - the main background components from $(e^+;\pi^-\pi^0\pi^0)$ events, green shaded histograms - the remaining background, points with errors - experimental data. MC and experimental histograms are normalized to the same number of events. Blue arrows show applied selections.

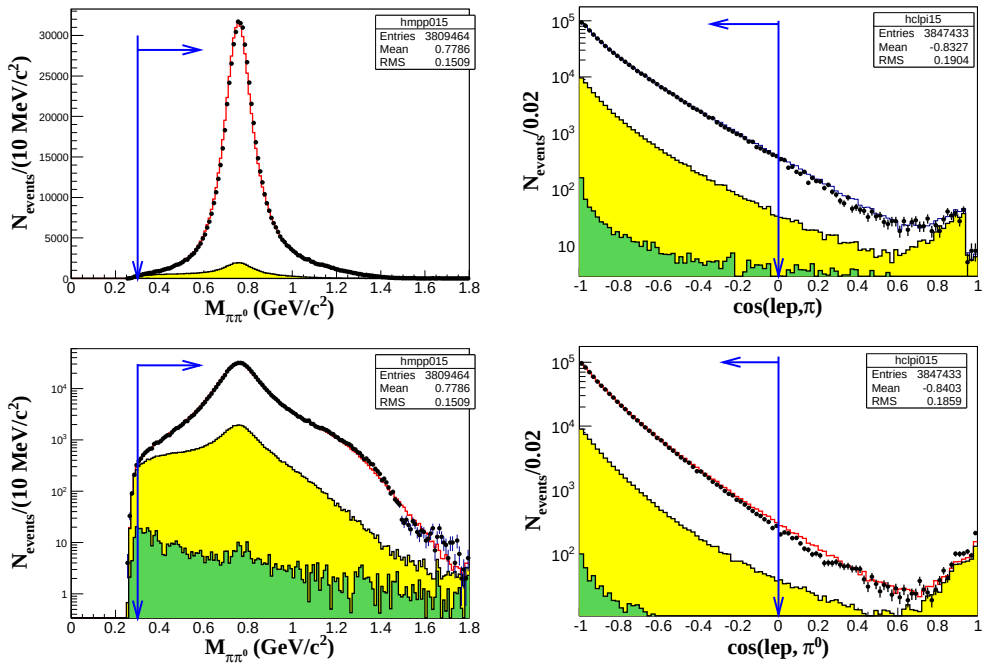

Figure 76: $\pi^-\pi^0$ invariant mass (upper left - linear scale, lower left - logarithmic scale), cosine of the angle between e^+ and π^- in CMS (upper right) and cosine of the angle between e^+ and π^0 in CMS (lower right) for the $(e^+;\pi^-\pi^0)$ events. Open histograms - full MC simulation, yellow shaded histograms - the main background components from $(e^+;\pi^-\pi^0\pi^0)$ events, green shaded histograms - the remaining background, points with errors - experimental data. MC and experimental histograms are normalized to the same number of events. Blue arrows show applied selections.

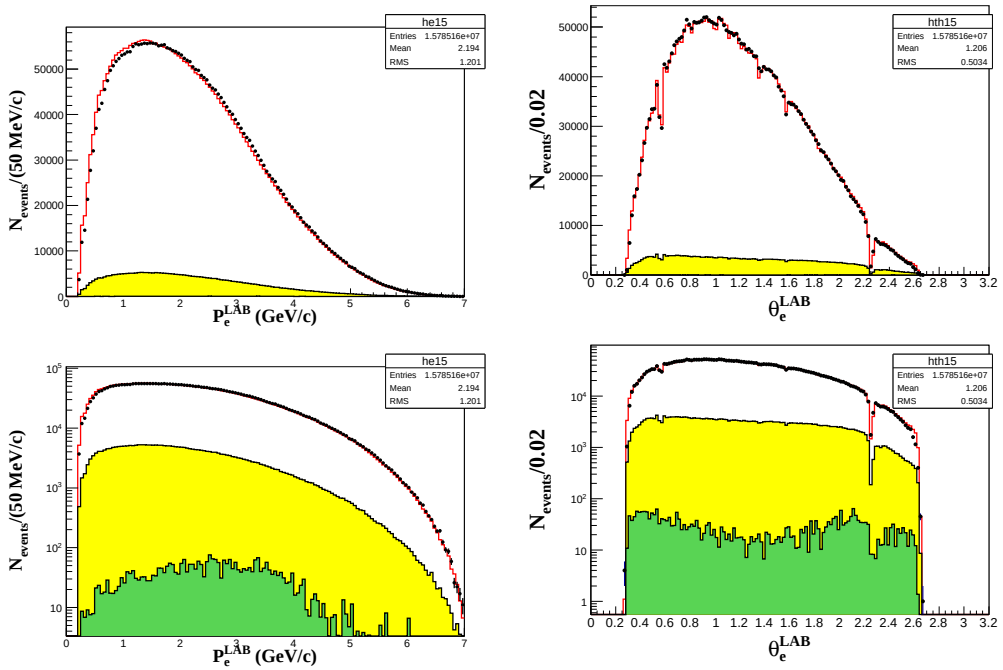

Figure 77: e^+ momentum (left) and polar angle (right) for the $(e^+;\pi^-\pi^0)$ events in LAB frame. Upper figures are shown in normal (linear) vertical scale, lower figures – in logarithmic scale. Open histograms - full MC simulation, yellow shaded histograms - the main background components from $(e^+;\pi^-\pi^0\pi^0)$ events, green shaded histograms - the remaining background, points with errors - experimental data. MC and experimental histograms are normalized to the same number of events.

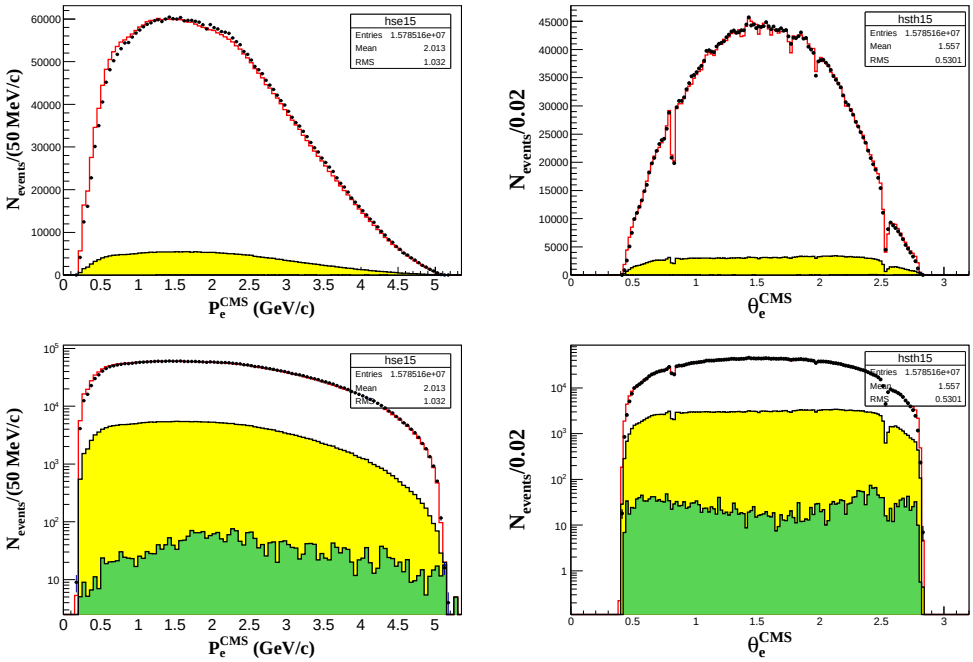

Figure 78: e^+ momentum (left) and polar angle (right) for the $(e^+;\pi^-\pi^0)$ events in CMS frame. Upper figures are shown in normal (linear) vertical scale, lower figures – in logarithmic scale. Open histograms - full MC simulation, yellow shaded histograms - the main background components from $(e^+;\pi^-\pi^0\pi^0)$ events, green shaded histograms - the remaining background, points with errors - experimental data. MC and experimental histograms are normalized to the same number of events.

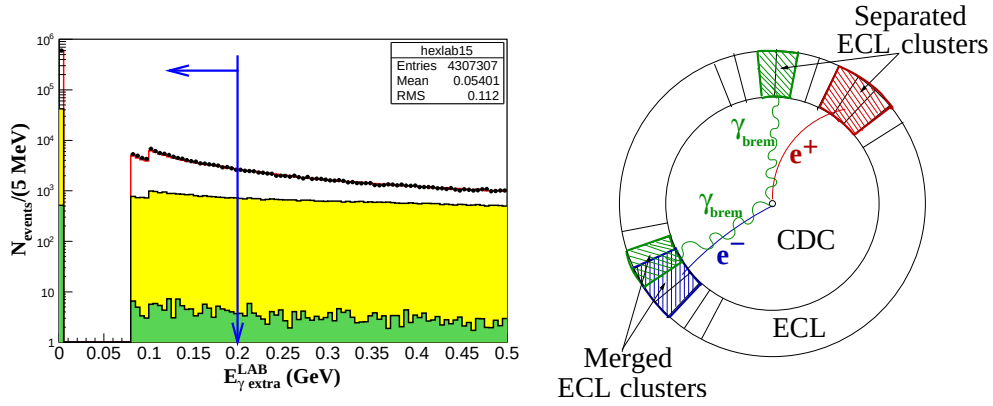

Figure 79: Extra gamma energy in LAB frame (left). Open histogram - full MC simulation, yellow shaded histogram - $(e^+;\pi^-\pi^0\pi^0)$ background, green shaded histogram - the remaining background, points with errors - experimental data. MC and experimental histograms are normalized to the same number of events. Right picture shows two different situations for the ECL cluster from external bremsstrahlung photon: cluster from high momentum e^- and photon are merged, cluster from low momentum e^+ and photon are different.

mental corrections can be large and should be properly taken into account. Fig. 87 helps to understand strong variation of the trigger efficiency for $(e,\ \rho)$ events. Two components are shown: only bits with Bhabha veto (red) and only bits without Bhabha veto (blue). While the efficiency of the second component is almost flat (∼70%) as a function of electron momentum, efficiency of the first component strongly varies from 100% down to $\sim 3-5\%$. This variation comes from the Bhabha veto argument, which was used in many Belle GDL output bits to suppress events of radiative Bhabha process $(e^+e^- \to e^+e^-(\gamma))$. Due to relatively low ECL energy deposition thresholds of about 5 GeV applied to form Bhabha veto argument efficiency of all output trigger bits with this argument almost vanishes by the electron momentum of about 6 GeV/c. Bhabha veto argument is not properly simulated (energy thresholds are not properly tuned in MC simulation), so quite large experiment/MC efficiency correction is expected for the "with Bhabha veto" component.

To determine trigger efficiency from the experimental data all bits should be separated into two physically independent subgroups, so called "charged"

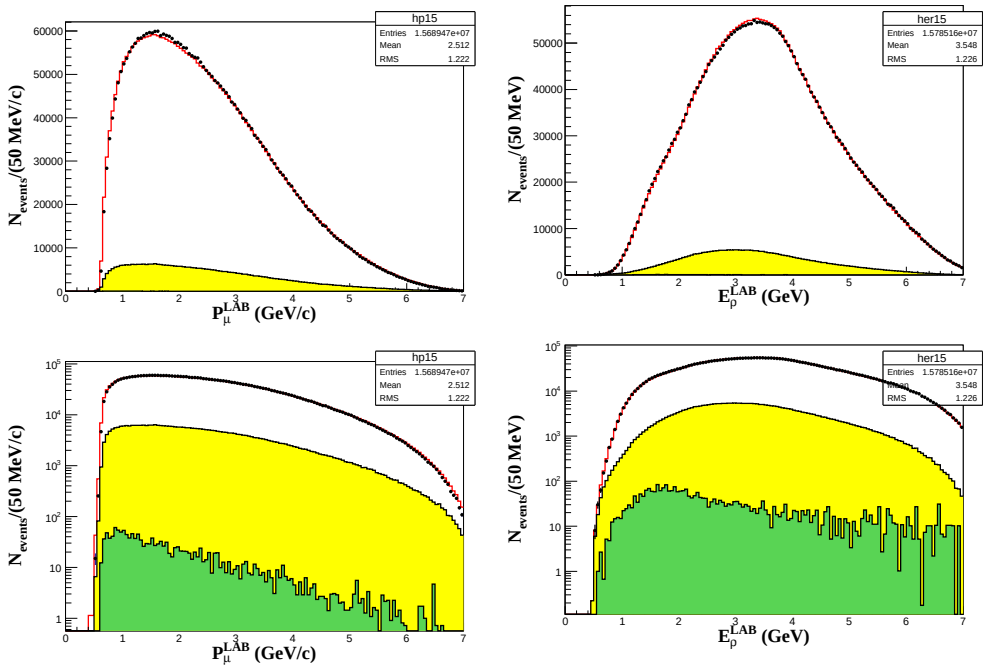

Figure 80: μ^+ momentum (left) and ρ^- energy (right) in LAB frame for the $(\mu^+;\pi^-\pi^0)$ events. Upper figures are shown in normal (linear) vertical scale, lower figures – in logarithmic scale. Open histograms - full MC simulation, yellow shaded histograms - $(e^+;\pi^-\pi^0\pi^0)$ background, green shaded histograms - the remaining background, points with errors - experimental data. MC and experimental histograms are normalized to the same number of events.

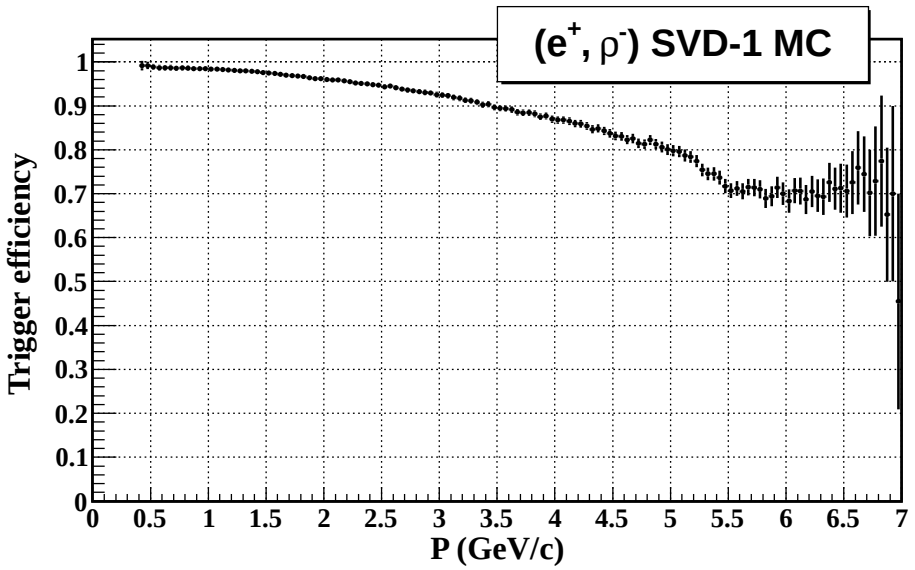

Figure 81: MC trigger efficiency for $(e^+,\ \rho^-)$ events, average efficiency $\bar{\varepsilon}_{trigger} = 93\%$

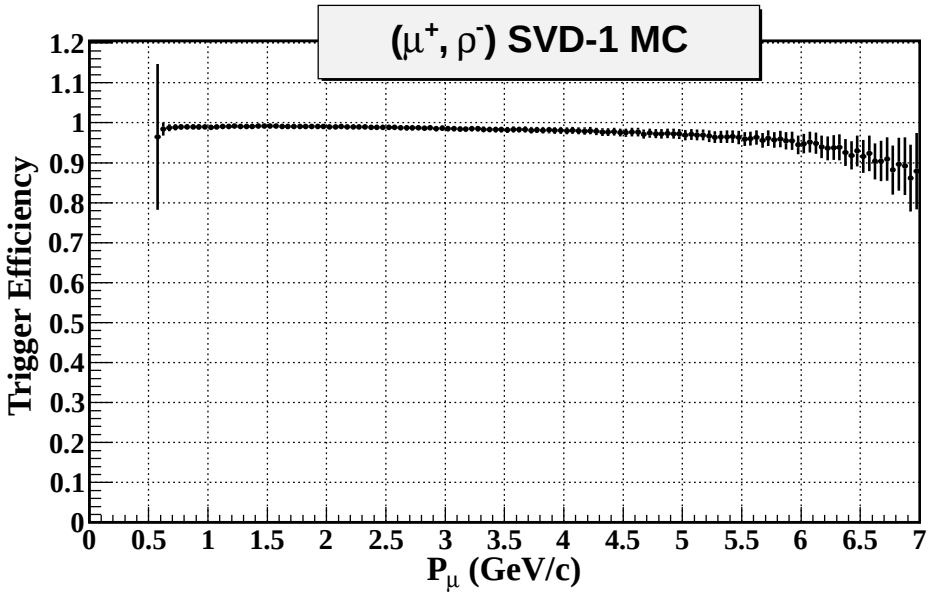

Figure 82: MC trigger efficiency for $(\mu^+,\ \rho^-)$ events, average efficiency $\bar{\varepsilon}_{trigger} = 99\%$

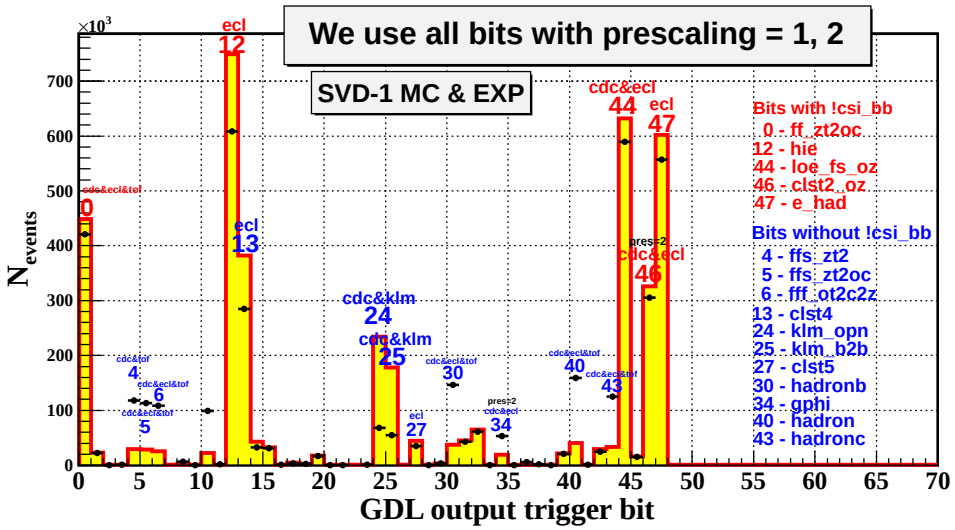

Figure 83: Distribution of the GDL output trigger bits for SVD-1 $(e^+;\rho^-)$ events. Yellow shaded histogram - signal MC, black points with errors - experimental data. Both histograms are normalized to the same number of events.

trigger (Z) (uses information from CDC, TOF, KLM), and ECL-based "neutral" trigger (N). Efficiency of each trigger can be determined as a relative frequency to the opposite trigger: $\varepsilon_Z = N(\text{Z AND N})/N(\text{N})$, $\varepsilon_N = N(\text{Z AND N})/N(\text{Z})$. As a result the total trigger efficiency reads:

$$\varepsilon_{\text{trig}} = \varepsilon_{Z\ OR\ N} = 1 - (1-\varepsilon_Z)(1-\varepsilon_N) \tag{92}$$

This algorithm is graphically clarified in Fig. 88 (left). For the SVD-1 experimental data sample we use this algorithm to determine efficiencies of the purely charged trigger (without Bhabha veto) and purely neutral trigger (with Bhabha veto), the result is shown in Fig. 89.

At Belle there are many mixed GDL output bits, especially with Bhabha veto argument, so it is difficult to use them in the trigger efficiency calibration. That is why for the further analysis we use only 9 bits. For the SVD-1 data charged and neutral triggers are formed from 5 bits (see their definition in Appendix A):

$$\text{Z} = \textbf{4} \text{ or } \textbf{24} \text{ or } \textbf{25}$$

$$\text{N} = \textbf{13} \text{ or } \textbf{27}$$

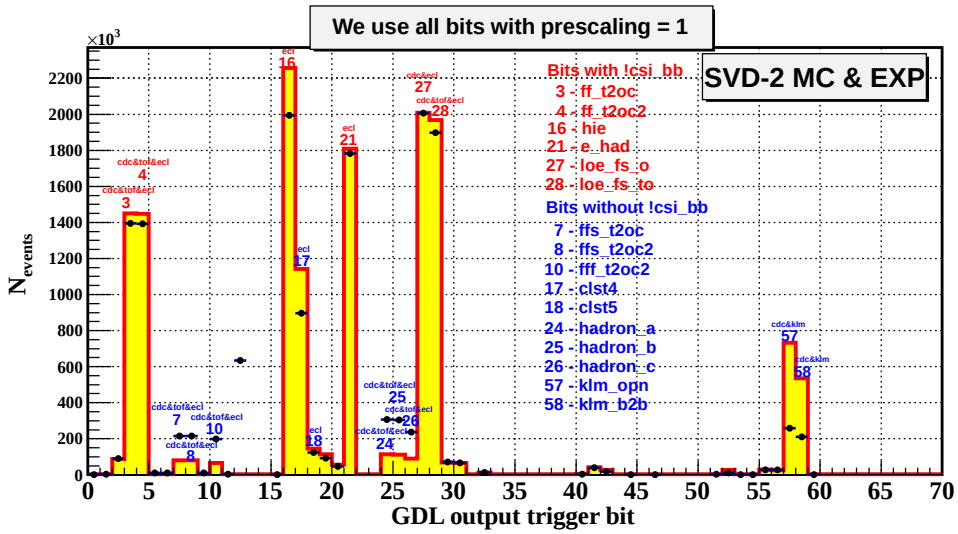

Figure 84: Distribution of the GDL output trigger bits for SVD-2 $(e^+;\rho^-)$ events. Yellow shaded histogram - signal MC, black points with errors - experimental data. Both histograms are normalized to the same number of events.

For the SVD-2 data charged and neutral triggers are formed from 4 bits (see the definition of the bits in Appendix A):

$$\mathrm{Z} = \mathbf{57} \text{ or } \mathbf{58}$$

$$\mathrm{N} = \mathbf{17} \text{ or } \mathbf{18}$$

As a result the trigger efficiency, $\varepsilon_{Z\ OR\ N}$, is only about 30% for the $(e^{\mp};\ \rho^{\pm})$ events, and about 60% for the $(\mu^{\mp};\ \rho^{\pm})$ events. So, in the procedure we should take into account these efficiencies explicitely:

$$\frac{N_Z}{N_0} = \varepsilon_Z^{sel}\cdot\varepsilon_Z^{trg}, \quad \frac{N_N}{N_0} = \varepsilon_N^{sel}\cdot\varepsilon_N^{trg}$$

$$\frac{N_{N\&Z}}{N_0} = \varepsilon_{N\&Z}^{sel}\cdot\varepsilon_{N\&Z}^{trg} = \varepsilon_{N\&Z}^{sel}\cdot\varepsilon_Z^{trg}\cdot\varepsilon_N^{trg}$$

$$\varepsilon_{\mathrm{trig}} = \left(\frac{N_Z N_N}{N_0 N_{N\&Z}}\right)\left\{\frac{N_{N\&Z}}{N_N} + \frac{N_{N\&Z}}{N_Z} - \left(\frac{N_{N\&Z}}{N_N}\right)\left(\frac{N_{N\&Z}}{N_Z}\right)\right\}, \tag{93}$$

$$\frac{N_Z N_N}{N_0 N_{N\&Z}} = \frac{\varepsilon_Z^{\mathrm{sel}}\varepsilon_N^{\mathrm{sel}}}{\varepsilon_{N\&Z}^{\mathrm{sel}}}, \tag{94}$$

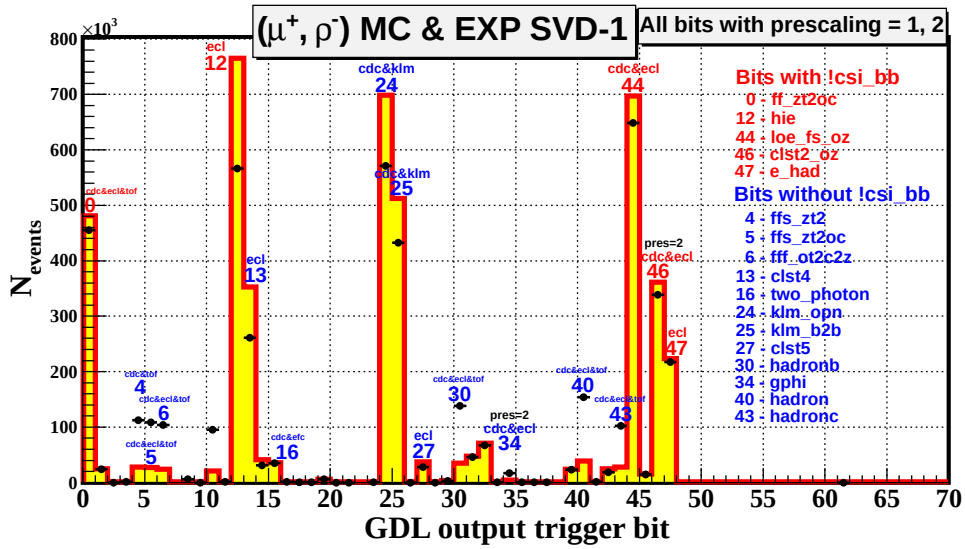

Figure 85: Distribution of the GDL output trigger bits for SVD-1 (μ^+, ρ^-) events. Yellow shaded histogram - signal MC, black points with errors - experimental data. Both histograms are normalized to the same number of events.

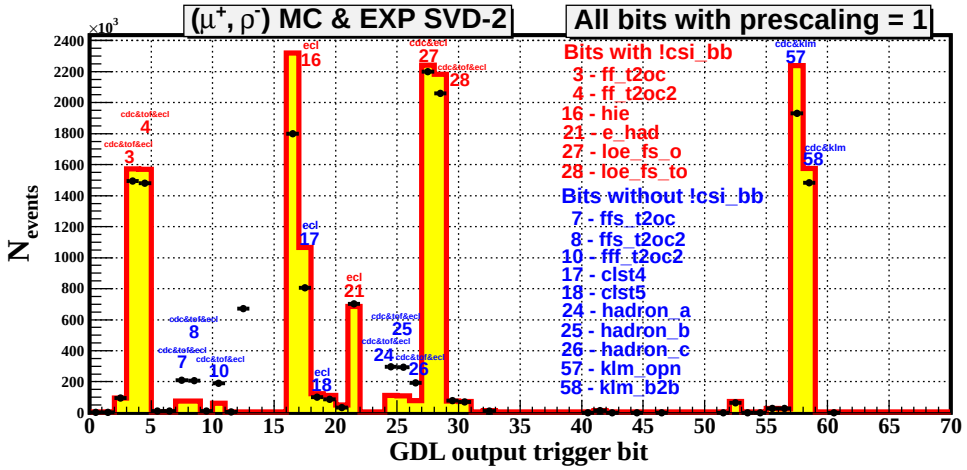

Figure 86: Distribution of the GDL output trigger bits for SVD-2 (μ^+, ρ^-) events. Yellow shaded histogram - signal MC, black points with errors - experimental data. Both histograms are normalized to the same number of events.

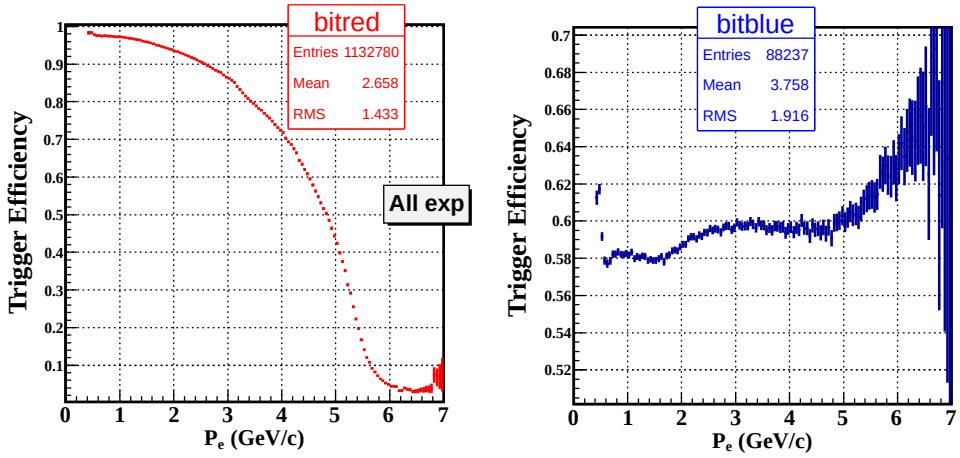

Figure 87: MC trigger efficiecy for (e^+; ρ^-) events as a function of e^+ momentum in LAB frame. Only bits with Bhabha veto (left) and only bits without Bhabha veto (right) components are shown.

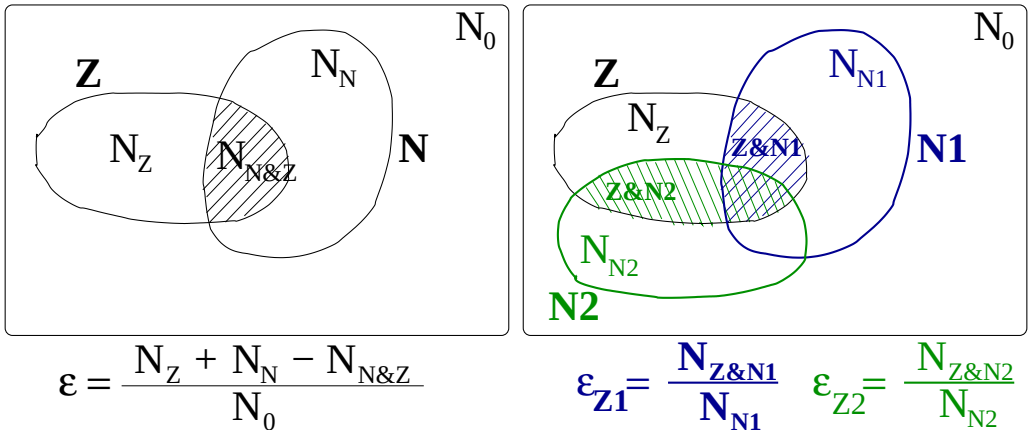

Figure 88: Graphical schemes clarifying calculation of the total trigger efficiency: one charged (Z) and one neutral (N) subtrigger case (left), one charged (Z) and two neutral (N1 and N2) subtriggers case (right)

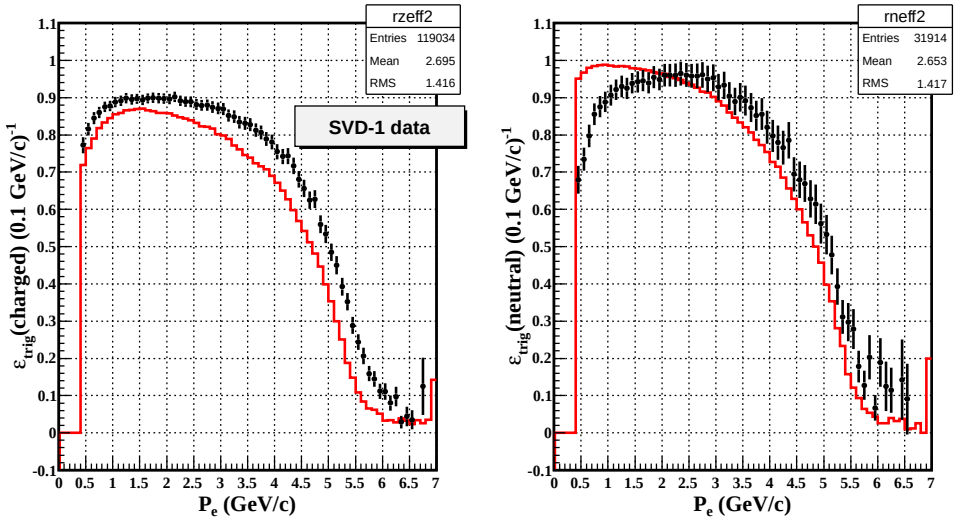

Figure 89: Efficiency as a function of e^+ LAB momentum for charged trigger (left) and neutral trigger with Bhabha veto (right) for SVD-1 (e^+; ρ^-) data sample. Open histograms - MC efficiencies, points with errors - experimental efficiencies calculated according Eq. 92.

In the assumption that:

$$\left(\frac{\varepsilon_Z^{\rm sel}\varepsilon_N^{\rm sel}}{\varepsilon_{N\&Z}^{\rm sel}}\right)^{\rm MC} = \left(\frac{\varepsilon_Z^{\rm sel}\varepsilon_N^{\rm sel}}{\varepsilon_{N\&Z}^{\rm sel}}\right)^{\rm EXP},$$

trigger efficiency can be written as:

$$\varepsilon_{\rm trig}^{\rm MC} = \left(\frac{N_Z N_N}{N_0 N_{N\&Z}}\right)^{\rm MC}\left\{\left(\frac{N_{N\&Z}}{N_N}\right)^{\rm MC} + \left(\frac{N_{N\&Z}}{N_Z}\right)^{\rm MC} - \left(\frac{N_{N\&Z}}{N_N}\frac{N_{N\&Z}}{N_Z}\right)^{\rm MC}\right\}, \quad (95)$$

$$\varepsilon_{\rm trig}^{\rm EXP} = \underline{\left(\frac{N_Z N_N}{N_0 N_{N\&Z}}\right)^{\rm MC}}\left\{\left(\frac{N_{N\&Z}}{N_N}\right)^{\rm EXP} + \left(\frac{N_{N\&Z}}{N_Z}\right)^{\rm EXP} - \left(\frac{N_{N\&Z}}{N_N}\frac{N_{N\&Z}}{N_Z}\right)^{\rm EXP}\right\}, \quad (96)$$

as a result trigger efficiency experiment/MC correction reads:

$$\mathcal{R}_{\rm trig} = \frac{\varepsilon_{\rm trig}^{\rm EXP}}{\varepsilon_{\rm trig}^{\rm MC}} = \frac{\left(\frac{N_{N\&Z}}{N_N}\right)^{\rm EXP} + \left(\frac{N_{N\&Z}}{N_Z}\right)^{\rm EXP} - \left(\frac{N_{N\&Z}}{N_N}\frac{N_{N\&Z}}{N_Z}\right)^{\rm EXP}}{\left(\frac{N_{N\&Z}}{N_N}\right)^{\rm MC} + \left(\frac{N_{N\&Z}}{N_Z}\right)^{\rm MC} - \left(\frac{N_{N\&Z}}{N_N}\frac{N_{N\&Z}}{N_Z}\right)^{\rm MC}}. \quad (97)$$

Fig. 90 shows trigger efficiency corrections determined by Eq. 97 for the SVD-1 and SVD-2 ($e;\ \rho$) data samples, and Fig. 91 demonstrates trigger efficiency corrections for the SVD-1 and SVD-2 ($\mu;\ \rho$) data samples. Corrections as a functions of lepton momentum in laboratory frame were approximated by empirical functions, which are used in the fitter.

6.2 Lepton identification efficiency corrections

Lepton identification (ℓID) efficiency corrections were calculated using the $e^+e^- \to e^+e^-\ell^+\ell^-,\ \ell = e, \mu$ two-photon data sample [49]. We used the tables obtained by Belle joint particle identification group [50]. In these tables efficiency corrections are calculated in 70 bins on the 2D plane of transversal momentum versus polar angle in LAB. We apply these corrections to the signal MC sample to calculate the correction as a function of lepton momentum, see it in Fig. 90 for the ($e^{\pm};\ \rho^{\mp}$) events and in Fig. 91 for the ($\mu^{\pm};\ \rho^{\mp}$) events. The uncertainty of ℓID efficiency correction is determined by the statistics of the $e^+e^- \to e^+e^-\ell^+\ell^-$ sample and the long-term stability, which is evaluated from the variation of the corrections calculated for time ordered subsamples of the experimental two-photon data [49]. ℓID corrections were approximated by appropriately chosen empirical functions, which are used in the fitter then.

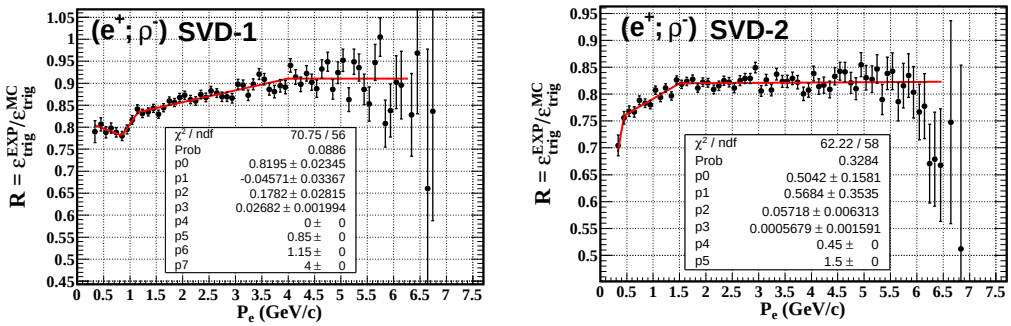

Figure 90: Trigger efficiency correction for SVD-1 (left) and SVD-2 (right) (e; ρ) data samples as a function of electron momentum in LAB - black points with errors. It is fitted by empirical function, shown by red solid line.

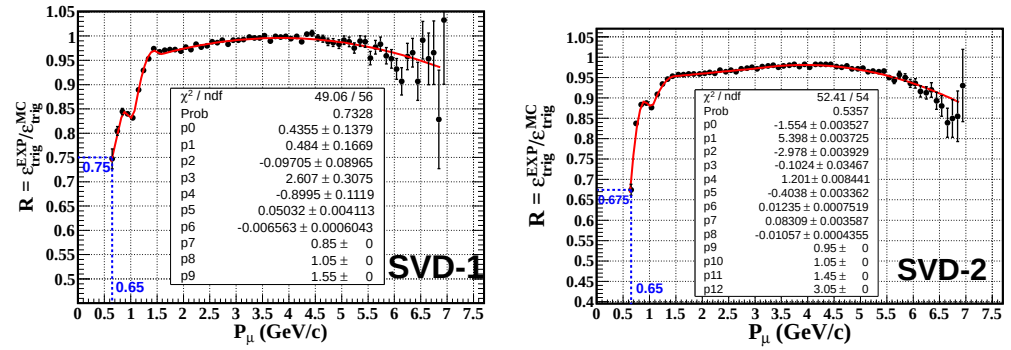

Figure 91: Trigger efficiency correction for SVD-1 (left) and SVD-2 (right) (μ; ρ) data samples as a function of muon momentum in LAB - black points with errors. It is fitted by empirical function, shown by red solid line.

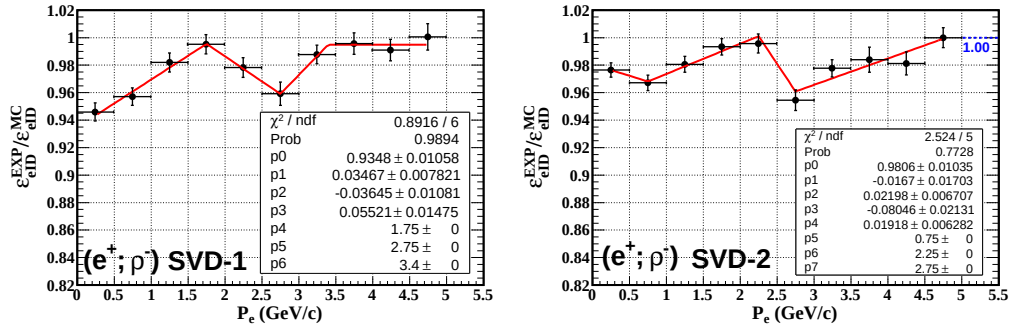

Figure 92: $e^{\pm}$ identification efficiency as a function of the $e^{\pm}$ momentum in LAB for SVD-1 (left) and SVD-2 (right) (e; ρ) events. Points with errors - efficiency correction, red solid line - empirical function.

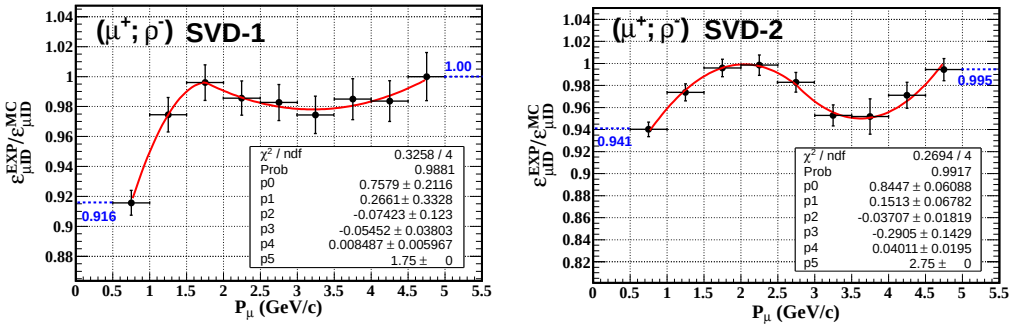

Figure 93: $\mu^{\pm}$ identification efficiency as a function of the $\mu^{\pm}$ momentum in LAB for (μ; ρ) events. Points with errors - efficiency correction, red solid line - empirical function.

7 Fit of experimental data

Result of the fit of experimental data, where the PDF for the remaining background was described according to the $\mathcal{P}_{4D}(p_\ell,\ p_\rho,\ \omega,\ \cos\psi_{\ell\rho})\cdot\mathcal{P}_{1D}(\varphi_\ell)\cdot\mathcal{P}_{1D}(\varphi_\rho)\cdot\mathcal{P}_{1D}(m^2_{\pi\pi})\cdot\mathcal{P}_{1D}(\cos\tilde{\theta}_\pi)\cdot\mathcal{P}_{1D}(\tilde{\varphi}_\pi)$(or shortly 4D$\otimes$1D^5) scheme (see Sect. 4) is shown in Tables 11,12.

Table 11: Result of the fit of experimental data (4D$\otimes$1D^5 scheme is used to describe the remaining background). Only statistical errors are shown for optimal Michel parameters. For the $(e^{\mp};\ \rho^{\pm})$ events η parameter is fixed at its Standard Model value ($\eta_{\rm SM}=0$).

$(e^+;\ \pi^-\pi^0)$				
ρ	=	0.7610	$\pm$	0.0022
η	=	0	$-$	fixed
ξ	=	1.0211	$\pm$	0.0092
$\xi\delta$	=	0.7278	$\pm$	0.0057

$(e^-;\ \pi^+\pi^0)$				
ρ	=	0.7566	$\pm$	0.0021
η	=	0	$-$	fixed
ξ	=	1.0180	$\pm$	0.0091
$\xi\delta$	=	0.7505	$\pm$	0.0057

$(\mu^+;\ \pi^-\pi^0)$				
ρ	=	0.7543	$\pm$	0.0041
η	=	-0.0395	$\pm$	0.0155
ξ	=	0.9797	$\pm$	0.0075
$\xi\delta$	=	0.7630	$\pm$	0.0050

$(\mu^-;\ \pi^+\pi^0)$				
ρ	=	0.7542	$\pm$	0.0041
η	=	-0.0390	$\pm$	0.0154
ξ	=	0.9884	$\pm$	0.0075
$\xi\delta$	=	0.7732	$\pm$	0.0050

Table 12: Result of the simulataneous fit of the $(e^+;\ \pi^-\pi^0)$, $(e^-;\ \pi^+\pi^0)$, $(\mu^+;\ \pi^-\pi^0)$ and $(\mu^-;\ \pi^+\pi^0)$ experimental events (4D$\otimes$1D^5 scheme is used to describe the remaining background). Only statistical errors are shown for optimal Michel parameters.

ρ	=	0.7576	$\pm$	0.0014
η	=	-0.0282	$\pm$	0.0062
ξ	=	0.9985	$\pm$	0.0039
$\xi\delta$	=	0.7589	$\pm$	0.0025

Figures 94- 97 show fit result as a comparison of the experimental and optimal distributions for the $(e^+;\ \rho^-)$ events. In Fig. 94 the comparison of the experimental and optimal e^+ CMS energy distributions is shown for the $(e^+;\ \rho^-)$ events. Reasonable agreement can be observed for the whole energy range, although the relative difference between these spectra (varies

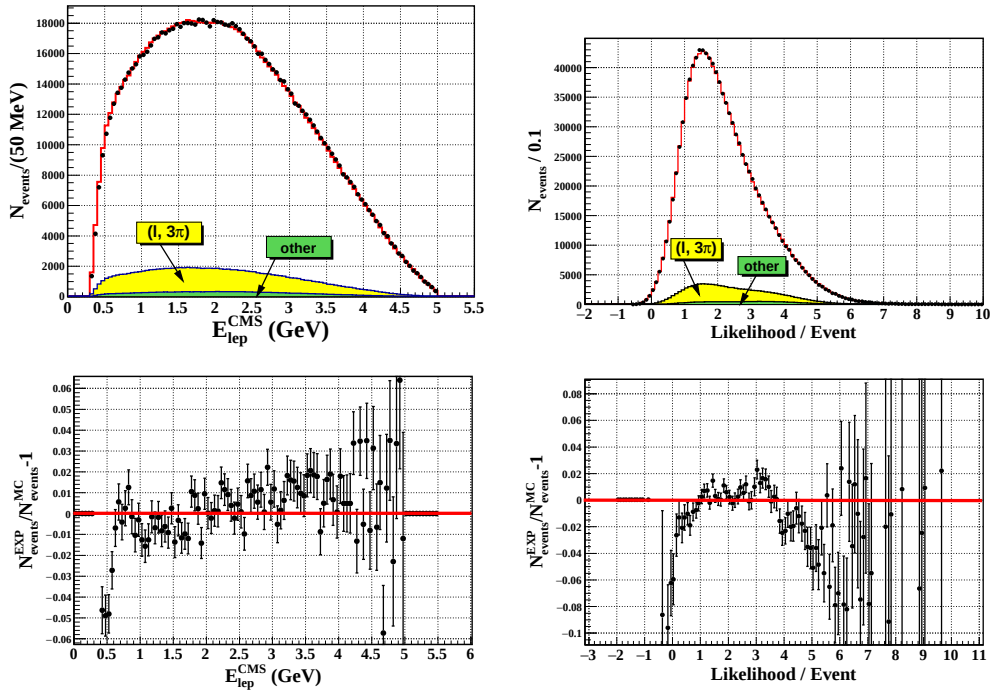

Figure 94: Result of the fit of (e^+; ρ^-) experimental events (4D$\otimes$1D^5 scheme). e^+ energy spectrum in CMS (left top), relative difference between experimental energy spectrum and fit result (left bottom), likelihood per event (top right) and relative difference between experimental likelihood per event and fit result(bottom right). Points with errors show experimental data, histogram - result of the fit. Open histograms show signal events, shaded histograms - background contributions.

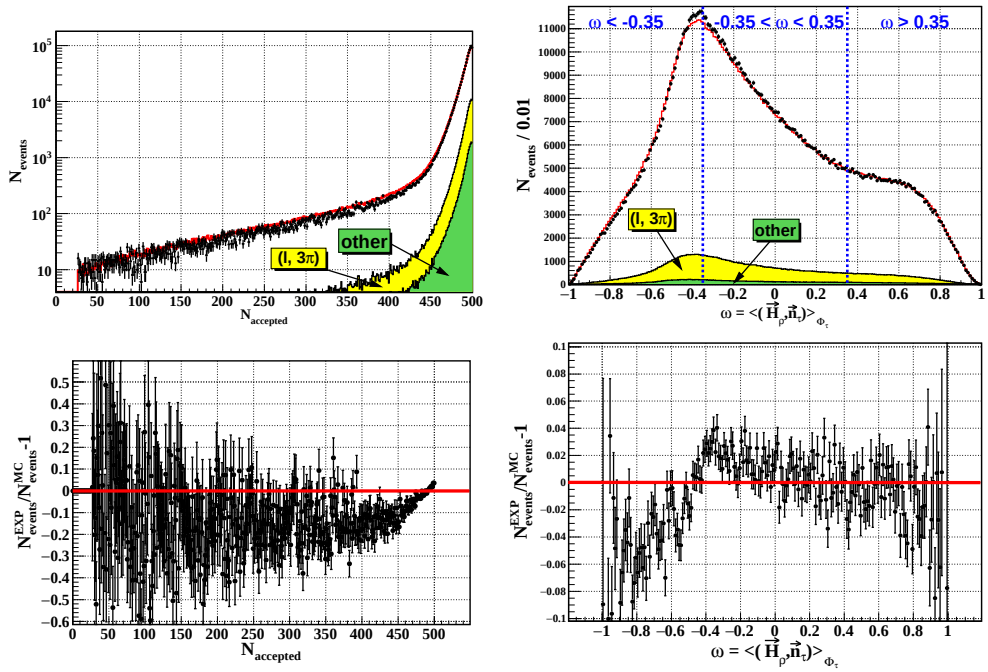

Figure 95: Result of the fit of $(e^+;\ \rho^-)$ experimental events ($4D \otimes 1D^5$ scheme). Number of accepted trials in the procedure of the numerical integration of the differential cross section (left top), relative difference between experimental number of accepted trials and fit result (left bottom), τ helicity sensitive variable, ω, (see Section 2) (top right) and relative difference between experimental ω and fit result (bottom right). Points with errors show experimental data, histogram - result of the fit. Open histograms show signal events, shaded histograms - background contributions.

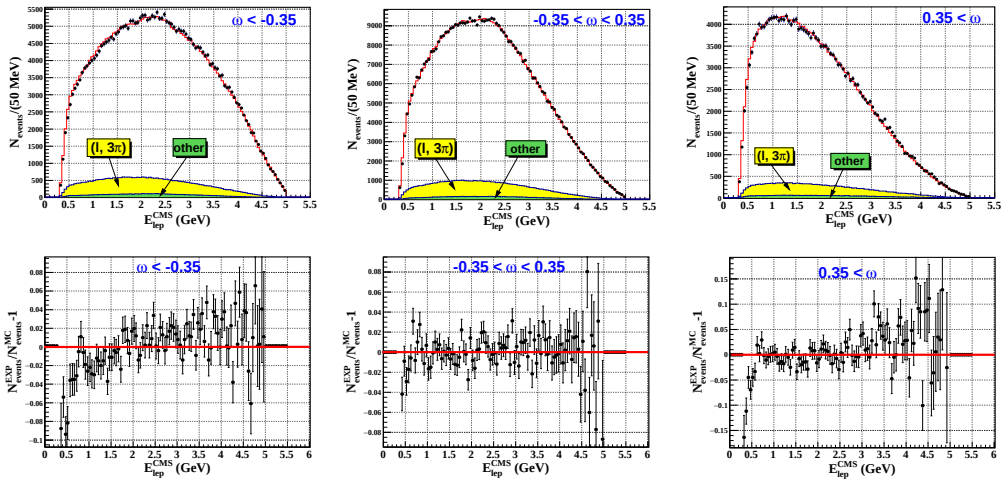

Figure 96: Result of the fit of $(e^+;\ \rho^-)$ experimental events ($4D \otimes 1D^5$ scheme). Three e^+ energy spectra are shown for different ranges in ω: $\omega < -0.35$ (upper left), $-0.35 < \omega < 0.35$ (upper middle), $\omega > 0.35$ (upper right). The corresponding relative differences between experimental spectra and fit results are shown in the lower figures. Points with errors show experimental data, histogram - result of the fit. Open histograms show signal events, shaded histograms - background contributions.

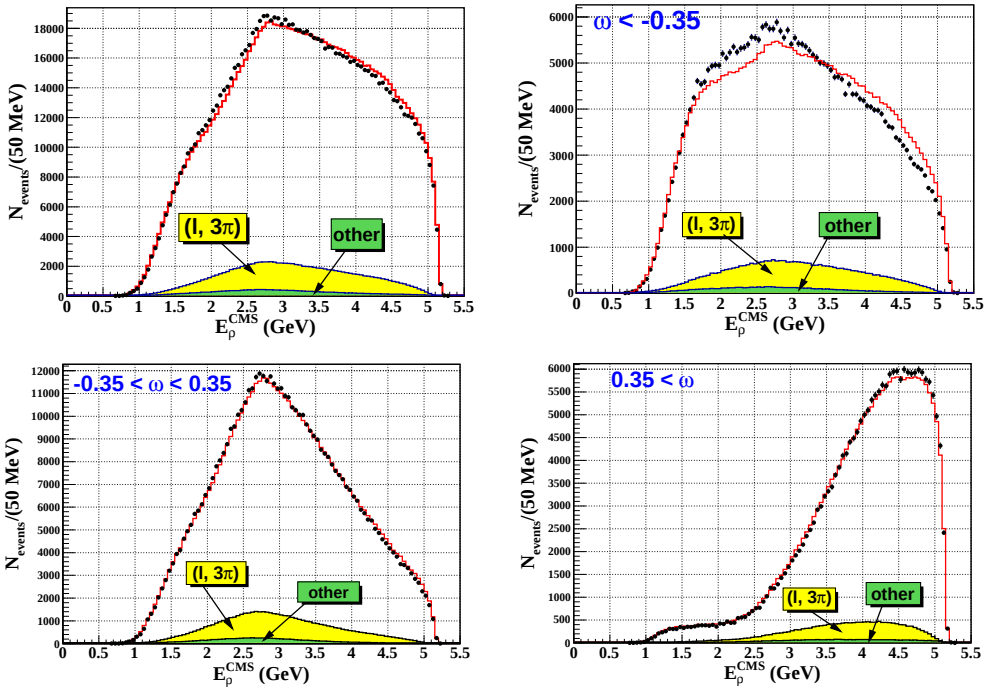

Figure 97: Result of the fit of $(e^+;\ \rho^-)$ experimental events (4D$\otimes$1D^5 scheme). ρ energy spectra are shown: total spectrum (top left), spectrum for the events with $\omega < -0.35$ (top right), $-0.35 < \omega < 0.35$ (bottom left), $\omega > 0.35$ (bottom right). Points with errors show experimental data, histogram - result of the fit. Open histograms show signal events, shaded histograms - background contributions.

from approximately -1% up to $\sim 2\%$ in the whole energy range) indicates some notable systematic effect. Distribution of the likelihood per event shows good quality of the fit. Distribution of τ helicity sensitive variable ω (see Section 2) for $(e^+;\ \rho^-)$ events is shown in Fig. 95. And spin-spin correlation of taus is clearly demonstrated in Fig. 96 for the $(e^+;\ \rho^-)$ events. The e^+ energy spectrum shape notably varies as the tau helicity sensitive variable, ω, goes from -1 to $+1$. Figure 97 shows the distribution of the ρ energy in CMS. It is clearly seen that the difference between experimental data and fit result is mostly accumulated in the region $\omega < -0.35$.

Figures 98-101 demonstrate result of the fit for the $(\mu^+;\ \rho^-)$ events. Muon energy spectrum and likelihood per event distributions are shown in Fig. 98. Relative difference between experimental and optimal μ^+ energy spectra shows variation, similar to $(e^+;\ \rho^-)$ case, from approximately -1% up to $\sim 2\%$ in the whole energy range. Distribution of the likelihood per event shows good quality of the fit, although the relative difference between experimental and optimal distributions exhibits some disagreement, especially in the low likelihood region. Distribution of ω for $(\mu^+;\ \rho^-)$ events is shown in Fig. 99. And spin-spin correlation of taus is clearly demonstrated in Fig. 100 for the $(\mu^+;\ \rho^-)$ events. The μ^+ energy spectrum shape notably varies as ω runs from -1 to $+1$. Figure 101 shows the distribution of the ρ energy in CMS. It is clearly seen that the agreement between the experimental and optimal spectra is much better than for the $(e^+;\ \rho^-)$ events. The ρ candidate is reconstructed equally in $(e^\pm;\ \rho^\mp)$ and $(\mu^\pm;\ \rho^\mp)$ events. The main difference comes from the trigger efficiency, which is smaller in the $(e^\pm;\ \rho^\mp)$ events by a factor of about 2 in comparison with the $(\mu^\pm;\ \rho^\mp)$ events. The correction to the trigger efficiency is essential and, probably, it should be tabulated as a function of several variables (not only lepton energy).

Figures 102-106 show result of the fit of experimental events ($4\mathrm{D}\otimes 1\mathrm{D}^5$ scheme) as a function of the extra gamma energy ($E^{\mathrm{LAB}}_{\gamma\ \mathrm{extra}}$) cut.

Result of the fit of experimental data, where the PDF for the remaining background was described according to the $\mathcal{P}_{3\mathrm{D}}(p_\ell,\ \cos\psi_{\ell\rho},\ p_\rho)\cdot\mathcal{P}_{2\mathrm{D}}(\varphi_\rho,\ \tilde{\varphi}_\pi)\cdot\frac{\mathcal{P}_{2\mathrm{D}}(p_\ell,\ \cos\theta_\rho)}{\mathcal{P}_{1\mathrm{D}}(p_\ell)}\cdot\frac{\mathcal{P}_{2\mathrm{D}}(p_\rho,\ \cos\tilde{\theta_\pi})}{\mathcal{P}_{1\mathrm{D}}(p_\rho)}\cdot\frac{\mathcal{P}_{2\mathrm{D}}(p_\rho,\ m^2_{\pi\pi})}{\mathcal{P}_{1\mathrm{D}}(p_\rho)}\cdot\frac{\mathcal{P}_{2\mathrm{D}}(\cos\psi_{\ell\rho},\ \Delta\varphi_{\ell\rho})}{\mathcal{P}_{1\mathrm{D}}(\cos\psi_{\ell\rho})}$ (or shortly $3\mathrm{D}\otimes 2\mathrm{D}^5/1\mathrm{D}^4$) scheme (see Sect. 4) is shown in Tables 13,14. And Figures 107-111 show result of the fit of experimental events ($3\mathrm{D}\otimes 2\mathrm{D}^5/1\mathrm{D}^4$ scheme) as a function of the extra gamma energy ($E^{\mathrm{LAB}}_{\gamma\ \mathrm{extra}}$) cut. As a reference we chose the fit with the $3\mathrm{D}\otimes 2\mathrm{D}^5/1\mathrm{D}^4$ scheme, see the result of the simultaneous fit in Table 14.

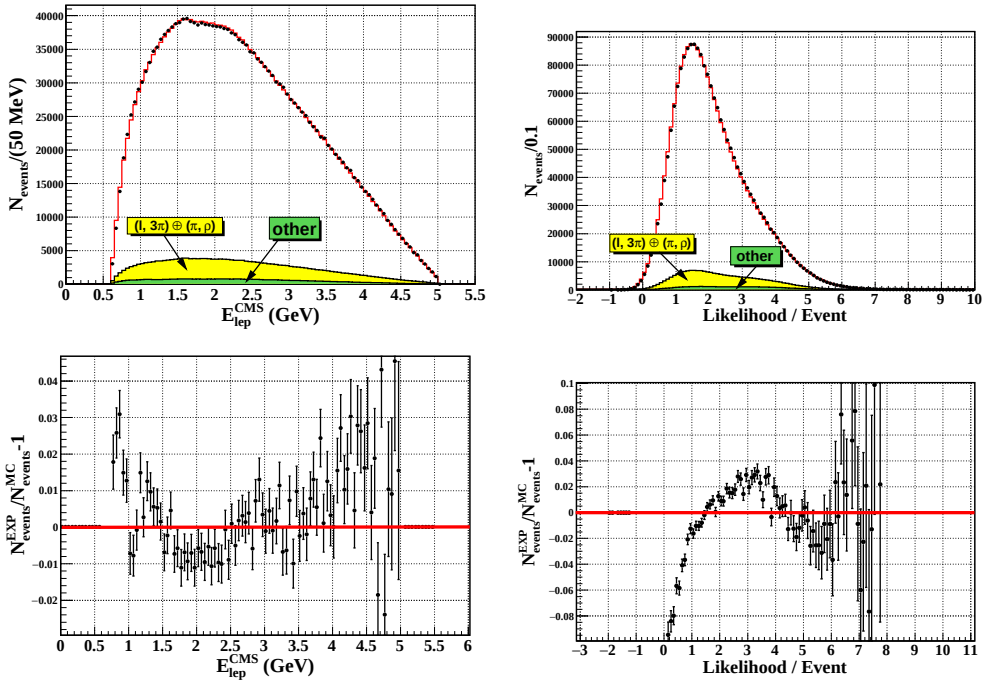

Figure 98: Result of the fit of (μ^+; ρ^-) experimental events (4D$\otimes$1D^5 scheme). μ^+ energy spectrum in CMS (left top), relative difference between experimental energy spectrum and fit result (left bottom), likelihood per event (top right) and relative difference between experimental likelihood per event and fit result(bottom right). Points with errors show experimental data, histogram - result of the fit. Open histograms show signal events, shaded histograms - background contributions.

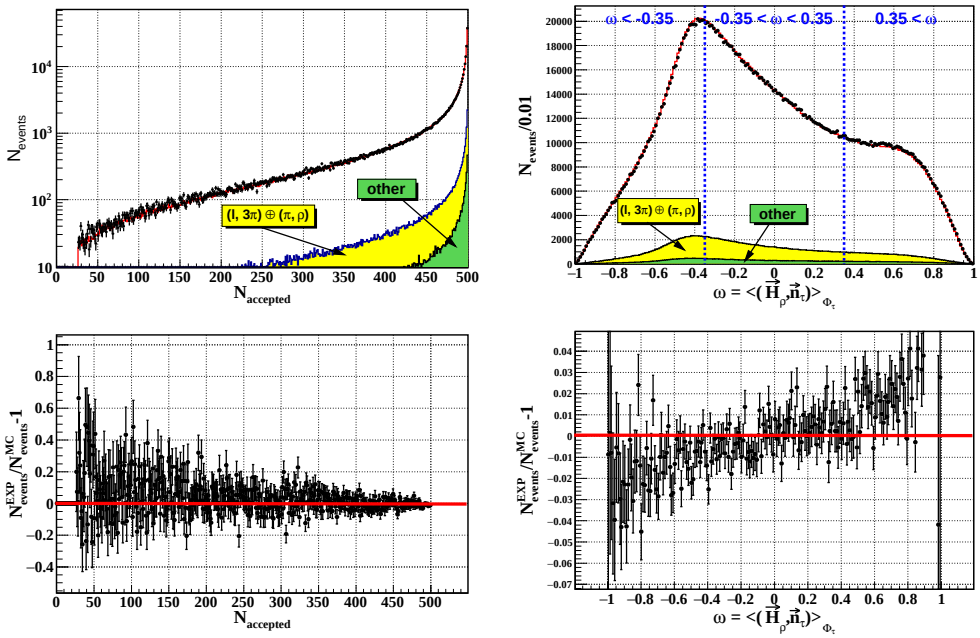

Figure 99: Result of the fit of $(\mu^+;\ \rho^-)$ experimental events (4D$\otimes$1D[5] scheme). Number of accepted trials in the procedure of the numerical integration of the differential cross section (left top), relative difference between experimental number of accepted trials and fit result (left bottom), τ helicity sensitive variable, ω, (see Section 2) (top right) and relative difference between experimental ω and fit result (bottom right). Points with errors show experimental data, histogram - result of the fit. Open histograms show signal events, shaded histograms - background contributions.

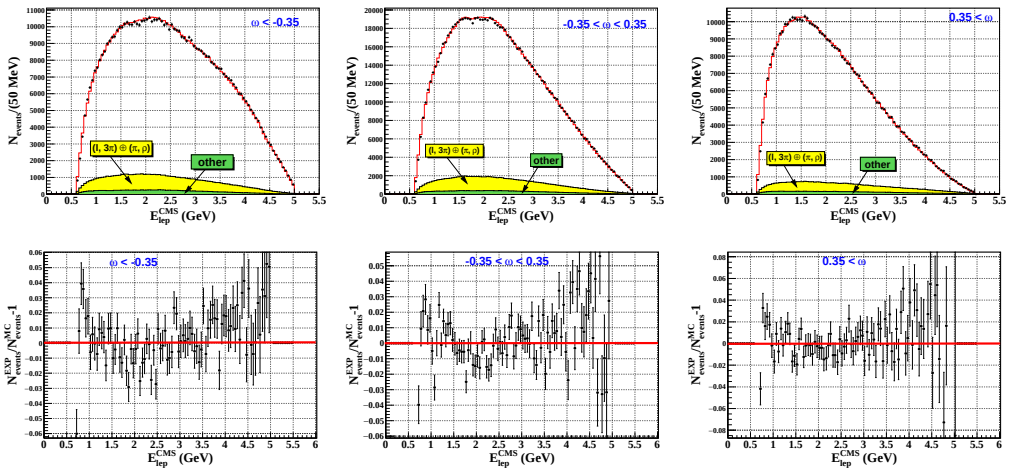

Figure 100: Result of the fit of $(\mu^+;\ \rho^-)$ experimental events ($4D\otimes 1D^5$ scheme). Three μ^+ energy spectra are shown for different ranges in ω: $\omega < -0.35$ (upper left), $-0.35 < \omega < 0.35$ (upper middle), $\omega > 0.35$ (upper right). The corresponding relative differences between experimental spectra and fit results are shown in the lower figures. Points with errors show experimental data, histogram - result of the fit. Open histograms show signal events, shaded histograms - background contributions.

Table 13: Result of the fit of experimental data ($3D\otimes 2D^5/1D^4$ scheme is used to describe the remaining background). Only statistical errors are shown for optimal Michel parameters. For the $(e^{\mp};\ \rho^{\pm})$ events η parameter is fixed at its Standard Model value ($\eta_{\rm SM} = 0$).

$(e^+;\ \pi^-\pi^0)$				
ρ	=	0.7627	$\pm$	0.0021
η	=	0	$-$	fixed
ξ	=	1.0201	$\pm$	0.0091
$\xi\delta$	=	0.7244	$\pm$	0.0057
$(\mu^+;\ \pi^-\pi^0)$				
ρ	=	0.7557	$\pm$	0.0041
η	=	-0.0381	$\pm$	0.0155
ξ	=	0.9776	$\pm$	0.0075
$\xi\delta$	=	0.7543	$\pm$	0.0049

$(e^-;\ \pi^+\pi^0)$				
ρ	=	0.7566	$\pm$	0.0021
η	=	0	$-$	fixed
ξ	=	1.0183	$\pm$	0.0091
$\xi\delta$	=	0.7471	$\pm$	0.0056
$(\mu^-;\ \pi^+\pi^0)$				
ρ	=	0.7550	$\pm$	0.0041
η	=	-0.0395	$\pm$	0.0154
ξ	=	0.9872	$\pm$	0.0075
$\xi\delta$	=	0.7643	$\pm$	0.0049

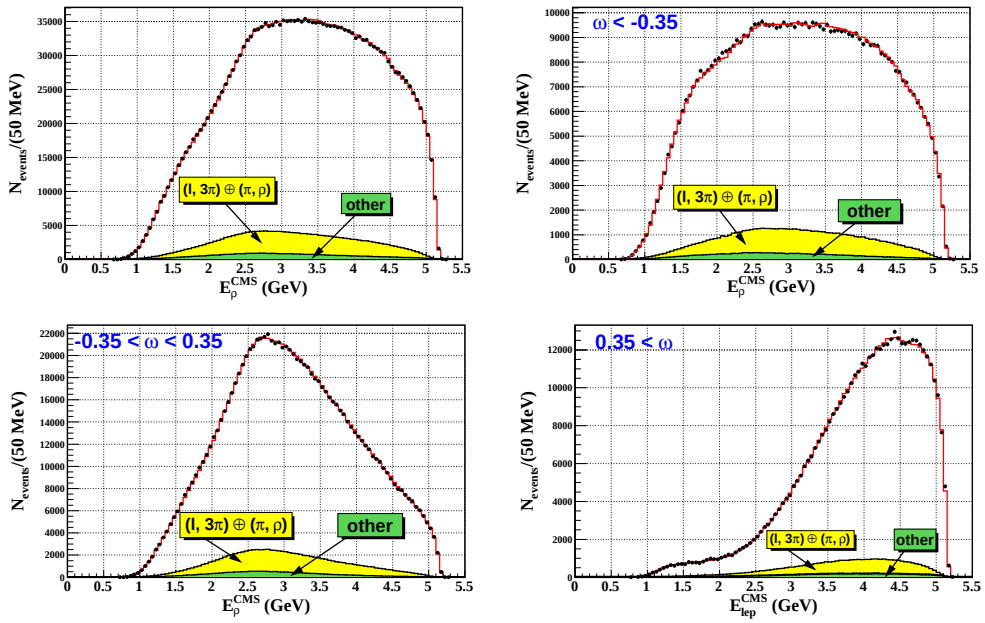

Figure 101: Result of the fit of $(\mu^+;\ \rho^-)$ experimental events (4D$\otimes$1D^5 scheme). ρ energy spectra are shown: total spectrum (top left), spectrum for the events with $\omega < -0.35$ (top right), $-0.35 < \omega < 0.35$ (bottom left), $\omega > 0.35$ (bottom right). Points with errors show experimental data, histogram - result of the fit. Open histograms show signal events, shaded histograms - background contributions.

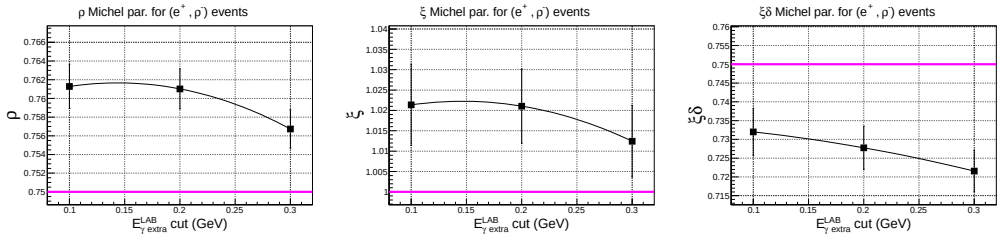

Figure 102: Optimal values of Michel parameters, ρ (left), ξ (middle), $\xi\delta$ (right), from the fit of the experimental $(e^+;\ \pi^-\pi^0)$ events (4D$\otimes$1D^5 scheme) as a function of the extra gamma energy ($E^{\rm LAB}_{\gamma\ \rm extra}$) cut. Magenta line shows the SM expectation for the corresponding Michel parameter.

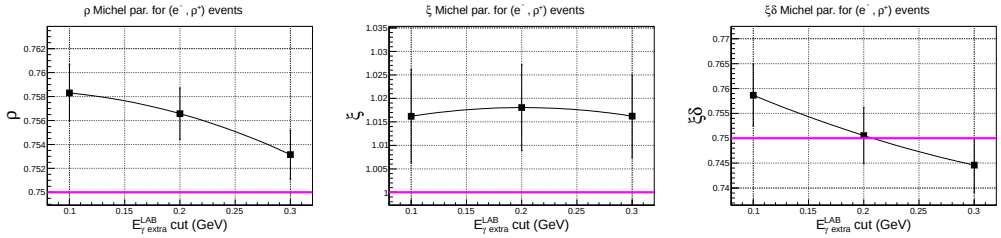

Figure 103: Optimal values of Michel parameters, ρ (left), ξ (middle), $\xi\delta$ (right), from the fit of the experimental (e^-; $\pi^+\pi^0$) events (4D$\otimes$1D^5 scheme) as a function of the extra gamma energy ($E^{\rm LAB}_{\gamma\ {\rm extra}}$) cut. Magenta line shows the SM expectation for the corresponding Michel parameter.

Table 14: Result of the simulataneous fit of the (e^+; $\pi^-\pi^0$), (e^-; $\pi^+\pi^0$), (μ^+; $\pi^-\pi^0$) and (μ^-; $\pi^+\pi^0$) experimental events (3D$\otimes$2D^5/1D^4 scheme is used to describe the remaining background). Only statistical errors are shown for optimal Michel parameters.

ρ	=	0.7586	$\pm$	0.0013
η	=	-0.0276	$\pm$	0.0062
ξ	=	0.9973	$\pm$	0.0039
$\xi\delta$	=	0.7520	$\pm$	0.0025

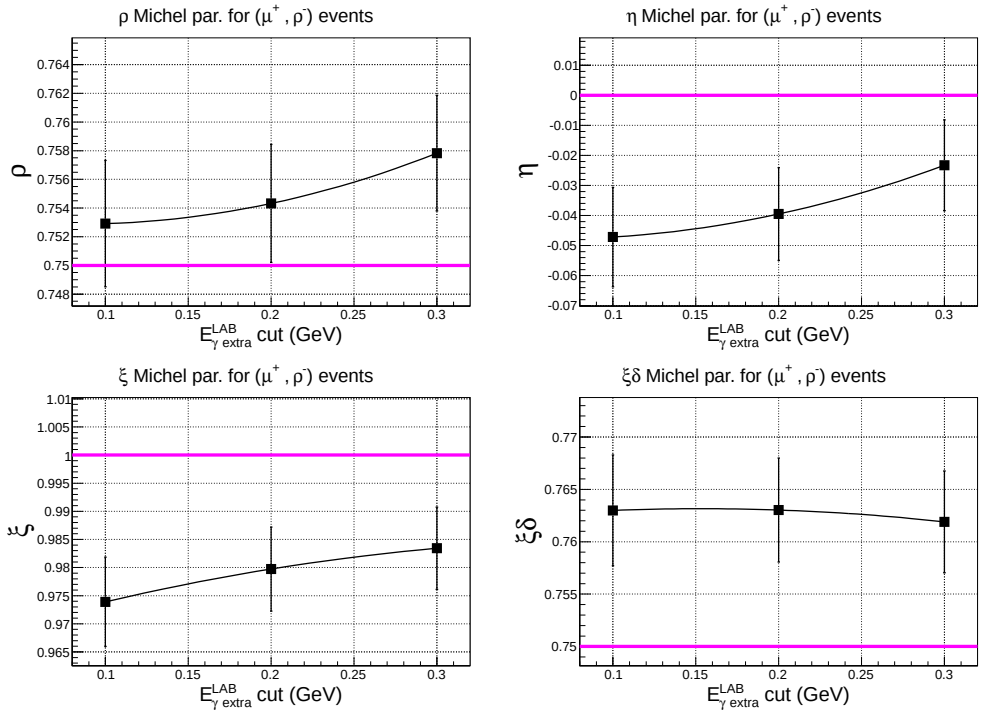

Figure 104: Optimal values of Michel parameters, ρ (upper left), η (upper right), ξ (lower left), $\xi\delta$ (lower right), from the fit of the experimental (μ^+; $\pi^-\pi^0$) events (4D$\otimes$1D^5 scheme) as a function of the extra gamma energy ($E^{\rm LAB}_{\gamma\ {\rm extra}}$) cut. Magenta line shows the SM expectation for the corresponding Michel parameter.

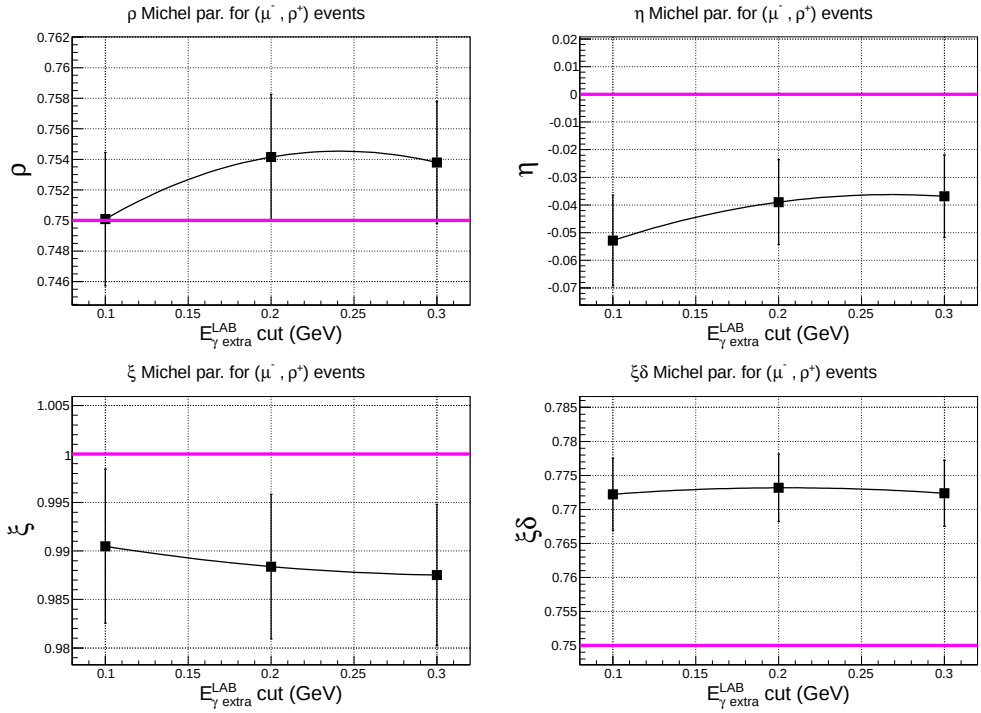

Figure 105: Optimal values of Michel parameters, ρ (upper left), η (upper right), ξ (lower left), $\xi\delta$ (lower right), from the fit of the experimental (μ^-; $\pi^+\pi^0$) events (4D$\otimes$1D^5 scheme) as a function of the extra gamma energy ($E^{\rm LAB}_{\gamma\ {\rm extra}}$) cut. Magenta line shows the SM expectation for the corresponding Michel parameter.

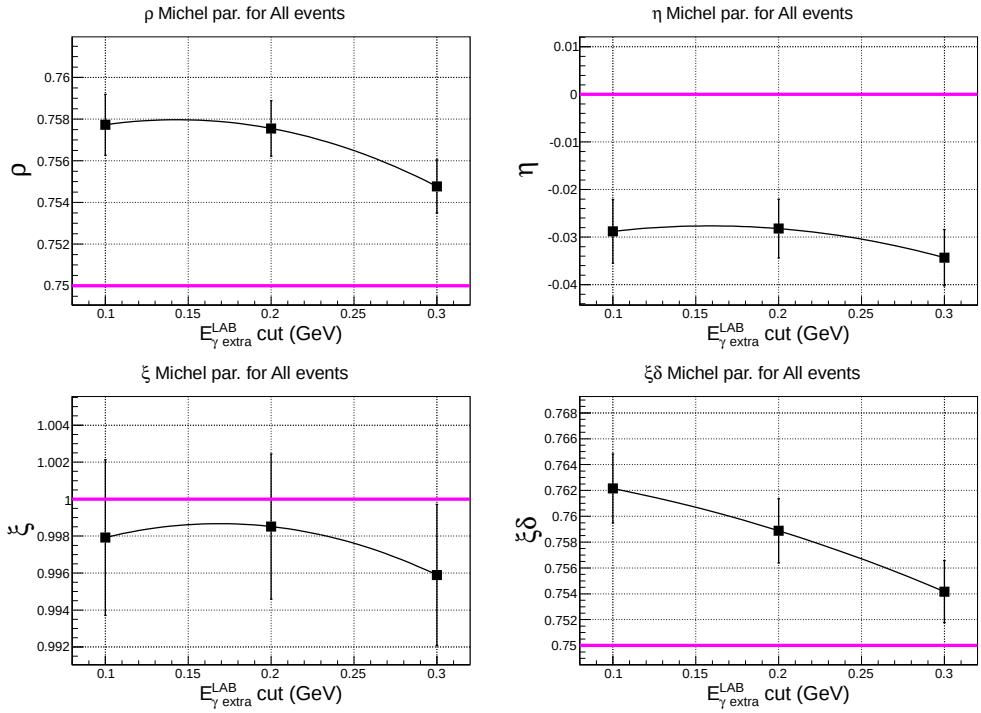

Figure 106: Optimal values of Michel parameters, ρ (upper left), η (upper right), ξ (lower left), $\xi\delta$ (lower right), from the **simultaneous fit** of the experimental ($e^{\pm}$; $\pi^{\mp}\pi^0$) and ($\mu^{\pm}$; $\pi^{\mp}\pi^0$) events (4D$\otimes$1D^5 scheme) as a function of the extra gamma energy ($E^{\rm LAB}_{\gamma\ {\rm extra}}$) cut. Magenta line shows the SM expectation for the corresponding Michel parameter.

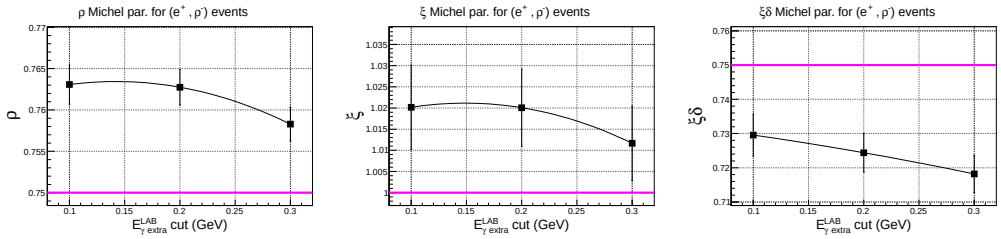

Figure 107: Optimal values of Michel parameters, ρ (left), ξ (middle), $\xi\delta$ (right), from the fit of the experimental (e^+; $\pi^-\pi^0$) events ($3D\otimes 2D^5/1D^4$ scheme) as a function of the extra gamma energy ($E^{\rm LAB}_{\gamma\ {\rm extra}}$) cut. Magenta line shows the SM expectation for the corresponding Michel parameter.

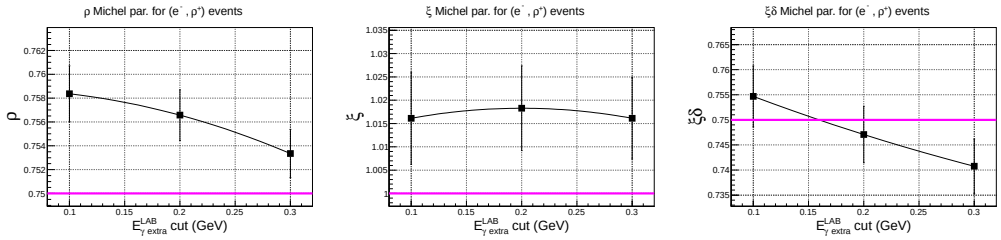

Figure 108: Optimal values of Michel parameters, ρ (left), ξ (middle), $\xi\delta$ (right), from the fit of the experimental (e^-; $\pi^+\pi^0$) events ($3D\otimes 2D^5/1D^4$ scheme) as a function of the extra gamma energy ($E^{\rm LAB}_{\gamma\ {\rm extra}}$) cut. Magenta line shows the SM expectation for the corresponding Michel parameter.

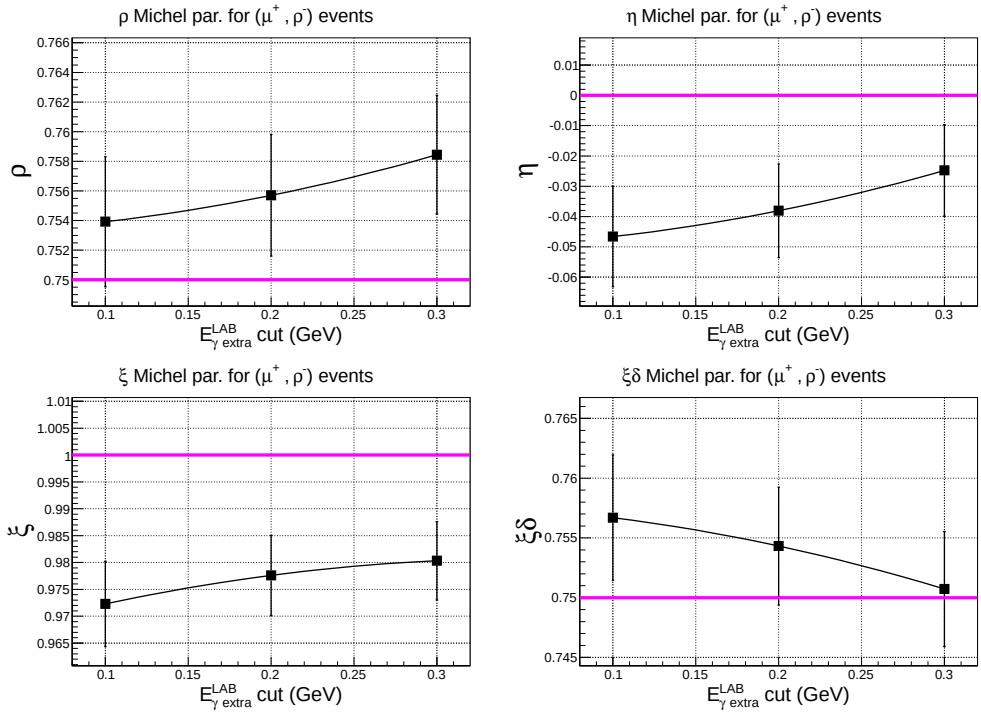

Figure 109: Optimal values of Michel parameters, ρ (upper left), η (upper right), ξ (lower left), $\xi\delta$ (lower right), from the fit of the experimental (μ^+; $\pi^-\pi^0$) events (3D$\otimes$2D^5/1D^4 scheme) as a function of the extra gamma energy ($E^{\rm LAB}_{\gamma\ {\rm extra}}$) cut. Magenta line shows the SM expectation for the corresponding Michel parameter.

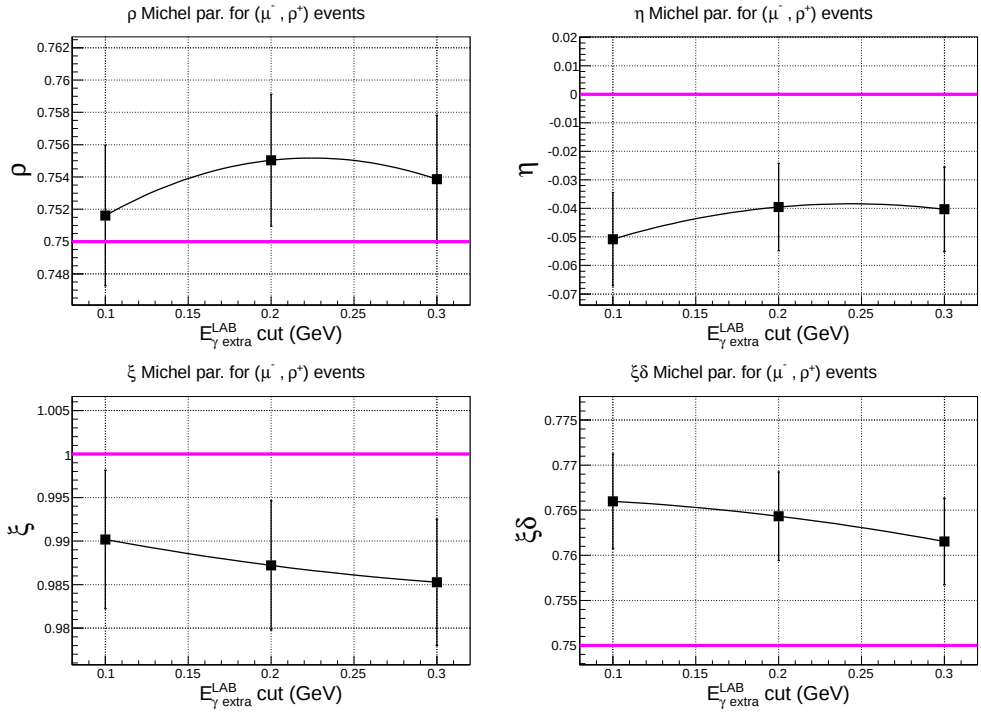

Figure 110: Optimal values of Michel parameters, ρ (upper left), η (upper right), ξ (lower left), $\xi\delta$ (lower right), from the fit of the experimental (μ^-; $\pi^+\pi^0$) events (3D$\otimes$2D^5/1D^4 scheme) as a function of the extra gamma energy ($E^{\rm LAB}_{\gamma\ {\rm extra}}$) cut. Magenta line shows the SM expectation for the corresponding Michel parameter.

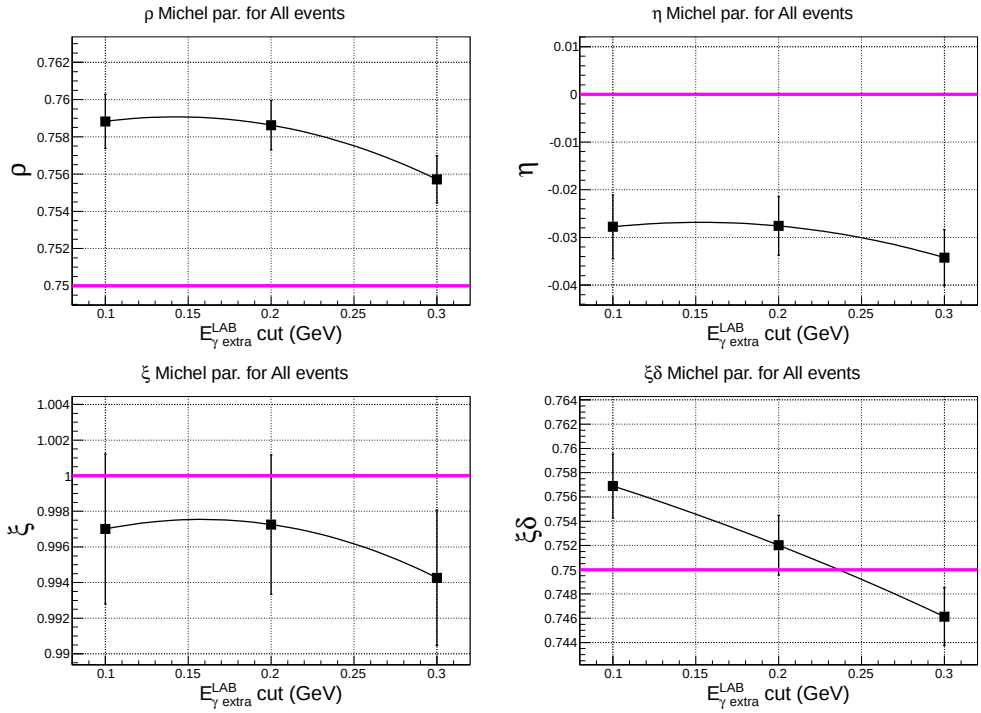

Figure 111: Optimal values of Michel parameters, ρ (upper left), η (upper right), ξ (lower left), $\xi\delta$ (lower right), from the **simultaneous fit** of the experimental ($e^{\pm}$; $\pi^{\mp}\pi^0$) and ($\mu^{\pm}$; $\pi^{\mp}\pi^0$) events (3D$\otimes$2D^5/1D^4 scheme) as a function of the extra gamma energy ($E^{\rm LAB}_{\gamma\ {\rm extra}}$) cut. Magenta line shows the SM expectation for the corresponding Michel parameter.

8 Study of the systematic uncertainties, results

It is confirmed that the uncertainties arising from the physical and apparatus corrections to the PDF are well below 1%; see Table 15. The statistical uncertainties of the normalization coefficients are kept as small as possible. The contribution to the systematic uncertainties of the Michel parameters due to the finite accuracy of the normalization coefficients shown in Table 15 are evaluated with the entire available generic $\tau^+\tau^-$ MC sample; they provide notable contributions. We observe a correlation of about 92% between the ρ and η parameters. The slope of the corresponding error ellipse exhibits an approximate dependence of $\Delta\eta \approx 4\Delta\rho$, which is incorporated as an inflated uncertainty of the η parameter in Table 15. However, we still

Table 15: Systematic uncertainties of Michel parameters related to physical and apparatus corrections, and accuracy of the normalization coefficients $C_i (i = 0 \div 4)$. Values are shown in units of percent (i.e. absolute deviation of the Michel parameter is multiplied by 100%).

Source	$\sigma(\rho), \%$	$\sigma(\eta), \%$	$\sigma(\xi_\rho\xi), \%$	$\sigma(\xi_\rho\xi\delta), \%$
Physical corrections				
ISR+$\mathcal{O}(\alpha^3)$	0.10	0.30	0.20	0.15
$\tau \to \ell\nu\nu\gamma$	0.03	0.10	0.09	0.08
$\tau \to \rho\nu\gamma$	0.06	0.16	0.11	0.02
Apparatus corrections				
Resolution $\oplus$ brems.	0.10	0.33	0.11	0.19
$\sigma(E_{\rm beam})$	0.07	0.25	0.03	0.15
Normalisation				
ΔC_1	0.21	0.60	0.14	0.12
ΔC_3	< 0.01	< 0.01	0.35	0.03
ΔC_4	0.02	0.03	0.05	0.23
Total	0.27	0.81	0.47	0.40

observe a systematic bias of the order of a few percent, especially in the $\xi_\rho\xi$ and $\xi_\rho\xi\delta$ Michel parameters. The current/tentative systematic uncertainty was obtained as a maximal difference of Michel parameter over 4 configurations and over 3 extra gamma energy cuts (very conservative estimation), see

Tables 12,14 and Figures 107-111:

$$\rho = 0.7586 \pm 0.0013_{\rm stat} \pm 0.0115_{\rm syst},$$

$$\eta = -0.0276 \pm 0.0062_{\rm stat} \pm 0.0219_{\rm syst},$$

$$\xi_\rho\xi = 0.9973 \pm 0.0039_{\rm stat} \pm 0.0479_{\rm syst},$$

$$\xi_\rho\xi\delta = 0.7520 \pm 0.0025_{\rm stat} \pm 0.0478_{\rm syst}.$$

Within errors all Michel parameters agree with the Standard Model expectation.

It is seen that our tentative systematic uncertainties are several times larger than those, mentioned in Table 15. Additional systematic uncertainty comes from the still imperfect description of the remaining background, for the $\xi_\rho\xi$ and $\xi_\rho\xi\delta$ parameters this uncertainty reaches 1%, see Fig. 74 (Sect. 5). To cure the remaining bias it would be helpful to check the contents of the remaining background and establish all modes with the admixtures larger or equal to 0.1%. It might happen that some of these backgrounds should be described analytically in the total PDF.

We also observe large difference between optimal $\xi_\rho\xi$ values (about 4%) for the $(e^+;\ \rho^-)$ (Fig. 107) and $(\mu^+;\ \rho^-)$ (Fig. 109) events, as well as between optimal $\xi_\rho\xi\delta$ values (about 4%) for the $(e^+;\ \rho^-)$ and $(\mu^-;\ \rho^+)$ (Fig. 105) events. These uncertainties are associated mainly to the trigger efficiency corrections, which should be tabulated as a functions of all important kinematical variables (not only lepton energy).

9 Summary

We present a study of Michel parameters in leptonic τ decays using a 485 fb^{-1} data sample collected at Belle. Michel parameters are extracted in the unbinned maximum likelihood fit of the $\ell-\rho$ events in the full nine-dimensional phase space. We exploit the spin-spin correlation of tau leptons to extract $\xi_\rho\xi$ and $\xi_\rho\xi\delta$ in addition to the ρ and η Michel parameters:

$$\rho = 0.7586 \pm 0.0013_{\text{stat}} \pm 0.0115_{\text{syst}},$$

$$\eta = -0.0276 \pm 0.0062_{\text{stat}} \pm 0.0219_{\text{syst}},$$

$$\xi_\rho\xi = 0.9973 \pm 0.0039_{\text{stat}} \pm 0.0479_{\text{syst}},$$

$$\xi_\rho\xi\delta = 0.7520 \pm 0.0025_{\text{stat}} \pm 0.0478_{\text{syst}}.$$

Although systematic uncertainties coming from the physical and apparatus corrections as well as from the normalisation are below 1%, currently we still have a relatively large systematic bias in the $\xi_\rho\xi$ and $\xi_\rho\xi\delta$ parameters, which originates from the inaccurate description of the remaining background as well as from the too rough tabulation of the trigger efficiency corrections.

References

[1] A. Rouge, Eur. Phys. J. C **18** (2001) 491.

[2] J. Polak and M. Zralek, Nucl. Phys. B **363** (1991) 385.

[3] J. Polak and M. Zralek, Phys. Rev. D **46** (1992) 3871.

[4] J. Polak and M. Zralek, Phys. Lett. B **276** (1992) 492.

[5] M. A. B. Beg, R. V. Budny, R. N. Mohapatra and A. Sirlin, Phys. Rev. Lett. **38** (1977) 1252 [Erratum-ibid. **39** (1977) 54].

[6] H. E. Haber, G. L. Kane and T. Sterling, Nucl. Phys. B **161** (1979) 493.

[7] J. F. Gunion and H. E. Haber, Nucl. Phys. B **272** (1986) 1 [Erratum-ibid. B **402** (1993) 567].

[8] J. F. Gunion and H. E. Haber, Nucl. Phys. B **278**, 449 (1986).

[9] J. P. Alexander *et al.* [CLEO Collaboration], Phys. Rev. D **56** (1997) 5320 [hep-ex/9705009].

[10] A. Heister *et al.* [ALEPH Collaboration], Eur. Phys. J. C **22** (2001) 217.

[11] Y. -S. Tsai, Phys. Rev. D **4** (1971) 2821 [Erratum-ibid. D **13** (1976) 771].

[12] M. Fujikawa *et al.* [Belle Collaboration], Phys. Rev. D **78** (2008) 072006.

[13] Z. Wąs, Nucl. Phys. Proc. Suppl. **98** (2001) 96.

[14] http://belle.kek.jp/secured/wiki/doku.php?id=physics:taup:tauola

[15] D. M. Schmidt, R. J. Morrison and M. S. Witherell, Nucl. Instrum. Meth. A **328** (1993) 547.

[16] H. Albrecht *et al.* [ARGUS Collaboration], Phys. Lett. B **250** (1990) 164.

[17] M. Davier *et. al* Phys. Lett. B **306** (1993) 411.

[18] W. Fetscher, Phys. Rev. D **42** (1990) 1544.

[19] K. Tamai, Nucl. Phys. B **668** (2003) 385.

[20] K. Tamai, KEK Preprint 2003-14.

[21] K. Tamai, Belle note 471.

[22] M. Schmidtler IEKP-KA/93-14 1993.

[23] A. B. Arbuzov, G. V. Fedotovich, E. A. Kuraev, N. P. Merenkov, V. D. Rushai and L. Trentadue, JHEP **9710** (1997) 001 [hep-ph/9702262].

[24] A. B. Arbuzov, G. V. Fedotovich, F. V. Ignatov, E. A. Kuraev, A. L. Sibidanov, "Monte-carlo generator for the processes $e^+e^- \to e^+e^-$, $\mu^+\mu^-$, $\pi^+\pi^-$ and K^+K^-, K_LK_S with precise radiative corrections at low energies," BINP Preprint 2004-70.
http://www.inp.nsk.su/activity/preprints/files/2004_070.pdf

[25] A. B. Arbuzov, G. V. Fedotovich, F. V. Ignatov, E. A. Kuraev and A. L. Sibidanov, Eur. Phys. J. C **46** (2006) 689 [hep-ph/0504233].

[26] E. A. Kuraev and V. S. Fadin, Sov. J. Nucl. Phys. **41** (1985) 466 [Yad. Fiz. **41** (1985) 733].

[27] F. A. Berends, R. Kleiss, S. Jadach and Z. Was, Acta Phys. Polon. B **14** (1983) 413.

[28] S. Jadach and Z. Was, Acta Phys. Polon. B **15** (1984) 1151 [Erratum-ibid. B **16** (1985) 483].

[29] S. Jadach and Z. Was, Comput. Phys. Commun. **36** (1985) 191.

[30] S. Actis *et al.* [Working Group on Radiative Corrections and Monte Carlo Generators for Low Energies Collaboration], Eur. Phys. J. C **66** (2010) 585 [arXiv:0912.0749 [hep-ph]].

[31] http://cmd.inp.nsk.su/~ignatov/vpl/

[32] S. Jadach, B. F. L. Ward and Z. Was, Comput. Phys. Commun. **130** (2000) 260.

[33] B. F. L. Ward, S. Jadach and Z. Was, Nucl. Phys. Proc. Suppl. **116** (2003) 73.

[34] A. B. Arbuzov, Phys. Lett. B **524** (2002) 99.

[35] A. Arbuzov, A. Czarnecki and A. Gaponenko, Phys. Rev. D **65** (2002) 113006.

[36] A. Arbuzov and K. Melnikov, Phys. Rev. D **66** (2002) 093003.

[37] M. Jezabek, Comput. Phys. Commum. **70** (1992) 69.

[38] A. Czarnecki, M. Jezabek and J. H. Kuhn, Nucl. Phys. B **351** (1991) 70.

[39] F. Flores-Baez *et al*, Phys. Rev. Lett. D **74** (2006) 071301(R).

[40] A. Flores-Tlalpa *et al*, Nucl. Phys. B (Proc. Suppl.) **169** (2007) 250.

[41] E. Barberio and Z. Was, Comput. Phys. Commun. **79** (1994) 291.

[42] Z. Was, P. Golonka and G. Nanava, PoS ACAT (2007) 071.

[43] Z. Was, P. Golonka and G. Nanava, Nucl. Phys. Proc. Suppl. **181-182** (2008) 269.

[44] Y. Ohnishi, Belle Note 148, (1996).

[45] K. Inami, Belle Note 629, (2003).

[46] K. Inami, tautp_ml:1916, September 28, (2006).

[47] D. M. Asner *et al.* [CLEO] Phys. Rev. D **61** (1999) 012002.

[48] S. Jadach, J. H. Kuhn and A. Was, Comp. Phys. Comm. **64** (1991) 275.

[49] L. Hinz *et al.* Belle Note 777 (2004), Belle Note 954 (2006).

[50] http://belle.kek.jp/group/pid_joint/

A GDL input and output bit definition

bit	delay	mnemonic	description
0	0	ncdr_full0	first bit of the number of CDC R-ϕ full tracks full track $\equiv$ track segments in all 6 trigger superlayers
1	0	ncdr_full1	second bit of the number of CDC R-ϕ full tracks
2	0	ncdr_short0	first bit of the number of CDC R-ϕ short tracks short track $\equiv$ track segments in 3 inner trigger superlayers short track includes full track
3	0	ncdr_short1	second bit of the number of CDC R-ϕ short tracks
4	0	ncdr_short2	third bit of the number of CDC R-ϕ short tracks
5	0	cdc_bb	1-7 back to back tracks with 64 segmentation in CDC R-ϕ plane
6	0	cdc_open	opening angle cut ($> 135^\circ$)
7	0	cdc_spare	not used
8	8	ncdz0	first bit of the number of CDC Z tracks
9	8	ncdz1	second bit of the number of CDC Z tracks
10			
11	0	calib0	internal trigger from SEQ (random trigger source)
12	28	tsc_mult	TOF multiplicity (GE 2 counter hits)
13	28	tsc_pat	TOF hit pattern (1-3 back to back)
14	28	tsc_ge1	number of TSC hits ≥ 1
15	28	tsc_ge2	number of TSC hits ≥ 2
16	28	tsc_timing	TOF timing signal
17	0	csi_timing	ECL timing signal
18	2	e_high	ECL high energy trigger (> 1.0 GeV)
19	2	e_low	ECL low energy trigger (> 0.5 GeV)
20	2	e_lum	ECL energy trigger for luminosity monitoring (> 3.0 GeV)
21	0	csi_bb	ECL Bhabha veto trigger
22	0	csi_bbpre	OR of 11 types of prescaled Bhabha trigger (prescaled)
23	0	nicl0	first bit of the number of isolated clusters on ECL
24	0	nicl1	second bit of the number of isolated clusters on ECL
25	0	nicl2	third bit of the number of isolated clusters on ECL
26	0	nicl3	fourth bit of the number of isolated clusters on ECL
27	0	csi_cosmic	ECL cosmic veto trigger
28	0	csi_tpbbgg	Bhabha and $\gamma\gamma$ trigger based on $\theta - \phi$ segmentation
29	0	csi_tpbb	Bhabha trigger based on θ-ϕ segmentation
30	0	csi_tpgg	$\gamma\gamma$ trigger based on θ-ϕ segmentation
31	0	csi_tpgx	γX trigger based on θ-ϕ segmentation
32	14	efc_bb	EFC Bhabha trigger
33	17	efc_tag	EFC two photon tag trigger
34	0	efc_spare	
35			
36	17	csi_brlbb	ECL barrel bhabha trigger
37	0	csi_fabbb	ECL bhabha trigger (AND of forward and backward)
38	17	csi_fobbb	ECL bhabha trigger (OR of forward and backward)
39	0	svd_svd_l0	SVD L0 provided by a LeCroy NIM module
40	31	klm_fwd	KLM forward endcap trigger
41	31	klm_bwd	KLM backward endcap trigger
42	31	klm_brl	KLM barrel trigger

Figure 112: SVD-1 GDL input bits, part I.

bit	delay	mnemonic	description
43	0		
44	0	final	delayed final trigger as a random trigger source
45	0	monitor1	
46	0	revolution	Revolution signal (timing is adjusted to bunch no. 0 for SVD)
47	0	svd_l0m	L0 trigger for SVD (modified)
48	–	cdc_hv_cc	CDC current limiter
49	–	svd_l0_64	L0 trigger with 64 segmentaions
50	–	svd_l0	L0 trigger for SVD
51	–	tsc_iv_on	TOF single rate (TSC60) when injection veto is ON
52	–	tsc_iv_off	TOF single rate (TSC60) when injection veto is OFF
53	–	tsc_mod35	TOF single rate (TSC35)
54	–	tsc_mod62	TOF single rate (TSC62)
55	–	scaler7	

Figure 113: SVD-1 GDL input bits, part II.

bit	mnemonic	PSV	definition
0	ff_zt2oc	1	(ncdr_full>1)&cdc_open&tsc_ge2&(ncdz>0)&csi_timing&!csi_bb
1	ff_t2oc	20	(ncdr_full>1)&cdc_open&tsc_ge2&csi_timing&!csi_bb
2	fs_ztoc	–	(ncdr_short>1)&(ncdr_full>0)&cdc_open&tsc_ge1&(ncdz>0)&csi_timing&!csi_bb
3	fs_toc	500	(ncdr_short>1)&(ncdr_full>0)&cdc_open&tsc_ge1&csi_timing&!csi_bb
4	ffs_zt2	1	(ncdr_short>2)&(ncdr_full>1)&tsc_ge2&(ncdz>0)
5	ffs_zt2oc	1	(ncdr_short>2)&(ncdr_full>1)&tsc_ge2&(ncdz>0)&cdc_open&csi_timing
6	fff_ot2c2z	1	(ncdr_full>2)&cdc_open&tsc_ge2&(nicl>1)&(ncdz>0)
7	fff_ot2c2	–	(ncdr_full>2)&cdc_open&tsc_ge2&(nicl>1)
8	ffs_t2	20	(ncdr_short>2)&(ncdr_full>1)&tsc_ge2
9	ffs	–	(ncdr_short>2)&(ncdr_full>1)
10	fff_ot2z	1	(ncdr_full>2)&cdc_open&tsc_ge2&(ncdz>0)
11	fsss_toc	20	(ncdr_short>3)&(ncdr_full>0)&tsc_ge1&cdc_open&csi_timing
12	hie	1	e_high&!csi_bb&!csi_cosmic
13	clst4	1	(nicl>3)&!csi_cosmic
14	loe_clst3	20	e_low&(nicl>2)&!csi_cosmic
15	loe_trk2	20	e_low&(ncdr_short>1)&((ncdr_full>0)#(ncdz>0))&cdc_open&!csi_bb
16	two_photon	5	efc_tag&(ncdr_short>1)&(ncdr_full>0)
17	csi_bhabha_p	–	csi_bbpre
18	csi_bhabha	50	csi_bb
19	csi_lum_e	50	e_lum
20	efc_bhabha	150	efc_bb
21	tof_b2b	10000	tsc_pat
22	abe_bhabha	–	csi_bb&cdc_bb
23	dimu_noz	–	cdc_bb&(tsc_pat#(nicl>1))
24	klm_opn	1	cdc_open&(klm_brl#klm_fwd#klm_bwd)
25	klm_b2b	1	cdc_bb&(klm_brl#klm_fwd#klm_bwd)
26	random_bg	600	final
27	clst5	1	(nicl>4)&!csi_cosmic
28	short_gt_1	30000	(ncdr_short>1)
29	taumon	200	((((ncdr_full>1)&tsc_ge2&csi_timing)#(e_low&(ncdr_short>1)&(ncdr_full>0))#(nicl>1))
			&cdc_open&(ncdz>0))#e_high
30	hadronb	1	(ncdr_short>2)&(ncdr_full>0)&(ncdz>0)&e_low&(nicl>1)&tsc_ge1
31	ff_zt2c	10	(ncdr_full>1)&tsc_ge2&(ncdz>0)&csi_timing&!csi_bb
32	loe_fs_z	10	e_low&(ncdr_short>1)&(ncdr_full>0)&(ncdz>0)&!csi_bb
33	cdcbb	4000	cdc_bb
34	gphi	2	e_lum&(ncdr_short>1)&!cdc_open&!csi_fabbb
35	gammax	50	csi_fobbb&!csi_fabbb&(ncdr_short>1)
36	brl_bhabha	10	csi_brlbb
37	brl_2gamma	20	csi_brlbb&!cdc_open
38	revol	200000	revolution
39	clst2_o	30	(nicl>1)&cdc_open&!csi_bb
40	hadron	1	(ncdr_short>2)&e_low&(nicl>1)&tsc_ge1
41	efc	5	efc_tag&(nicl>1)
42	e_hi_clst4	20	(nicl>3)&e_high
43	hadronc	1	(ncdr_short>2)&(ncdr_full>1)&cdc_open&e_high&(nicl>2)&tsc_ge1
44	loe_fs_oz	1	e_low&(ncdr_short>1)&(ncdr_full>0)&cdc_open&(ncdz>0)&!csi_bb
45	dimu_z	40	cdc_bb&(tsc_pat#(nicl>1))&(ncdz>0)
46	clst2_oz	2	(nicl>1)&cdc_open&(ncdz>0)&!csi_bb
47	e_had	1	e_lum&!csi_bb

Figure 114: SVD-1 GDL output bits, part I.

bit	mnemonic	PSV	definition
48	s	–	(ncdr_short>0)
49	f	–	(ncdr_full>0)
50	fs_b	–	(ncdr_full>0)&(ncdr_short>1)&!csi_bb
51	ff_b	–	(ncdr_full>1)&!csi_bb
52	fff	–	(ncdr_full>2)
53	fs_o_b	–	(ncdr_full>0)&(ncdr_short>1)&cdc_open&!csi_bb
54	ff_o_b	–	(ncdr_full>1)&cdc_open&!csi_bb
55	ffs_o	–	(ncdr_full>1)&(ncdr_short>2)&cdc_open
56	fff_o	–	(ncdr_full>2)&cdc_open
57	tp_bbgg	–	csi_tpbbgg
58	tp_bb	–	csi_tpbb
59	tp_2gamma	–	csi_tpgg
60	tp_gammax	–	csi_tpgx
61	random	42	randin
62	ff_t2o	–	(ncdr_full>1)&tsc_ge2&cdc_open&!csi_bb
63	ffs_zt2o	—	(ncdr_full>1)&(ncdr_short>2)&cdc_open&(ncdz>0)&tsc_ge2

FTDL logic version 5.04. Modified bits are shown. This is used from run 295.

53	loe_fs_o	–	e_low&(ncdr_short>1)&(ncdr_full>0)&cdc_open&!csi_bb
55	loe_fs_oc1	–	e_low&(ncdr_short>1)&(ncdr_full>0)&cdc_open&!csi_bb&(nicl>0)
56	loe_fs_oc2	–	e_low&(ncdr_short>1)&(ncdr_full>0)&cdc_open&!csi_bb&(nicl>1)

Figure 115: SVD-1 GDL output bits, part II.

bit	delay	mnemonic	description
0	12	ncdr_full0	first bit of the number of CDC R-ϕ full tracks full track $\equiv$ track segments in all 6 trigger superlayers
1	12	ncdr_full1	second bit of the number of CDC R-ϕ full tracks
2	12	ncdr_short0	first bit of the number of CDC R-ϕ short tracks short track $\equiv$ track segments in 3 inner trigger superlayers short track includes full track
3	12	ncdr_short1	second bit of the number of CDC R-ϕ short tracks
4	12	ncdr_short2	third bit of the number of CDC R-ϕ short tracks
5	12	cdc_bb	1-7 back to back tracks with 64 segmentation in CDC R-ϕ plane
6	12	cdc_open	opening angle cut ($> 135°$)
7	0	final	delayed final trigger as a random source
8	28	efc_bb	EFC Bhabha trigger
9	34	efc_tag	EFC two photon tag trigger
10	0	revolution	Revolution signal (timing is adjusted to bunch no. 0 for SVD)
11	0	randin	internal trigger from SEQ (random trigger source)
12	56	tsc_mult	TOF multiplicity (GE 2 counter hits)
13	56	tsc_pat	TOF hit pattern (1-3 back to back)
14	56	tsc_ge1	number of TSC hits ≥ 1
15	56	tsc_ge2	number of TSC hits ≥ 2
16	56	tsc_timing	TOF timing signal
17	0	csi_timing	ECL timing signal
18	4	e_high	ECL high energy trigger (> 1.0 GeV)
19	4	e_low	ECL low energy trigger (> 0.5 GeV)
20	4	e_lum	ECL energy trigger for luminosity monitoring (> 3.0 GeV)
21	0	csi_bb	ECL Bhabha veto trigger
22	32	csi_brlbb	ECL barrel bhabha trigger
23	0	nicl0	first bit of the number of isolated clusters on ECL
24	0	nicl1	second bit of the number of isolated clusters on ECL
25	0	nicl2	third bit of the number of isolated clusters on ECL
26	0	nicl3	fourth bit of the number of isolated clusters on ECL
27	0	csi_cosmic	ECL cosmic veto trigger
28	0	csi_tpbbgg	Bhabha and $\gamma\gamma$ trigger
29	0	csi_tpbb	Bhabha trigger based on θ-ϕ segmentation
30	0	csi_tpgg	$\gamma\gamma$ trigger based on θ-ϕ segmentation
31	0	csi_tpgx	γX trigger based on θ-ϕ segmentation
32	12	nsvdz_short0	first bit of the number of SVD Z short tracks
33	12	nsvdz_short1	second bit of the number of SVD Z short tracks
34	12	nsvdz_short2	third bit of the number of SVD Z short tracks
35	12	nsvdr_short0	first bit of the number of SVD R-ϕ short tracks
36	12	nsvdr_short1	second bit of the number of SVD R-ϕ short tracks
37	12	lum	Lum.
38	12	svdz_bb	1-7 back to back tracks with 64 segmentation in SVD R-ϕ plane
39	12	svdz_open	opening angle cut ($> 135°$)

Figure 116: SVD-2 GDL input bits, part I.

bit	delay	mnemonic	description
40	62	klm_fwd	KLM forward endcap trigger
41	62	klm_bwd	KLM backward endcap trigger
42	62	klm_brl	KLM barrel trigger
43	6	svd_tofcdc	for SVD L0 study
44	12	nsvdz_full0	first bit of the number of SVD Z full tracks
45	12	nsvdz_full1	second bit of the number of SVD Z full tracks
46	12	nsvdr_full0	first bit of the number of SVD R-ϕ full tracks
47	12	nsvdr_full1	second bit of the number of SVD R-ϕ full tracks
48	0	cdc_hv_cc	CDC current limiter
49	0	tsc_l0_64	L0 trigger with 64 segmentaions
50	0	tsc_l0_32	L0 trigger with 32 segmentaions
51	0	tsc_iv_on	TOF single rate (TSC60) when injection veto is ON
52	0	tsc_iv_off	TOF single rate (TSC60) when injection veto is OFF
53	0	tsc_mod35	TOF single rate (TSC35)
54	0	tsc_mod62	TOF single rate (TSC62)
55	0	tsc_l0_32m	TOF rate (L0-Mode32)
56	0	svd_l0	L0 trigger for SVD (modified)
57	0	svd_hold	L0 trigger hold for SVD
58	0	scaler10	scaler10
59	0	scaler11	scaler11
60	0	scaler12	scaler12
61	0	scaler13	scaler13
62	0	scaler14	scaler14
63	0	scaler15	scaler15

Figure 117: SVD-2 GDL input bits, part II.

bit	mnemonic	PSV	definition
0	fs_toc	1000	(ncdr_short>1)&(ncdr_full>0)&cdc_open&tsc_ge1&csi_timing&!csi_bb&(!iveto35)
1	fs_toc2	500	(ncdr_short>1)&(ncdr_full>0)&cdc_open&tsc_ge2&(nicl>1)&!csi_bb&(!iveto35)
2	ff_toc	20	(ncdr_full>1)&cdc_open&tsc_ge1&csi_timing&!csi_bb&(!iveto35)
3	ff_t2oc	1	(ncdr_full>1)&cdc_open&tsc_ge2&csi_timing&!csi_bb&(!iveto35)
4	ff_t2oc2	1	(ncdr_full>1)&cdc_open&tsc_ge2&(nicl>1)&!csi_bb&(!iveto35)
5	ffs_t2	20	(ncdr_short>2)&(ncdr_full>1)&tsc_ge2&(!iveto35)
6	ffs_t2o	20	(ncdr_short>2)&(ncdr_full>1)&tsc_ge2&cdc_open&(!iveto35)
7	ffs_t2oc	1	(ncdr_short>2)&(ncdr_full>1)&tsc_ge2&cdc_open&csi_timing&(!iveto35)
8	ffs_t2oc2	1	(ncdr_short>2)&(ncdr_full>1)&tsc_ge2&cdc_open&(nicl>1)&(!iveto35)
9	fff_t2o	20	(ncdr_full>2)&cdc_open&tsc_ge2&(!iveto35)
10	fff_t2oc2	1	(ncdr_full>2)&cdc_open&tsc_ge2&(nicl>1)&(!iveto35)
11	fsss_toc	20	(ncdr_short>3)&(ncdr_full>0)&tsc_ge1&cdc_open&csi_timing&(!iveto35)
12	fs_to	–	(ncdr_short>1)&(ncdr_full>0)&cdc_open&tsc_ge1&!csi_bb&(!iveto35)
13	fs_t2o	–	(ncdr_short>1)&(ncdr_full>0)&cdc_open&tsc_ge2&!csi_bb&(!iveto35)
14	ff_to	–	(ncdr_full>1)&cdc_open&tsc_ge1&!csi_bb&(!iveto35)
15	ff_t2o	–	(ncdr_full>1)&cdc_open&tsc_ge2&!csi_bb&(!iveto35)
16	hie	1	e_high&!csi_bb&!csi_cosmic&(!iveto35)
17	clst4	1	(nicl>3)&!csi_cosmic&(!iveto35)
18	clst5	1	(nicl>4)&!csi_cosmic&(!iveto35)
19	loe_clst3	20	e_low&(nicl>2)&!csi_cosmic&(!iveto35)
20	e_hi_clst4	20	(nicl>3)&e_high&(!iveto35)
21	e_had	1	e_lum&!csi_bb&(!iveto35)
22	dummy22	–	GN
23	dummy23	–	GN
24	hadron_a	1	(ncdr_short>2)&e_low&(nicl>1)&tsc_ge1&(!iveto35)
25	hadron_b	1	(ncdr_short>2)&(ncdr_full>0)&e_low&(nicl>1)&tsc_ge1&(!iveto35)
26	hadron_c	1	(ncdr_short>2)&(ncdr_full>1)&cdc_open&e_high&(nicl>2)&tsc_ge1&(!iveto35)
27	loe_fs_o	1	e_low&(ncdr_short>1)&(ncdr_full>0)&cdc_open&!csi_bb&(!iveto35)
28	loe_fs_to	1	e_low&(ncdr_short>1)&(ncdr_full>0)&tsc_ge1&cdc_open&!csi_bb&(!iveto35)
29	clst2_o	30	(nicl>1)&cdc_open&!csi_bb&(!iveto35)
30	clst2_to	30	(nicl>1)&tsc_ge1&cdc_open&!csi_bb&(!iveto35)
31	two_photon	–	efc_tag&(ncdr_short>1)&(ncdr_full>0)&(!iveto35)
32	tau	200	((((ncdr_full>1)&tsc_ge2&csi_timing
33	dummy33	–	GN
34	dummy34	–	GN
35	dummy35	–	GN
36	dummy36	–	GN
37	dummy37	–	GN
38	dummy38	–	GN
39	dummy39	–	GN
40	csi_bhabha	50	csi_bb&(!iveto35)
41	csi_lum_e	50	e_lum&(!iveto35)
42	brl_bhabha	10	csi_brlbb&(!iveto35)
43	tp_bb	–	csi_tpbb&(!iveto35)
44	efc_bhabha	–	efc_bb&(!iveto35)
45	abe_bhabha	–	csi_bb&cdc_bb&(!iveto35)
46	random_lum	400	lum&(!iveto35)
47	random_lumv	–	lum&iveto35

Figure 118: SVD-2 GDL output bits, part I.

bit	mnemonic	PSV	definition
48	tp_bbgg	–	csi_tpbbgg&(!iveto35)
49	tp_2gamma	–	csi_tpgg&(!iveto35)
50	tp_gammax	–	csi_tpgx&(!iveto35)
51	brl_2gamma	20	csi_brlbb&!cdc_open&(!iveto35)
52	klm_tsc	10	tsc_pat&(klm_br
53	tof_b2b	10000	tsc_pat&(!iveto35)
54	cdcbb	4000	cdc_bb&(!iveto35)
55	dimu	20	cdc_bb&tsc_pat&(nicl>1)&(!iveto35)
56	dimu_tsc	20	cdc_bb&tsc_pat&(!iveto35)
57	klm_opn	1	cdc_open&(klm_br
58	klm_b2b	1	cdc_bb&(klm_br
59	random_bg	600	final&(!iveto35)
60	revol	200000	revolution&(!iveto35)
61	random	–	randin&(!iveto35)
62	efc	–	efc_tag&(nicl>1)&(!iveto35)
63	dimu_c2	–	cdc_bb&(nicl>1)&(!iveto35)
64	s	–	(ncdr_short>0)&(!iveto35)
65	f	–	(ncdr_full>0)&(!iveto35)
66	ss	–	(ncdr_short>1)&!csi_bb&(!iveto35)
67	fs	–	(ncdr_full>0)&(ncdr_short>1)&!csi_bb&(!iveto35)
68	ff	–	(ncdr_full>1)&!csi_bb&(!iveto35)
69	ffs	–	(ncdr_short>2)&(ncdr_full>1)&(!iveto35)
70	fff	–	(ncdr_full>2)&(!iveto35)
71	fs_o	–	(ncdr_full>0)&(ncdr_short>1)&cdc_open&!csi_bb&(!iveto35)
72	ff_o	–	(ncdr_full>1)&cdc_open&!csi_bb&(!iveto35)
73	ffs_o	–	(ncdr_full>1)&(ncdr_short>2)&cdc_open&(!iveto35)
74	fff_o	–	(ncdr_full>2)&cdc_open&(!iveto35)
75	s2	–	(ncdr_short>1)&(!iveto35)

Figure 119: SVD-2 GDL output bits, part II.